Title

Hierarchical Assemblies in Supramolecular Nanocomposite Thin Films: Kinetic Pathway Dependence

Author

Evans, Katherine Marie

Publication Date

2019

Peer reviewed|Thesis/dissertation

Hierarchical Assemblies in Supramolecular Nanocomposite Thin Films: Kinetic Pathway Dependence

By

Katherine Marie Evans

A dissertation submitted in partial satisfaction of the

requirements for the degree of

Doctor of Philosophy

in

Chemistry

in the

Graduate Division

of the

University of California, Berkeley

Committee in charge:

Professor Ting Xu, Chair
Professor Peidong Yang
Professor Jie Yao

Fall 2019

Abstract

Hierarchical Assemblies in Supramolecular Nanocomposite Thin Films: Kinetic Pathway Dependence

By

Katherine Marie Evans

Doctor of Philosophy in Chemistry

University of California, Berkeley

Professor Ting Xu, Chair

Polymer nanocomposites are an extremely versatile class of materials due to the variety of materials that can be used and their many applications. Structured nanocomposites are of particular interest due to the potential of a structure/function relationship. In order to establish such a relationship, a variety of nanoscale structures with control over how to generate them. Block copolymer (BCP)-based supramolecules have been studied for the past two decades in thin film due to their ability to self-assemble to form order on the nanoscale. The complexity of supramolecules is obvious: they are constructed from noncovalently attaching a small molecule to a BCP block. As a multicomponent system, the self-assembly process is governed by competing thermodynamic and kinetic considerations. The thermodynamics that lead to equilibrium structures are well understood. In order to move beyond known structures and create tunable thin films, the kinetic pathway must studied.

The effect of several parameters in the multicomponent system on the final film structure and long-range order was quantified to understand the synergistic effects of the components. A multi-dimension diagram of the assembly process was developed that accounts for experimental observations in supramolecular thin films in the last decades from multiple groups. This diagram was used to create a design framework that can be used to control the long-range order in nanocomposite thin films by controlling the kinetic pathway.

The framework determined was applied to lithographically patterned substrates to achieve assemblies under incommensurate conditions that aligned with circular patterns. The resultant structures arise from the kinetic pathway during assembly rather than purely thermodynamic considerations.

A different kinetic regime was explored by using high molecular weight-based supramolecules. These films have two distinct kinetic regimes: slow diffusion

of highly entangled polymers and the relatively faster diffusion of nanoparticles. The two regimes can be modulated so that films with different structure and feature sizes can be achieved. *In situ* grazing-incidence transmission small angle X-ray scattering studies were performed to monitor the kinetic pathway taken during self-assembly to quantify the changes to structure and order in a solution-based process. The information about the importance of the kinetic pathway on a multicomponent system yielded a deeper understanding of the assembly process that opens the door to creating designer nanocomposites with precisely tailorable features.

Hierarchical Assemblies in Supramolecular Nanocomposite Thin Films: Kinetic Pathway Dependence

Table of Contents

Chapter 1

Structured Polymer Nanocomposites

1.1 Introduction

Polymer nanocomposites are ubiquitous in our society due to their rich diversity in both biological and synthetic systems. From fabrics to medical devices to solar cells and more, nanocomposites have been adopted in countless ways into our every day life. The ability to create these functional materials has been possible due to our understanding of how to control the chemistry, structure, processing, and functionality of the monomer building blocks, polymer chains overall, and additives. As science and technology progress, there is a pressing need to create new polymer-based films with increasingly specialized functionality and for use in a wide variety of fields.

Polymer nanocomposites can use a variety of building blocks including graphene, carbon nanotubes, metallic nanoparticles, and more[1-7]. While all these materials have interesting properties that they can impart to the nanocomposite, nanoparticles (NPs) are often used due to their diversity of structure and function. Nanoparticles (NPs), often referred to as artificial atoms, have unique optical, electrical, mechanical, and magnetic properties due to the quantum confinement effect[8-11]. Much effort has gone toward understanding the synthesis of particles of different shapes (rods, plates, dots, tetrapods, etc), sizes, and chemistry to fully harness the potential of these interesting materials[12-14]. By compatibilizing NPs so that they can be incorporated, dispersed, and arranged in a polymer matrix, their unique properties can be harnessed[3, 15-18]. This is not a trivial task.

Polymer architecture can be used to achieve structural control. Of particular interest are block copolymers (BCP), which are formed from two or more chemically

distinct segments. Such structures will self-assemble to form specified nanostructure, although these are often limited to a few equilibrium structures. BCP-based supramolecules, where a small molecule is non-covalently bonded to one of the blocks of the BCP, offer an improvement over traditional BCP systems[19, 20]. The small molecule can be used to easily introduce functionality without complex synthesis, including liquid crystals and organic semiconductors[21-25]. Liquid crystal-based supramolecules have been shown to introduce photophysical properties and make supramolecules responsive to external fields[25-30]. Organic semiconductors can be used to implement optical and electronic properties into simple polymer systems[31-33]. The small molecule can also be used to create stimuli-responsive systems, such as thermal switchable photonics or thermally switchable electrical conductivity[34-38]. The small molecule will also guide NP assembly if the ligand on the NP is chemically similar to the small molecule itself. Supramolecule systems additionally can be used to create self-assembled hierarchical structure with ordering on several length scales[35]. The small molecule is key for providing structure and functionality, but there is still much unknown about the pathway of assembly and how to guide it to create novel structures and exactly specifiable feature sizes and properties.

Supramolecular nanocomposites have a minimum of 4 components: two or more blocks of the BCP, the small molecule, and the NP. For thin films, solvent is often an additional component. The multicomponent system offers many challenges because the final film structure and functionality is a result of the balance of the thermodynamic and kinetic forces of each component operating at once. However,

these challenges each represent a handle that can be used to control and govern the final film assembly. In depth knowledge of the thermodynamic guiding forces have been studied for several decades now, but there are still many questions about the kinetic pathway as well as the interplay among components. In order to create tunable nanocomposites with arbitrary feature sizes, structure, and morphology, we must be able to go beyond existing knowledge of the self-assembly of supramolecular nanocomposites to understand the kinetic pathway during assembly. This thesis begins to answer questions of what is possible when the influence of each component of the multicomponent system on the final film features can identified, new pathways can be accessed during the assembly process that go beyond traditional thermodynamic limits, and the components are no longer limited by size restrictions. Understanding and balancing kinetic pathway of all components during self-assembly leads to greater structural control over polymer nanocomposites and opens the door for the creation of designer nanocomposites.

The following sections review the current knowledge guiding our understanding of the energy landscape of self-assembly of polymer nanocomposites. While supramolecules are of particular interest, the extensive knowledge gained from studies into BCPs alone is a good starting place for building an understanding of a more complex, multicomponent nanocomposite system. The known thermodynamic and kinetic considerations of supramolecular thin film systems, both with and without NPs, will be discussed in detail. Solvent annealing will be presented as key method for the processing of these nanocomposites. Self-assembly in systems under geometric confinement and in high molecular weight systems will

be discussed due to their differing considerations and new regimes as compared with traditional BCP self-assembly. While these processes and conditions are only a small slice of the rich variable space available for polymer-based nanocomposite self-assembly, they should begin to create a compelling overview of why knowledge about the kinetic pathway of assembly is critical for controlling the features of these systems.

1.2 Supramolecules- A multicomponent system

Supramolecules are formed from a BCP backbone with a small molecule non-covalently bonded to one of the blocks[35, 39]. The incorporation of this small molecule leads to greater structural control as well as a way to easily incorporate functionality without the need for complex synthetic steps over traditional BCP systems[20]. The small molecule will add new thermodynamic considerations of the self-assembly process. As is the case with traditional diblock copolymers, the thermodynamics of self-assembly are guided by the Gibb's Free Energy. Enthalpically, the interaction between the blocks is guided by the Flory-Huggins interaction parameter, χ_{AB}[40]. In thin films, the interaction energies between the substrate and BCP, as well as the air interface and BCP must also be considered[41]. New enthalpic interactions are added in supramolecules: the small molecule interactions with each BCP block, the enthalpy of the non-covalent bond that forms the supramolecule, and any interactions that the small molecule has for itself. For example, some small molecules with alkyl chains can have a driving force to crystallize[24]. The polymer conformation, geometric arrangement of the BCP

microdomains, and the small molecule translational entropy due to the number of configurations it can assume make up the entropic considerations. The balance between these enthalpic and entropic considerations results in an equilibrium structure, guided by a phase diagram, for both traditional BCPs (Figure 1a) and supramolecules (Figure 1b).

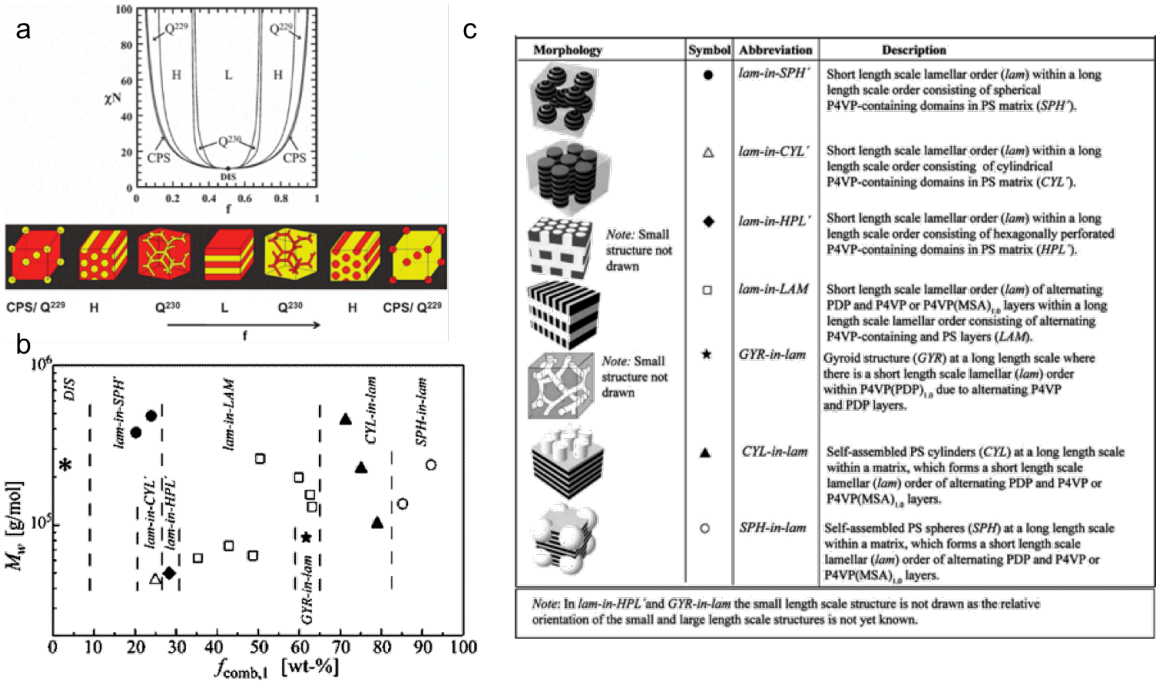

Figure 1: Phase diagram of (a) a block copolymer as a function of the volume fraction of each block with illustrations of each morphology shown and (b) a supramolecule as a function of the volume fraction of the comb block. The descriptions and illustrations of the expanded morphologies is shown in (c). BCP phase diagram (a) is reprinted with permission from Wiesner *et al*. Chem. Soc. Rev., **2011**, 40, 522. Copyright 2011 Royal Society of Chemistry. Supramolecule phase diagram and illustrations of morphology (b,c) are adapted with permission from Valkama *et al*. Macromoleucles, **2006**, 39, 9327. Copyright 2006 American Chemical Society.

One key effect of the small molecule in bulk supramolecules is to expand the phase diagram. The small molecule can stabilize semi-equilibrium states such as

hexagonally perforated lamellae, generate gyroid structures over a wider range, and generate non-equilibrium structures[42-45]. Crucially, the small molecule also introduces hierarchical structures, such as lamellae-in-lamellae and lamellae-in-spheres, due to the shorter length scale packing of the small molecule within the larger length scale microdomain of the BCP[39, 44, 46] (Figure 1c).

The small molecule loading can be used to select the final film morphology[44]. As discussed earlier, the morphology is a result of the relative volume of each block. In traditional BCP systems, the composition of the polymer must be changed to change the morphology. In supramolecules, however, the morphology can be selected by simply adding more or less small molecule to the system while keeping the BCP the same. Additionally, the solubility of the small molecule at different temperatures can be taken advantage of to induce order-order transitions[39].

In thin film, supramolecules have additional thermodynamic considerations. The enthalpy between the substrate/supramolecule and air interface/supramolecule will also affect the assembly process. This interface can be tuned to change the orientation of cylindrical supramolecules from parallel to perpendicular to the surface, for example. Thin films of supramolecule are often processed via solvent annealing, adding an additional component, which will be discussed further in the next section.

The small molecule in both bulk and thin film also introduces a way to easily incorporate NPs. The small molecule can be selected so that it has favorable enthalpic interactions with ligand on the NP. This leads to a way to selectively incorporate the NP into one domain of the BCP as well as ensuring the particle is

well dispersed in the host matrix, no small feat in creating nanocomposites. The incorporation of NPs also affects the entropy during self-assembly, which will be discussed in subsequent sections.

Supramolecules have several advantages in creating nanocomposites: the small molecule leads to inherent tunability in both structure in functionality and can create hierarchical structures. They can also be used to easily incorporate NPs by using a small molecule that is chemically similar to the NP ligand. However, supramolecular nanocomposites are still often limited to structures that are achievable by the phase diagram.

1.3 Structural Control of Thin Films

1.3.1 Solvent Vapor Annealing

Polymer thin films can be processed in a variety of ways: shearing, use of external fields, zone annealing, thermal annealing, solvent annealing, etc[30, 47-52]. Solvent vapor annealing, often referred to simply as solvent annealing, is a preferred method for processing supramolecular thin films. This is due to the thermal volatility of many small molecules. Additionally, solvent annealing will introduce greater free volume as compared to thermal annealing, and can be done quickly and at room temperature[53]. In solvent vapor annealing, the solvent vapor swells the film, increasing mobility at a temperature that is considerably below T_g. This change in mobility is due to a decreasing T_g as follows the Fox equation

$$\frac{1}{T_g} = \frac{w_1}{T_{g,1}} + \frac{w_2}{T_{g,2}}$$

where $T_{g,1}$, $T_{g,2,}$ w_1, and w_2 are the glass transition temperature and weight fractions of component 1 and 2, respectively. Additionally, solvent annealing increases free volume per chain, reducing chain entanglement and increasing diffusion in the polymer system. The addition of solvent will also change χ in the system to an effective χ, which follows $\chi_{eff} = \chi_0(1 - f_s)$ where f_s is the solvent fraction and χ_o is the Flory-Huggins interaction parameter without solvent[54]. As such, when solvent is added, the driving force for separation can decrease in the BCP or supramolecule.

While solvent vapor annealing has been used a processing technique for many years, the process by which it helps supramolecules form long range order, how it affects the kinetics of self-assembly, and, in particular, the role it plays by adding an additional component to a multicomponent supramolecular system, are still largely unexplored.

The use of solvent annealing as a way to create long-range order has been validated in supramolecular thin films with and without NPs. Supramolecule films alone can form long-range ordered lamellae and cylinders with hierarchical structure, *i.e.* lamellae-in-lamellae or lamellae-in-cylinders. The small molecule loading in these systems could be used to tune the orientation of the majority alignment from perpendicular to parallel[46]. Solvent annealing can also access more complicated structures, such as lamellae-in-gyroid[55].

The solvent annealing condition itself can also tune the alignment of the hierarchical structure: by increasing the solvent fraction considerably, the small molecule can align parallel to the cylindrical alignment of the thin films, in contrast to bulk systems, where the short length scale of the small molecule aligns

perpendicular to the longer length scale order formed by the polymer[56]. In a more systematic study, the phase behavior of a supramolecule was investigated on a supramolecule that was on the boundary between forming lamellae and cylinders[57]. It was found that the system could switch between lamellae and cylinders by controlling the solvent vapor pressure of a slightly selective solvent. Furthermore, the solvent annealing condition could be selected so that a terrace-forming structure that contained both lamellae and cylinders were formed at the same time in the same film. The solvent annealing condition, coupled with the film thickness, could also produce either parallel or perpendicular lamellae. Several researchers have validated the use of solvent as a way to change the orientation of the supramolecule[58]. In BCP systems, this is accomplished via surface functionalization so that one or both blocks have preferential interactions. By achieving this control via solvent alone, processing is much simpler, faster, and greater control over the final film is possible. Building on this fundamental work, solvent annealing can also be used to control order-order transitions in supramolecular thin films[56, 57, 59, 60]. Figure 2 shows the order-order transitions possible in one system. The selectivity of the solvent for each of the blocks and swelling ratio was tuned so that the system switched from perpendicular to parallel cylinders, or cylinders to spheres. The pathway was key for controlling the final film features.

Supramolecule thin films with nanoparticles can also be controlled via solvent annealing. One study optimized the solvent annealing condition for the creation of long-range order. It was found that the fraction of solvent present in the film at the end of the annealing process, rather than annealing time, was essential

for dictating the long-range order[61]. The kinetic pathway of the assembly process was directly related to the solvent annealing condition: at low solvent fraction, the film has high activation energy to form an ordered state, but at higher solvent fraction, the activation energy is much lower, resulting in greater long-range order. Understanding the basic kinetic during solvent annealing has also been applied to control the morphology in nanoparticle-containing supramolecular thin films to achieve a non-equilibrium morphology[62]. Supramolecule nanocomposites can also undergo order-order transitions via solvent annealing[63].

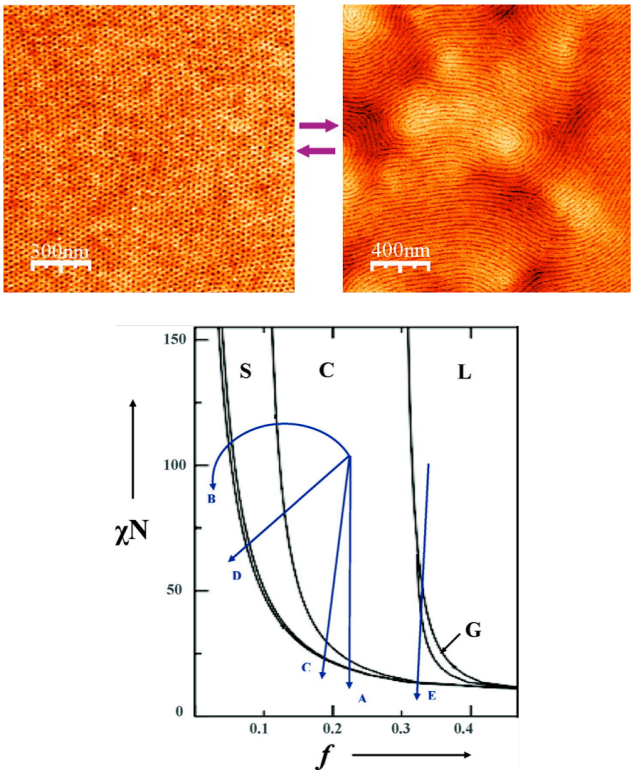

Figure 2: (top) AFM images showing the ability to create long-range order with specific morphology that can be switched by choosing the pathway of ordering during solvent annealing. (bottom) Different pathways are possible during solvent annealing by controlling the selectivity of the solvent as well as the degree of swelling, resulting in order-order transitions. Reprinted with permission from Hur *et al.* ACS Nano, **2018,** 12, 9974-9981. Copyright 2018 American Chemical Society

Non-equilibrium structures can be formed in supramolecular thin films by controlling the solvent annealing condition in conjunction with the pathway[43]. Hexagonal microdomains were formed in thin films by first annealing so that cylindrical microdomains are formed, using solvent to selectively remove the small molecule, and then reannealing briefly. The pathway of assembly, crucially processed via solvent annealing, is can be manipulated to create novel morphologies in supramolecular systems.

1.3.2. Directed Self-Assembly of Supramolecules

Long-range, orientational order of supramolecular systems can be formed by combining the "bottom-up" self-assembly of the polymer system with "top-down" methods for directed self-assembly (DSA)[64]. In top-down assembly, the desired pattern is defined by lithographically created trenches or chemical patterns on the underlying substrate. Both techniques—graphoepitaxy and chemical patterning—have been studied extensively and shown to induce highly ordered systems that align very well with the underlying patterns.

DSA has successfully been used in supramolecular nanocomposite systems. In one study, NPs in a supramolecule were aligned with a linear trench pattern to create a highly aligned pattern in three dimensions. The final film thickness that could be reliably aligned with the underlying pattern was about 7x the trench depth and in trenches of width of about 11 times the equilibrium periodicity of the supramolecule[65]. In a later study, these same supramolecular nanocomposites were shown to have unique optical properties. The difference in interparticle spacing of gold NPs along the trench direction versus perpendicular to it lead to a wavelength-

dependent optical anisotropy. The refractive index showed birefringence and there was also a wavelength dependent reflectivity ratio[61].

Despite these successes, there is a fundamental limitation to self-assembly guided by DSA. This limitation is the need for commensurability: the confining feature (trench width, chemical stripe width) must be an integer multiple of the equilibrium BCP periodicity (L_o). Commensurability has been shown to be needed for alignment of supramolecules on a chemical pattern with and without NPs[66]. However, commensurability has been more carefully examined in BCP thin films.

Commensurability was first studied theoretically in lamellae BCPs confined between two plates[67, 68]. It was shown that the polymer is able to either stretch or compress so that the periodicity would be commensurate with the confinement width to form parallel lamellae, although this is accompanied by a loss of polymer chain entropy. However, if the deviation from the equilibrium periodicity was too great, the lamellae reorient to form perpendicular lamellae to relieve chain deformation. As the spacing between the plates increased, the deviation from the bulk periodicity tended to decrease, since the chain deformation would happen across more layers, and so average out to a small deviation from L_o. These results were also verified experimentally[69, 70].

The need for commensurability has been studied in sphere forming systems confined to lithographically patterned trenches[71]. The number of rows of spheres formed was determined by the confinement width. When the confinement width is within $(0.5\pm n)*L_o$ of the periodicity, where n is an integer and L_o is the equilibrium

periodicity, n rows will form. If the confinement width is ~(0.5±n)*L_o, there will be regions of n rows and regions of either n+1 or n-1 rows.

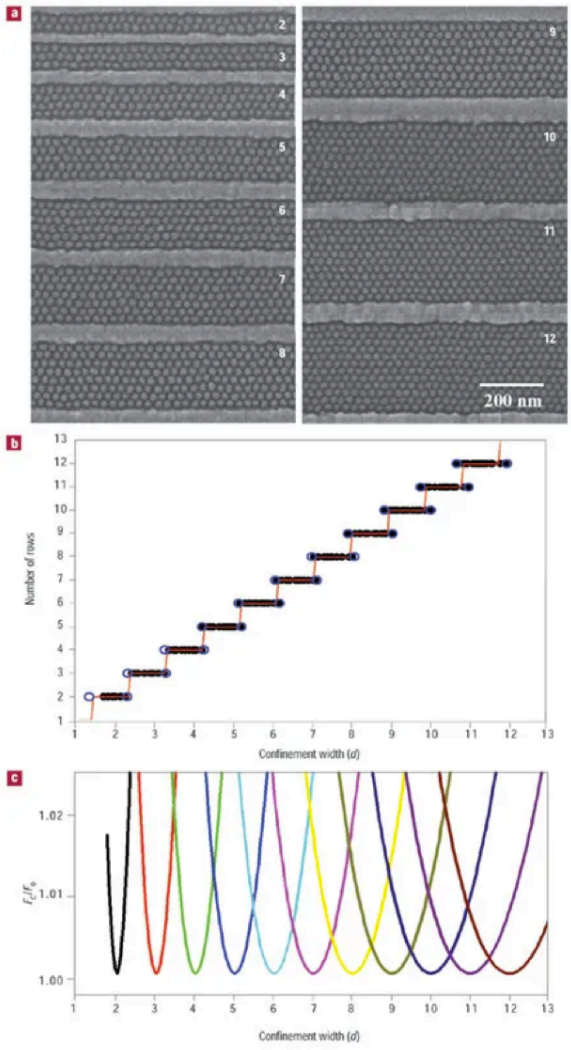

Figure 3: The effect of commensurability on spherical forming BCPs under confinement (a) SEM images of how the spheres align in trench patterns that are different integer multiples of the (b) number of rows formed in trenches as a function of confinement width. In wider trenches, coexistence of multiple number of rows in a single pattern (c) Free energy change as a function of confinement width. The minimum is when the width is an integer multiple of the periodicity. Reprinted with permission from Cheng *et al.* Nat. Mater., **2004,** 3, 823-828. Copyright 2004 Nature Publishing Group

Figure 3 shows that the system has a minimum free energy when the confinement width was an integer factor of the equilibrium BCP periodicity, when there was no chain deformation necessary. For narrower trenches, the free energy increases much faster than for wider trenches as the trench width moves away from the commensurate width, which is due to chain deformation being greater since fewer chains have to compress by more in narrow trenches. Commensurability guides assembly in both physically confined patterns as well as for chemically patterned surfaces. In these systems, a chemical stripe that has attractive energy for one of the blocks is formed on a substrate, often using lithographic methods, to form a heterogeneous structure. If the width of the stripe is commensurate with the width of the BCP block, the BCP will align nicely with few defects, but if the width of the guiding stripe deviates by more than 5-10% of the commensurate condition, the system will not align[72-75].

DSA of geometric patterns has been explored new geometries have been explored using trench patterns, in particular, circular patterns. By confining the BCP in a circular trench, concentric circles or spirals can be formed with changing periodicity and diameter of the rings, depending once again on the commensurability of the polymer with the trench[76, 77]. Chemical patterning can be used to create sharp junctions in patterns. Homopolymer is added to relieve the loss of conformational entropy that the BCP undergoes to stretch around the sharp corner, but the alignment with the pattern is still dictated by commensurability [78].

For all these systems, commensurability dictates whether the system will align with the underlying pattern. It has shown promise for creating highly aligned

systems with few defects in a variety of geometries, however, there is still a fundamental limitation as to what types of patterns and what feature sizes are accessible using DSA for BCP self-assembly. Commensurability relies on the balance of thermodynamic forces (minimization of interfacial energy by aligning and entropic loss due to deviations from the equilibrium periodicity). Opportunities to circumvent this requirement are possible in manipulating the kinetic pathway to create non-equilibrium structures. Supramolecules in particular are a promising candidate for this because the multicomponent system has multiple ways to try and circumvent the limitation on feature sizes imposed by the commensurability requirement.

1.4 Kinetic Considerations of a Multicomponent System

1.4.1 Kinetic Control of Supramolecular Nanocomposites

Recently, a few studies have been conducted into how the kinetic pathway of self-assembly of supramolecular nanocomposite thin films can be tuned for greater control over the final films. The first study investigated the role of solvent annealing on the pathway of assembly and identified the fraction of solvent present in the film (f_s) as a key component for creating long-range order[61]. The kinetic pathway was governed by the energetic costs arising from defects, the chain mobility, and the activation energy of interdomain diffusion. By understanding these processes, assembly with long-range order was found to be achievable in under a minute with complex optical properties. This study highlighted the complexity of manipulating

the assembly process of a multicomponent system and so focused on optimizing the solvent annealing conditions and investigating its effect on the kinetic pathway.

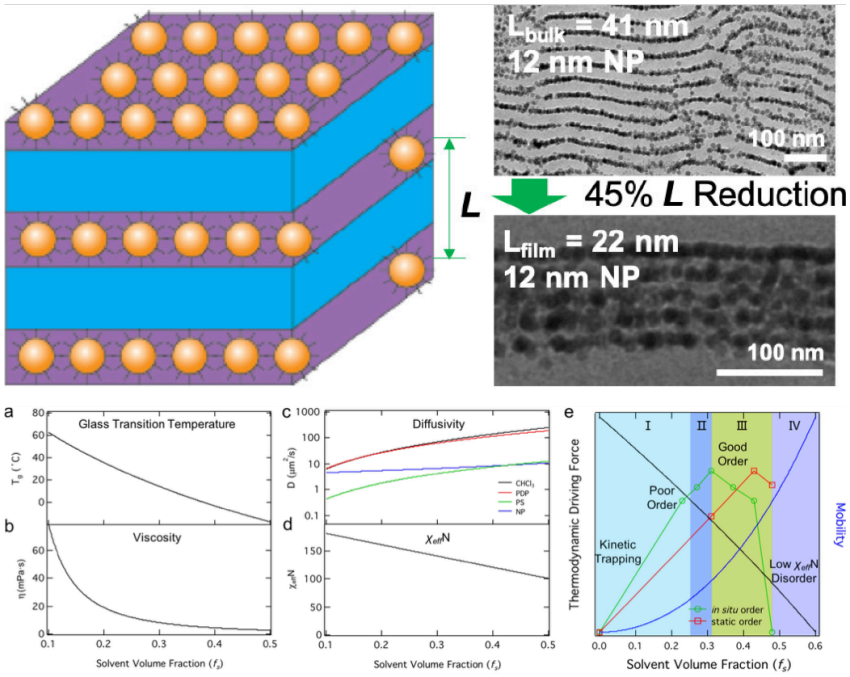

Figure 4: Final film structure of a supramolecular nanocomposite with a 45% reduction in periodicity as compared to the bulk structure. The change in (a) glass transition temperature, (b) viscositiy (c) diffusivity of the components, and (d) thermodynamic driving force for separation, given by χ*N as a function of solvent fraction in the film. This non-equilibrium structure arises from the balance of the kinetics and thermodynamics (e). Reprinted with permission from Huang *et al.* Macromolecules, **2019**, 52, 1803-1809. Copyright 2019 American Chemical Society.

Another study on the same supramolecular nanocomposite system looked at the effect of the solvent removal rate in lamellae forming systems. The final films had a reduction from the equilibrium periodicity of 45%, which was studied using *in situ* GISAXS[79]. The *in situ* studies were crucial to determining the optimal solvent annealing condition prior to rapid solvent removal that balanced the solvent field, short-range diffusion, mobility of each component, and thermodynamic driving

force for order to create films with the same non-equilibrium periodicity for small particles (3 nm) and relatively large particles (12 nm) (Figure 4). By carefully examining how the mobility of the system, given by the glass transition temperature and viscosity of the film, the diffusivity of the various components, and the thermodynamic driving force for separation, given by χ^*N, an understanding of the pathway was gained. Crucially, this insight leads to the ability to control that pathway to create highly ordered thin films with a non-equilibrium periodicity.

The kinetic pathway can also be manipulated in supramolecular nanocomposites to achieve novel structures[62]. Large particles, with a d/L ratio of up to 0.67, were incorporated into a supramolecule system. As discussed earlier, large particles are usually expelled from the polymer matrix when the d/L ratio is above 0.3. These large particles were able to coassemble with the supramolecule by modulating the diffusion of NPs and suppressing surface aggregation via solvent annealing.

A more systematic study was conducted to understand the effect of particle size and supramolecular morphology[80]. Again, given the complexity of the multicomponent system, it is necessary to investigate multiple components at once to see how each component affects the final film structure as well as each other during the assembly process. It was shown that the matrix morphology affected the diffusion of the NPs in the vertical direction. Cylindrical films had fast diffusion due to the continuous pathway, while parallel lamellae films had slow diffusion because of the necessary interdomain crossing. The size of the NP also affected the final

morphology, with larger particles, defined by the d/L ratio, forming a micelle-like structure. The final film structure was directly related to the diffusion of the NPs.

These studies on the whole suggest that the kinetic pathway is a crucial step for controlling the final NP structure. However, this control is difficult in a supramolecular nanocomposite due to the large number of components. However, if the balance between thermodynamics and kinetics of each component can be understood and modulated, designer nanocomposites may be achieved.

1.4.2 Diffusion of Block Copolymers

Insight into the diffusion processes of the BCP is a necessary component for understanding the whole self-assembly process. For the past two decades, researches have attempted to understand how diffusion in BCP systems happens and what mechanisms affect it. Early work focused on self-diffusion of BCPs, that is, how BCPs diffusion in matrices of the same BCP in a bulk sample, generally under thermal annealing conditions. This work is highly relevant for understanding the mechanism of microphase separation as well as how long-range order is created. One paper predicted the mechanism of interdomain crossing in a strongly segregating A-B BCP system[81]. When the A block has to cross through the enthalpically unfavorable B block, it will stretch out considerably, pulling a given number of monomers through the block in a multistep process. By stretching out, the system loses entropic free energy, but also minimizes the unfavorable enthalpic interaction. In doing so, the activation free energy of interdomain crossing scales as $F\sim(\chi N)^{2/3}$, as opposed to if the BCP diffused as a coil, which would scale as $F\sim(\chi N)$. It was noted that this mechanism of diffusion is still slow and has a high energy

barrier. It is also important to note this mechanism is only true of strongly segregating systems, and most systems follow $F \sim (\chi N)$.

Further studies probed the mechanism of self-diffusion further. Given the inherent anisotropy in lamellar systems, it is expected that the diffusion processes will be different. The diffusion coefficients along the BCP domain (D_{par}) and the diffusion coefficients across the BCP domain (D_{perp}) were studied to quantify the relative speeds to the two types of diffusion. Experiment validated theoretical predictions that D_{par} is a much faster than D_{perp} since interdomain diffusion is much more energetically costly and scales as $D_{perp} \sim D_o \exp(-\alpha \chi N_A)$ [82, 83]. Here, N_A is the number of monomers in the A block and α is an experimentally determined parameter close to 1. This model is referred to as "hindered diffusion," that is, diffusion that is hindered by the enthalpic penalty of interdomain crossing. The ratio of D_{par} to D_{perp} can be as high as 40 in lamellar systems[84]. For cylinders, this same anisotropy exists. In unentangled systems, the anisotropy of diffusion increases as χ increases as D_{perp} increases and D_{par} remains essentially constant. The ratio of D_{par} to D_{perp} can be as high as 80[85, 86]. The degree of alignment of the cylinders and its effect on the diffusion was examined[87]. It was found that D_{perp} was strongly dependent on the degree of alignment: as the degree of alignment increased, D_{perp} increased, in some cases, becoming similar to D_{par}. This was attributed to the presence of defects, such as dislocations. If there is, for example, a forked dislocation, it may be faster for the BCP to diffuse through the fork, rather than go around it, increasing the apparent D_{perp}. D_{par} was found to have very little dependence on the degree of alignment of the cylinders. In spherical systems, there is only one diffusion

coefficient, D_s, which involves interdomain diffusion. This too follows the scaling law $D_{perp} \sim D_o \exp(-\alpha \chi N_A)$[88-90]. The hindered diffusion model is shown to be fairly universal, with diffusion across domains to be much slower than along domains or in a freely diffusing system. The diffusion slows with increasing χ and increases with increasing temperature. The diffusion in a gyroid system has also been measured[86]. As a continuous network, there is no need for interdomain crossing, so there is only one diffusion coefficient, but if follows a separate scaling law. Rather than depending on χ, the diffusion coefficient is similar to parallel diffusion in a cylindrical system, albeit scaled down slightly due to the tortuosity.

The previously described studies were all carried out on low molecular weight systems, with no entanglements. The dynamics in entangled BCPs was also investigated. Initially, the diffusion in disordered lamellar systems, with microphase separation but short and multiple lamellae grains, was investigated[91]. Since the system was disordered, the diffusion coefficients measured were a combination of D_{par} and D_{perp}. It was found that for unentangled systems, the diffusion scales as $D \sim M^{-1}$, where M is the molecular weight of the sample, which is expected for Rouse dynamics of unentangled polymers. The lamellae had no effect on the unentangled system dynamics. However, for an entangled system, the diffusion does not scale as $D \sim M^{-2}$ as is expected for homopolymers undergoing reptation dynamics as is expected for entangled polymers. Instead, the lamellar structure affected the ability of the polymer to diffuse, slowing down the dynamics of the system. A more careful investigation into the effect of entanglements on D_{par} and D_{perp} was performed on lamellar systems[92, 93]. In entangled systems, the primary mechanism of motion is

reptation. In reptation, a "tube" is formed by the entanglements through which a single polymer chain can diffuse in one direction. As the polymer moves, the chain end undergoes a random walk and finds the best way for a new tube to be created. In BCP systems, this mechanism is complicated by the two (or more) chemically distinct domains, so that there is an enthalpic penalty associated with crossing domains. This model is extended to an "activated reptation" model to take into account the changing energetic considerations of a BCP system. As compared with "free" diffusion in a system where χ=0, $D_{perp}/D_o \sim \exp(\chi N)$, so that the limitation of interdomain diffusion is enthalpic in nature. By contrast, D_{par} is independent of χ, and instead scales as $D_{par}/D_o \sim \exp(N/N_e)$ where N_e is the number of monomers between entanglements. The proposed mechanism to explain D_{par} is entropically related, the arm-retraction mechanism. Here, neither the A and B block do not cross into the opposite block (explaining the independence from χ), but instead, to move along the interface, the A (or B) chain must retract through the entangled matrix to be in the interfacial zone, then reextend to a new configuration. This process is expected to be very slow. In unentangled systems, $D_{par}/D_o \sim 1$. The addition of entanglements significantly slows down diffusion in both D_{par} and D_{perp}, resulting in less of a difference between the two mechanisms (smaller anisotropy). In cylinders, the same change in dynamics and mechanism with respect to D_{par} in entangled systems is seen[86, 87].

While there have not been any systematic studies that investigate the diffusion of supramolecules, the findings from BCP are relevant, as the same arguments for energy barriers for parallel versus perpendicular diffusion will apply.

However, the small molecule may be able to modulate the interfacial interactions and so either help or hinder diffusion in supramolecules. It has been shown that, under solvent annealing, the mobility of supramolecules depends on the fraction of small molecule added to the supramolecule and that the addition of any small molecule increases the mobility of the system considerably[56, 57].

1.4.3 High Molecular Weight-Based Nanocomposites

One of the inherent limitations of using a BCP-based supramolecule is the size range of the periodicity. Generally, BCP-based systems are limited to a periodicity between 10-50 nm. It is difficult to get very small or very large periodicities. From theory, it has been determined that the periodicity, L_o, $\sim \chi^a * N^b$, where a and b depend on whether the system is in the weak, strong or super strong segregation limit[94]. For the weak segregation limit, where $\chi*N \sim 10.5$, a=1/3 and b=1/2. For the strong segregation limit, where $10.5 << \chi*N << 100$, a=1/6 and b=2/3. For the super strong segregation limit, where $\chi*N >> 100$, a=0 and b=1. Despite these predictions, there are fundamental kinetic limitations that prevent large periodicity from being achieved.

Many of the features that control the self-assembly process are molecular weight dependent: diffusion of the polymer, degree of entanglement, and viscosity of the system. As such, getting features larger than around 50 nm is difficult even if the driving force is quite high ($\chi*N >> 10.5$). In order to circumvent kinetic limitation, several strategies have been examined. Adding a homopolymer to the BCP can swell the domain size, but the molecular weight and amount of homopolymer added must be carefully chosen so the system remains miscible[95-98]. This method was first

adopted to make tunable bulk BCP photonic crystals. Tunability across the entire visible wavelength in photonic crystals was achieved by adding between 5-50 wt% of equal amounts of polystyrene and polyisoprene to a lamellae forming polystyrene-polyisoprene system[99, 100]. The homopolymers chosen were of a considerably smaller molecular weight than the BCP: each hompolymer was ~13 kg/mol and the total molecular weight of symmetric BCP was 391 kg/mol. In this regime, the homopolymer is able to "wet" the BCP since the much smaller size of the homopolymer means it is uniformly spread throughout the BCP domain. Later studies have investigated the kinetics of such systems in thin film, showing that ternary polymer systems in this regime have enhanced kinetics as compared to neat BCP systems alone due to the lowering of energy barriers of the distributed, small, homopolymer[101].

Solvent can also be used as a way to induce order in high molecular weight systems. Initial studies looked at the crystallization of solvent as a way to produce long-range order in high molecular weight thin films[102]. The directional solidification of benzoic acid produced highly oriented microdomains in both perpendicular lamellar and parallel cylindrical BCPs. The orientation of the BCPs in the high MW regime were almost 90 degrees off from the orientation of the BCPs in the same system for the low MW regime, which was attributed to slower diffusion, an earlier onset of an order-disorder transition, and decrease in solubility due to higher MW system. A simple solvent annealing method was used to create high molecular weight based gyroids for use in membrane applications[103]. A long annealing step (100-200 minutes) with a neutral solvent was used in a chamber

with a regulated temperature gap between the top and bottom. This set-up allows for increased mobility in the high MW system, while still maintaining a high driving force for separation. The key for creating a long-range ordered system was increasing the mobility of the system. This means that supramolecules could have a fundamental advantage over BCPs: the small molecule can act as a selective solvent to decrease entanglement, lower viscosity, and increase free volume and mobility. This has yet to be explored.

A more explicit coupling of solvent and thermal annealing methods was used for long-range order in DSA of perpendicular lamellae systems with a periodicity of up to 200 nm[104]. Here, a solvent annealing step is followed by a thermal annealing step. This process produces uniform thin films with long-range order. During the solvent annealing process, the defect density decreased with increased solvent annealing time, while the thermal annealing process did not greatly affect the defect density. However, the periodicity of the BCP increased considerably during the thermal annealing process from the periodicity set by the solvent annealing process. This was attributed to a "re-equilibration" process of the block size by increasing short-range segregation. This process was seen in multiple high molecular weight BCPs. The high molecular weight BCPs were able to align with linear trench patterns using this method as well.

Bottle-brush BCPs have also been adopted as a way to create large periodicity structures without the kinetic limitations of high molecular weight linear polymers. These polymers are constructed from grafting a polymer side chain to the backbone. The dense packing of the side chains and elongated nature of the

backbones significantly decrease the chain entanglement, thus changing the kinetic regime. Self-assembly is very rapid in these systems. It has been shown that the periodicity scales with the number of monomers in the backbone, since the backbone is stretched out enough that its length is essentially equivalent to the contour length[105]. Lamellar, cylindrical, and spherical morphologies with feature sizes of greater than 100 nm have been demonstrated, which are tuned by changing the graft length so that there must be curvature of the shorter length block to accommodate the interfacial area mismatch[106-108]. This method is compatible with NP incorporation[109]. The side chain length can be modulated so that NPs either will incorporate throughout a domain or at the center of the domain, so that NP placement can be controlled.

1.4.4 Defect Annihilation in the Self-Assembly Process

Another area of kinetic consideration is defect annihilation in supramolecular systems. The creation of long-range order is only achievable via annihilation of defects such as disclinations and dislocations. The pathway of defect annihilation in BCPs has been studied theoretically and experimentally. Unfortunately, no such studies exist for supramolecules, or nanocomposites. However, the pathway should be similar, albeit the exact thermodynamics will change due to the incorporation of a small molecule.

Defects create a greater interfacial area, so they are thermodynamically unfavorable, but their annihilation is a kinetically limited process. Depending on the type of defect, the pathway of annihilation will change. In general, however, defects are paired and must find each other before they will be annihilated[110-112].

Theoretical studies have determined the energy pathway of annihilation of defect pairs in BCP systems that have been self-assembled on chemically patterned substrates using self-consistent field theory and verified with some experimental evidence[113, 114]. Figure 5 shows the energy pathway of a very simple defect, a disclination dipole in a lamellae forming BCP during thermal annealing. In the annihilation of this defect, increased interface is formed, which is energetically unfavorable, leading to an energy barrier for the formation of transition states necessary to ultimately annihilate the defect. For defects that are further apart, there are more transition states, and each time, the system must overcome an energy barrier for the defect to be annihilated. The transition time is proportional to the energy barrier height, thus films are often in a kinetically trapped state.

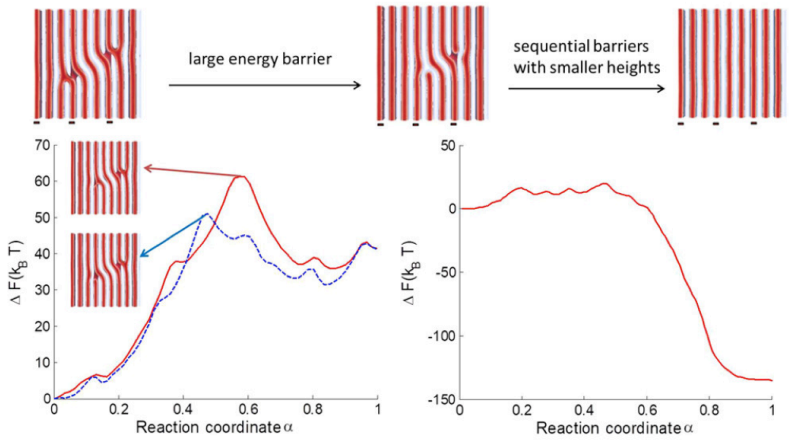

Figure 5: The activation energy needed at each step of defect annihilation for (left) disclinations to move from far away to right next to each other and (right) disclinations once they are next to each other. Reprinted with permission from Hur *et al.* ACS Nano, **2018**, 12, 9974-9981. Copyright 2019 American Chemical Society.

Several experimental papers have investigated the pathway of defect annihilation by directly tracking defects using methods such as atomic force microscopy (AFM) on flat substrates as well as in DSA systems. Early studies focused on identifying the

mechanism of defect annihilation and found that several metastable states were formed on the pathway to a defect-free region[115]. It was also found that defects that were closer together were annihilated more quickly[116].

The pathway of defect annihilation depends on the type of defect, as well as how far away to the defects are from each other. Before defects are annihilated, they can move positions in a thin film, which often results in pairs being brought closer to one another. The mobility of the defect will depend on the type, but in general, there will be a flow of defects, suggesting that defect motion is correlated across a large area (micron scale). The motion of defects prior to annihilation follows Arrhenius behavior[117]. That is, the activation energy of defect mobility can be calculated.

A more thorough understanding of the mechanism of defect annihilation was determined by tracking defects in cylinder forming BCPs that were confined in a linear trench pattern[118]. Two primary mechanisms were determined for defect annihilation and the growth of long-range order: climb and glide[117, 119]. Climbing is defined as BCP motion parallel to the BCP interface, and gliding is defined as BCP motion perpendicular to the BCP interface. As discussed in a prior section, the relative energy barriers between the two is expected to be quite different, which was verified using *in situ* AFM during thermal heating. Climbing was found to happen very quickly, with a much higher diffusion coefficient. Gliding was much slower[118]. For single point defects, one of these mechanisms was usually sufficient to annihilate the defect.

Defect annihilation studies are important for understanding the kinetics associated with forming long-range order. The orientational correlation length can

stand in as a measure for the average spacing between defects. The more defect there are, the shorter the correlation length will be[120]. By plotting this correlation length versus time, the rate at which disclinations are annihilated can be plotted, which give a view of the energetics required to form a perfectly ordered structure. The annihilation of disclinations will follow a power law[117]. This power law was seen in lamellar, cylindrical, and sphere systems[111, 121]. The exact power law changes depending on the morphology as well as the χ_{eff}[122, 123]. The power law may be system dependent, but can be used to compare across BCP systems and compare how easy or difficult it is to annihilate defects. Supramolecular systems will likely follow similar pathways of defect annihilation, but the rates of defect annihilation will likely be different.

1.4.5 Polymer Diffusion in Nanocomposites

Once NPs are added to a polymer, the dynamics of the polymer will change considerably. Studies into polymer chain dynamics and diffusion in nanocomposites has so far been limited to homopolymer matrices or polymer grafted NPs. However, polymer diffusion in homopolymer-based nanocomposites can still inform the considerations needed to understand the overall kinetic picture of a multicomponent polymer nanocomposite.

Initial studies into polymer chain dynamics in nanocomposites were conducted via simulation. Using Monte Carlo simulation, it was found that, in a system where the NP was considerably larger than the polymer chain, the polymer chain forms a densely packed shell on the surface of the particle, and that the polymer chains often bridged multiple particles[124]. As a result, the particles acted as

effective crosslinking agents, slowing the diffusion of the polymer system. Smaller particles had a more pronounced effect on slowing down the dynamics of the polymer system.

The type of interaction of the particle/polymer also affects the dynamics. Using a molecular dynamics simulation, it was found that diffusion of the polymer in a nanocomposite is determined by whether the interaction between the polymer/particle is repulsive or attractive[125, 126]. When the polymer/particle interaction is attractive, the diffusivity of the polymer chain is decreased relative to the polymer bulk value, and when the interaction is repulsive, the diffusivity of the chain is increased relative to its bulk value for a system where the particle size is on the same order as the radius of gyration (R_g) of the polymer with low particle loading (>10v%). However, this change in diffusion is only near the surface of the particle: approximately one R_g away from the surface, the diffusion of the polymer chain becomes approximately the same as the bulk value.

The dynamics of the polymer chain will change depending on the loading of particles as well as their size. The effect of polymer loading and interparticle distance on polymer chain diffusion was studied experimentally in a polystyrene/silica NP system[127]. The volume fraction of the particles in a system was varied from 1v%-50v%. A sample with a thin deuterated polystyrene (dPS) polymer film deposited onto a bulk PS sample was thermally annealed. The distance the dPS had traveled after the annealing step was measured, and from that, a diffusion coefficient was determined. It was found that the diffusion of the tracer polymer decreases as the NP loading increases, with an even more pronounced

effect when the tracer polymer molecular weight is higher. It was determined that the confinement of the polymer between particles is what affects the ability of the polymer to diffuse. This is consistent with the entropic barrier model: slower diffusion in the presence of NPs is attributed to the loss of entropy that goes along with a polymer chain deforms to squeeze between two neighboring NPs. The temperature dependence of the change in diffusion coefficient as the NP loading increases has also been studied. At high temperatures, the diffusion coefficient decreases more sharply with increasing particle loading, which is also consistent with the entropic barrier model[128]. The effect of increasing confinement, that is, decreasing interparticle distance, on decreasing the polymer diffusion coefficient has also been described theoretically[129].

The size of the NP and NP polydispersity also affect the diffusion of a polymer through the matrix[130]. At a given volume fraction, smaller NPs will lead to faster diffusion of the polymer because the interparticle distance will be smaller, so the confinement the polymer feels will decrease. Polydispersity of NP size will also affect the interparticle distance: systems with large polydispersity will have greater interparticle spacing, and so the diffusion of the polymers in those systems will be increase. Once again, the experimentally determined diffusion parameters can be explained by slower polymer dynamics due to the entropic loss of the confinement between NPs.

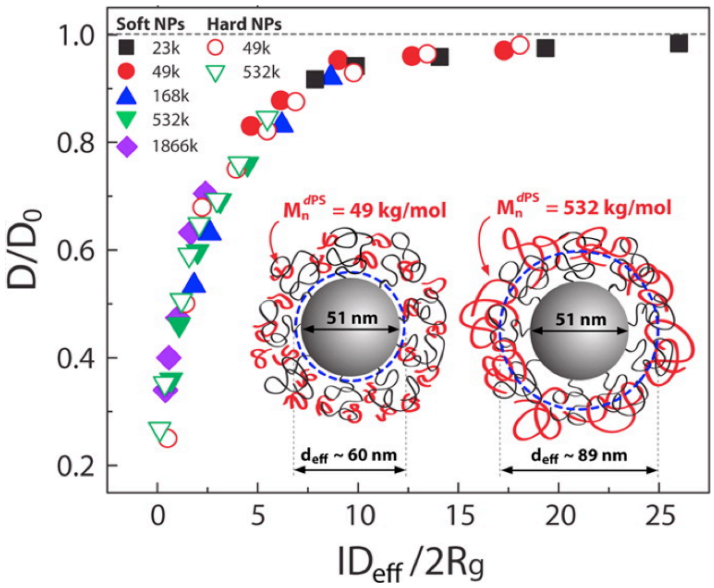

Figure 6: Effect of confinement parameter. The reduced diffusion coefficient (D/D_0) of the polymer of different molecular weight function of the confinement parameter $ID_{eff}/2R_g$yields a master curve. Inset illustrates how penetration of the tracer into the polymer brush decreases as the tracer size increases which results in closer effective spacing of NPs (i.e., ID_{eff} decrease). Reprinted with permission from Choi *et al.* ACS Macro Lett., **2013** 26, 485-490. Copyright 2013 American Chemical Society

The degree of confinement can represent a universal way of understanding polymer diffusion in nanocomposites[131, 132] (Figure 6). By plotting the normalized diffusion coefficients (D/D_o, where D_o is diffusion in a bulk polymer matrix) against the confinement parameter ($ID/2R_g$, where ID is the interparticle distance and R_g is the radius of gyration of the probe polymer), a master curve can be created, showing that the confinement parameter captures the effect of NP size, polydispersity, and volume fraction of particle loading. In a PMMA/silica system, the diffusion coefficient was decreased by 80% relative to the bulk diffusion when $ID<2R_g$. When $ID>2R_g$, the change in diffusion is more moderate, up to 15%, but the effects are felt as far away as when the interparticle distance is eight times larger than $2R_g$, suggesting far ranging effects of including particles.

The idea that the degree of confinement is key for determining the diffusion of the polymer has been confirmed using neutron scattering on a poly(2-vinylpyradine)/silica sample[133]. Neutron scattering is able to provide spatial and temporal information on a small length scale and fast time scale, so additional insight is possible, such as how the segments diffuse, rather than simply looking at average movement of the entire chain in time. The average segment diffusion coefficient of the segment was found to decrease monotonically with increasing NP concentration, which corresponds to decreasing particle distance. The segmental diffusion was determined to follow classical translational diffusion under extreme confinement conditions, where the interparticle distance was on the scale of the Kuhn monomer. The segmental dynamics were found to only depend weakly on the molecular weight, which was unexpected given the well-documented change in dynamics in highly entangled systems. This suggests that there is still much work to be done to understand polymer diffusion in nanocomposites.

The shape of the particle can influence polymer chain dynamics as well. Up to this point, all the particles discussed have been spheres. However, the shape of the NP has been shown to be key in influencing polymer diffusion in polymer nanocomposites. Nanorods (NR) were dispersed in a polystyrene matrix at loadings from 0-10v%, and four different molecular weight tracers were used to determine the effect of the relative size of the tracer and NR size on diffusion. For NRs whose length is 371 nm, low NR loadings lead to a decrease in the diffusion rate, regardless of the molecular weight of the tracer polymer. In dilute systems, NRs act as barriers that must be circumvented. For these NRs at high loadings, the change in the

diffusion of the tracer polymer depends on its molecular weight. Low molecular weight tracers continue to have smaller diffusion coefficients as the NR loading increases. The diffusion coefficient of high molecular weight tracers, however, begins to increase and reaches the bulk value of polymer diffusion as the NR loading increases. The high molecular weight tracers have an R_g on the same order as the radius of the NR, so that the chain dynamics will be more expanded, making diffusion easier. The onset of the recovery of the diffusion coefficient is at the same loading necessary to make a percolation network. For shorter NPs, some recovery of diffusion is possible once a percolative network is formed as well for the lower molecular weight tracers, where the length of the rod is greater than $2*R_g$ of the tracer. The non-monotonic behavior is attributed to differences in diffusion in the direction perpendicular to the rod (slow) and diffusion in the direction along the rod(fast), as well as the relative amount of monomer friction.

1.4.6 Diffusion of Nanoparticles in Nanocomposites

The addition of NPs also affects the kinetics of self-assembly. NP diffusion occurs on a different timescale than polymer diffusion. NP dynamics can be quite variable and have different effects on the matrix overall, depending on the size, shape, and polymer matrix characteristics. One key to understanding particle dynamics in polymers is to understand the effect of NPs on the viscosity of the polymer. As the viscosity decreases, kinetics will be enhanced, following time-temperature superposition.

Early work on this subject discovered that NP diffusion in a polymer matrix deviates significantly from what is expected from Einstein-Stokes diffusion.

Einstein-Stokes diffusion, the classical model for describing diffusion of a hard sphere in a viscous medium, predicts that the viscosity of the system should increase when particles are added. However, that is not always the case. In a PS polymer with NPs created from crosslinked PS, the viscosity of the polymer decreased upon addition of the NPs[134]. This system was chosen to eliminate enthalpic considerations as well as to maximize dispersion in the system. The viscosity was found to decrease by as much as four times, even though Einstein dynamics predict an increase in viscosity. It was also found that the T_g decreased as NPs are added, despite the fact that the NPs had almost identical T_g to the polymer matrix. This leads to the assertion that the viscosity decreased with the change in free volume introduced by the NPs. The NPs, however, did not appear to reduce entanglements of long polymer chains.

The lowering of viscosity when particles are added has also been seen with inorganic particles. Initially, this phenomenon was measured in PDMS with silicate particles, where the particles were very small, on the order of the size of the polymer monomers[135]. Thus, this finding was attributed to the particles acting like small molecules rather than colloidal, hard particles. In a study that looked at quantum dots in a PS matrix, the diffusion coefficient of the polymers was found to be 200 times faster than the expected Stokes-Einstein diffusion coefficient[136]. In this case, the cadmium selenide NPs were 4.7 nm in diameter in a high molecular weight, entangled polystyrene system where the radius of gyration is 17 nm, larger, but on approximately the same scale, as the NPs. The tube diameter of an entangled mesh of PS is approximately the same as the NP diameter. The explanation for the

decreased viscosity is due to the differing length scales of polymer chain relaxation and NP diffusion. NPs of this size are able to move tens of nanometers in the time it takes a polymer chain to relax. Thus, they do not participate in the dynamics of the entangled mesh. Instead, they provide a constraint release mechanism, in addition to adding free volume to the system, to lower the viscosity. The explanation for why NPs lower viscosity is related to the nanoscale viscosity and frictional forces rather than the global frictional forces. Small NPs only experience the micro/nanoscopic viscosity from the local polymer environments, which is smaller than the overall bulk viscosity.

The previous studies looked at relatively small particles. The size of the particles, particularly in relation to the size of the polymer, will affect the dynamics of the NPs. Several studies have investigated the onset of Stokes-Einstein diffusion in polymer nanocomposites as function of particle size. From these studies, a relationship between the polymer radius of gyration, polymer radius, and entanglement mesh size can be determined. For unentangled polymers, when the particle radius is larger than the radius of gyration, NP diffusion follows Stokes-Einstein diffusion and the viscosity of the system increases upon addition of the NPs[137]. For entangled polymers, if the particle is smaller than the entanglement mesh size, it will deviate from Stokes-Einstein dynamics[137]. The recovery to Stokes-Einstein diffusion is slow, and requires the particle size to be between 2-10 times the size of the entanglement mesh diameter[138].

Overall, the diffusion behavior of each component in a polymer nanocomposite is complex, with several competing processes occurring

simultaneously that ultimately drive the self-assembly process. It is difficult to know exactly what is happening at each stage, highlighting the need for more thorough studies.

1.5 Characterization Using *In Situ* X-Ray Scattering

Despite its widespread use, the exact pathway taken during solvent annealing is still unknown in supramolecular nanocomposites. The best way to tackle this problem is to conduct systematic *in situ* scattering studies, where the changes in structure can be tracked and correlated with solvent content. Unfortunately, there is still a large gap in these types of studies in the supramolecule and nanocomposite community. Some studies have been conducted on BCP systems without NPs. While the pathway of the supramolecule is expected to be very different due to the small molecule, the results from BCP *in situ* studies are still instructive and thus will be reviewed here.

For polymer nanocomposite thin films, grazing incidence small angle X-ray scattering (GISAXS) is the most commonly used technique *in situ* technique. *In situ* experiments have yielded insight into the pathway during self-assembly, revealing states that previously were unknown. The change in periodicity, structure, and underlying polymer chain dynamics can be revealed by *in situ* GISAXS.

Initial studies looked at lamellar block copolymers during solvent vapor annealing[139, 140]. From these experiments, distinct kinetic regimes at different points in the annealing process can be identified that correlate to molecular motion. During the annealing stage, three different kinetic steps were identified: polymer swelling

and uniaxial block stretching, followed by block relaxation, polymer chain rearrangement to a globular state, and periodicity decrease due to a lowered χ_{eff}. In this phase, the interfacial area between the two blocks is quite large due to the more coiled polymer conformation, which causes instability in the system. This instability leads to the rearrangement of the blocks and the formation of new layers of lamellae. Finally, the periodicity stabilizes. The pathway described here is not obvious from simply looking at the starting and final morphology of the system, highlighting the need for *in situ* studies. Further studies examined the relative rate of periodicity change in parallel lamellae versus perpendicular lamellae. It was found that parallel lamellae grow very quickly, due to smaller periodicity initially set by the spin casting step, although ultimately, one periodicity was achieved.

The drying process was also investigated in lamellae. During the drying process, the periodicity decreases. Initially during drying, the decrease in periodicity is not as large as would be expected from solvent leaving. This is due to chain stretching occurring at the interface as χ_{eff} begins to increase again as the solvent content becomes smaller. In the final phase, the system is below the T_g and thus decrease of the lamellae is due simply to the solvent evaporation. The discrepancy in swelling of the differently oriented lamellae gives insight into the mechanism by which ordering happens and the key role of solvent on influencing dynamics is clear in this work.

In situ studies were also performed to compare solvent annealing to thermal annealing and how the processes may differ for hexagonally packed cylindrical samples during solvent annealing and drying[141]. Ultimately, it was determined that

the greater mobility given by solvent annealing lead to larger grain sizes at the end of the annealing process. During the drying process, the periodicity of the solvent annealed sample becomes larger than the periodicity of the thermal annealed sample. This is once again attributed to the greater mobility that the solvent gives the system, even at low solvent fractions, so that the chain could stretch away as χ_{eff} increases and the interfacial area becomes unfavorable. These observations are in qualitative agreement with the ordering processes in the lamellae system. Here, the important contribution is to note that solvent annealing enhances polymer chain dynamics, which can lead to long-range order on short time scales.

As described previously, solvent annealing can change the pathway of assembly and produce order-order transitions. By using a selective solvent or a non-selective solvent, different pathways can be accessed resulting in different morphologies and can be reversibly switched[142]. In a poly(methylstyrene)-b-poly(hydroxystyrene) system, solvent annealing using a non-selective solvent was able to induce an ordered structure, and force a transition between perpendicular to parallel cylinders. The pathway of this transition was that perpendicular cylinders are initially formed, followed by the disappearance of these cylinders as solvent annealing continues, and then the perpendicular cylinders appear. In a selective solvent, the pathway is different. The initial structure formed is parallel cylinders, which transition to body-centered cubic (BCC) spheres, and then to face-centered orthorhombic (FCO) spheres as the solvent is taken up by the polymer and the volume fraction of the blocks shifts. The morphology is reversible and can be controlled: films that have been annealed using the non-selective solvent can then

be annealed by the selective solvent and go through order-order transitions associated with that annealing step, as well as the reverse. The starting morphology of the film (as cast or already highly ordered) does not ultimately influence the final film morphology, but rather the type of solvent does. The morphological changes were found to happen at specific swelling ratios, not as a function of time annealed, and can result in highly ordered structures of different morphology. Polymer systems that undergo order-order transitions across all common BCP morphologies simply by tuning the solvent annealing process have also been shown, providing insight into how transitions across all phases occur and the power of solvent annealing for use in morphological control[143].

The drying process post-annealing also affects the final film features. The rate at which solvent is removed can influence the final film features. Instantaneous versus slow solvent removal can result in a change in the periodicity and grain size of the BCP[144] (Figure 7). If the solvent is removed instantaneously, the periodicity will change little because the system is in a kinetically frozen state. Generally though, the periodicity will increase. If the solvent is removed quickly, but not instantaneously, the periodicity will increase by more. If the solvent is removed slowly, the periodicity will increase significantly. As the solvent content in the film decreases, the χ_{eff} will increase. With slow solvent removal, the chains have the time and mobility to stretch away from each other to the more thermodynamically favorable conformation and so the periodicity increases. In a BCP system that forms spheres, the solvent removal process revealed a unique pathway[145].

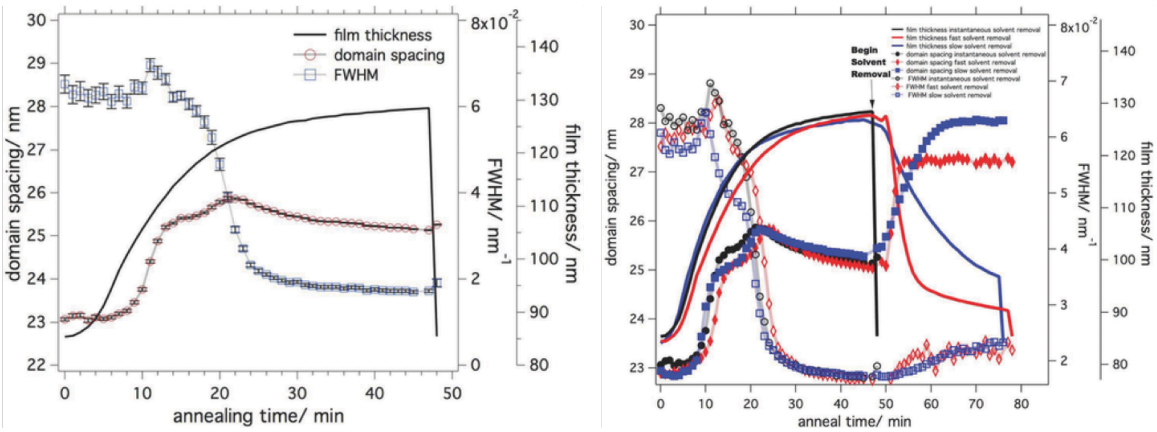

Figure 7: (left) The change in periodicity of a BPC and sharpness (given by the full width at half max) of the scattering peak produced during *in situ* solvent annealing. (right) The change in periodicity of a BCP and sharpness of the scattering peak during *in situ* annealing and drying as a function of solvent removal rate. Adapted with permission from Gu *et al. Adv. Mater.*, **2013,** 26, 237-281. Copyright 2013 Wiley-VCH Verlag GmbH & Co. KGaA, Weinheim

At the end of the annealing process, the system forms hexagonally packed spheres. During fast drying, the system transitions to a short-lived orthorhombic sphere structure that then transitions back to the hexagonally packed phase. This intermediate structure would be unknown without *in situ* studies. Upon slow drying, the final film morphology is a mixture of hexagonal and orthorhombic spheres.

In situ studies are important because they can yield insight about the pathway, chain dynamics, and reveal information about how the system orders that is not apparent from the starting and final film features. Both solvent annealing and drying can be used as a handle to control the pathway of the film and are key for understanding the final film morphology.

1.6 Conclusions and Outlook

Supramolecular nanocomposites have been widely studied due to their ability to form hierarchical structures on the nanoscale for a wide-ranging variety of applications. However, they are complex systems, with four or more components. This complexity offers opportunity for tuning the functionality and film features via changing the small molecule, polymer backbone, processing conditions, etc. However, this complexity means much is still unknown as to what is possible to achieve in thin films. Understanding the kinetic pathway during assembly will be crucial to achieve control over supramolecular nanocomposites. This thesis will begin to fill in gaps of knowledge that exist in understanding the kinetic pathway of supramolecular nanocomposite self-assembly.

The work described in this dissertation examines the kinetic pathway of assembly of supramolecular nanocomposite thin films. This multicomponent system has complex assembly processes, so the factors that can be used as handles to create tunable films have been investigated. This starts in Chapter 2 where the effect of the small molecule and solvent annealing condition on the final film morphology on flat and patterned surfaces was examined in systems without NPs. Chapter 3 extends the study of directed self-assembly on circle patterned substrates both with and without NPs. Chapter 4 examines a new kinetic regime with using high molecular weight based supramolecules and large (>10 nm) particles to access larger length scales than is typical in BCP-based assembly. Finally, in Chapter 5, *in situ* X-ray scattering using the new technique grazing incidence transmission small angle X-ray scattering (GTSAXS) is used to monitor the kinetic pathway of assembly during

controlled drying of a nanocomposite thin film. This dissertation should begin to create a roadmap for how to manipulate the kinetic pathway to control the structure in tunable thin film nanocomposites.

Chapter 2
Self-Assembly of Supramolecular Thin Films: Role of Small Molecule and Solvent Vapor Annealing

2.1 Introduction

Block copolymer (BCP)-based supramolecules are advantageous for forming hierarchically structured materials and incorporating functionalities without synthetic complications[1-6]. They have been extensively studied in the past two decades in bulk and thin films. The complexity of these supramolecular systems is obvious: they are constructed by non-covalently attaching small molecules to a BCP block. As a multi-component system, their phase behavior depends on interplay of different thermodynamic driving forces as well as the assembly processes. Much of the research in the field of supramolecules has focused on two key areas: how to control the nanoscale structure and how to introduce functionality[7-13]. For both of these purposes, all results indicate that the small molecule is key in differentiating supramolecules from traditional BCPs. Initial studies in bulk systems of supramolecule systems showed that incorporating small molecules was able to create hierarchical structures, such as lamellae-in-lamellae and lamellae-in-spheres, due to the shorter length scale packing of the small molecule within the larger length scale microdomain of the BCP[2, 14, 15]. The small molecule is also able to change the phase diagram by stabilizing semi-equilibrium states such as hexagonally perforated lamellae, generate gyroid structures over a wider range, and generate non-equilibrium structures[14, 16-18]. The small molecule can be used to easily introduce functionality without complex synthesis, including liquid crystals and organic semiconductors[19-23]. Liquid crystal-based supramolecules have been shown to introduce photophysical properties and make supramolecules responsive to external fields[23-28]. Organic semiconductors can be used to implement optical and

electronic properties into simple polymer systems[29-31]. The small molecule can also be used to create stimuli-responsive systems, such as thermal switchable photonics or thermally switchable electrical conductivity[3, 32-35].

Supramolecular thin films are often solvent vapor annealed due to the thermal volatility of small molecule. The presence of solvent introduces more complexity since affects both the thermodynamics and kinetics during the self-assembly process. Solvent annealing has been used to tune morphology without changing the BCP composition by altering the volume fraction of one block or solvent selectivity[36-38]. Lithographic patterns and chemical patterns have also been used in directed self-assembly of supramolecules to achieve long-range order and finely tune the nanostructure[39, 40].

While there have been large body of studies in achieving structural and, to some extent, functional control in supramolecules, there is still a significant gap in understanding the kinetic processes that result in these experimental observations. Despite the complexity and large parameter space, there are rather limited studies on the kinetic pathway of assembly and systematic investigation into what role each of the components plays during the assembly process. In supramolecular thin films, macroscopic alignment of microdomains and in some cases, morphologies can be independently tailored regardless of interfacial interaction and film thickness by varying solvent condition[36, 38]. By varying the solvent fraction during annealing process, the assembly process was optimized for rapid ordering in the timescale of tens of seconds for scalable manufacturing[41]. Manipulating kinetic pathway of different assembly processes has also been applied to control the morphology in

nanoparticle-containing supramolecular thin films to achieve a non-equilibrium morphology[42]. From these studies, it is clear that the kinetic pathway affects the final film morphology. There is a great need to systematically investigate the role of each of the components, and how those components interact and affect the overall phase diagram, various assembly processes, and ultimately, the resultant hierarchical assemblies in supramolecular thin films (Figure 1).

Here, it is shown that by systematically varying the small molecule loading as well as the solvent annealing condition, the effects of both components on the assembly process can be decoupled to gain control over the characteristic features on flat and patterned surfaces. There is a superposition effect between the small molecule loading and the solvent fraction to create ordered structures with long-range order. For all supramolecular system investigated, incommensurability between the pattern width and supramolecule periodicity did not cause the system to disorder, which was attributed to the presence of small molecule. Furthermore, the kinetic pathway, rather than the incommensurability seen in BCP, is key to understand the feature size and the degree of order in supramolecular thin films on patterned substrate.

2.2 Role of Small Molecule Loading and Solvent Annealing Condition on Flat Substrates

The supramolecule used here is polystyrene-block-poly(4-vinylpyridine) (pentadecylphenol)$_r$ (PS-*b*-P4VP(PDP)$_r$). The molar ratio of PDP to the 4VP monomer is defined as r. The kinetic and thermodynamic considerations of each

component will dictate the self-assembly process. Several of the components will affect the system at the same time and in a similar way, making it difficult to determine how each component contributes to the self-assembly process. Figure 1 shows the general considerations of each of the main components of the supramolecular system, the BCP, the small molecule, and the solvent.

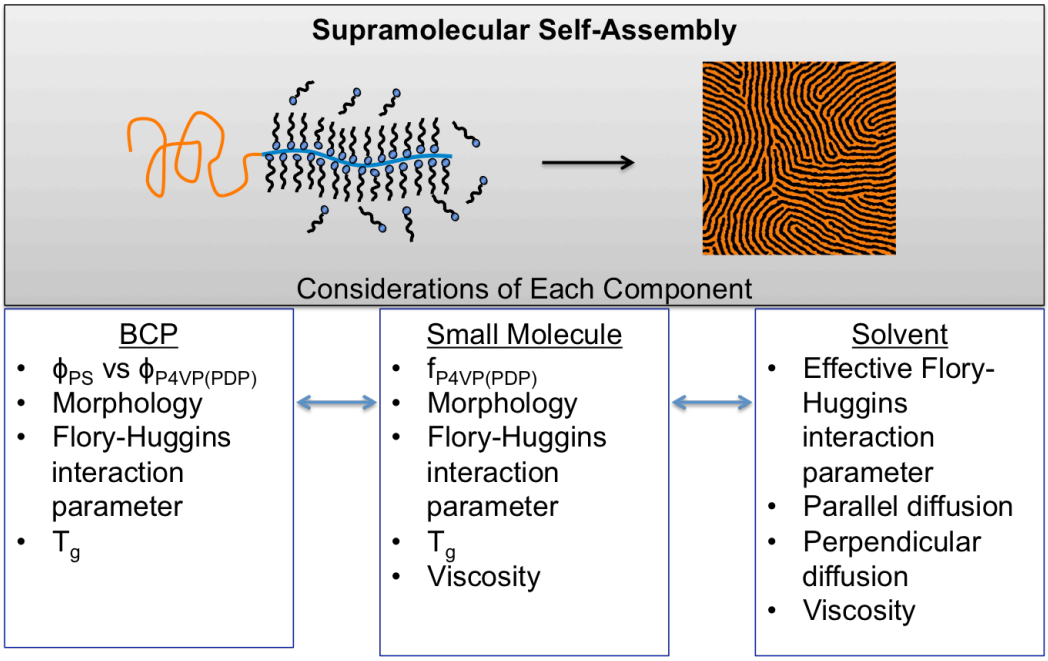

Figure 1: Scheme depicting supramolecular thin film assembly. The BCP, small molecule, and solvent all affect the thermodynamics and kinetics of the self-assembly process, often in similar ways. Each component will interact with the others to determine the final film structure, making it difficult to exactly know the effect of each component.

The BCP itself will affect the predicted morphology based on the relative volume fraction of the PS block and the P4VP(PDP) block as well as the Flory-Huggins interaction parameter (χ) between the two blocks. The MW and composition of the BCP will determine the glass transition temperature (T_g), which determines the mobility and viscosity of the system. The small molecule loading will affect several of the same factors. It can be used to tune the volume fraction of the P4VP(PDP) block and therefore morphology. Adding an additional component creates more interaction parameters and can also change the effective χ between PS and P4VP. Again, the T_g and viscosity will change, leading to changes in the diffusion rates and kinetic pathway during the assembly process. Solvent has similar considerations. The addition of solvent will change χ, T_g, and the system viscosity. These in turn all affect the diffusion of the supramolecule. During ordering, there are two important types of diffusion: parallel diffusion, which happens along PS/P4VP(PDP) interface, and perpendicular (interdomain) diffusion, which happens across the PS/P4VP(PDP) interface[43, 44]. Solvent annealing will lower the energy barrier to both types of diffusion, but is particularly important for perpendicular diffusion[41, 45]. As such, the PDP loading and solvent annealing condition were systematically investigated. In bulk, the chosen supramolecules form hexagonally-packed PS cylinders embedded in a P4VP(PDP) matrix with a periodicity of ~31 nm. Films were monitored *in situ* to precisely control the solvent fraction (f_s) in the films during the annealing process. The f_s reported is the final solvent fraction before the annealing process is terminated.

The PDP loading was varied between r=1 to r=2 to investigate how introducing free small molecule into the system affected the morphology and long-range order of the assembly (Figure 2). When there a stoichiometric ratio of PDP (r=1), no apparent ordered structure is found at any f_s (Figure 2a). The predicted morphology of a bulk system with r=1 is lamellae. In the AFM phase images, the light regions correspond to the PS domain and the dark regions correspond to the P4VP(PDP) domain. All films for r=1 show a light matrix with darker defects oriented randomly. They are disordered. No clear morphology develops as the amount of solvent increases, suggesting the system does not have sufficient time or mobility to form an ordered structure. This is the case for r=1.2 as well.

When the PDP loading is increased to r =1.5, the supramolecular thin films display order (Figure 2b). Based on the volume fraction of the comb block, the predicted morphology is on the border between lamellae and hexagonally packed cylinders. At f_s=0.1, the morphology is not clear, but when f_s=0.2, short PS cylinders are formed. Additional solvent annealing leads to longer PS cylinders, as expected due to increased mobility as solvent vapor is added to the system. At high solvent fractions ($f_s \geq 0.4$), however, the system is disordered. Solvent annealing yields the expected morphology, but only in a narrow window. When the PDP loading is increased to r=2 (Figure 2c), the film behaves as similarly to that seen at r=1.5. At very short solvent annealing times, short PS cylinders form. As more solvent is added, the grain size of the PS cylinders grows. Free PDP facilitates the formation of long-range structures, but solvent annealing is necessary to reach films with large grain sizes.

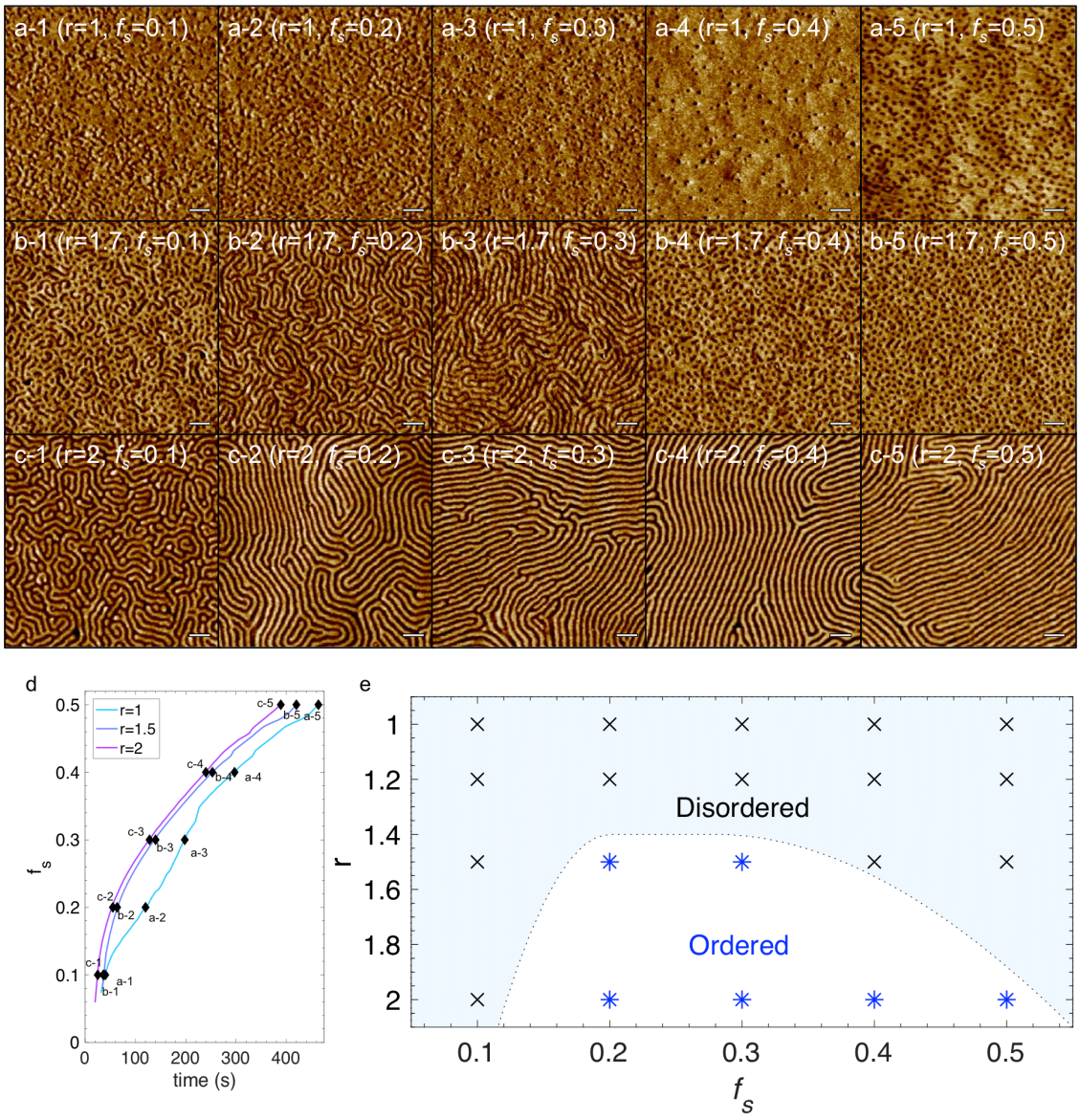

Figure 2: (a-c) AFM phase images corresponding points marked on f_s profiles in (d) at f_s=0.1, 0.2, 0.3, 0.4, and 0.5 for (a) r=1, (b) r=1.5, and (c) r=2. (d) The swelling profile of f_s versus annealing time for ~60 nm supramolecular thin films with r=1, 1.5, and 2. (e) Phase diagram of ordered and disordered structures as dependent on f_s and PDP ratio. Scale bar =100 nm.

Figure 2e shows a phase diagram for ordered versus disordered structures as a function of PDP loading, r, and solvent fraction. The shape of the order/disorder phase boundary shows the superposition of the effect of the solvent fraction and the small molecule. At low PDP loading, the system will not form an ordered structure under solvent annealing. With sufficient PDP loading, ordered structures are possible, but solvent annealing is necessary. The long-range order and window over which there is an ordered structure of the system depends on both the solvent annealing condition as well as the small molecule loading.

The superposition between the effect of solvent fraction and PDP stoichiometry on forming ordered structures is more apparent when considering a smaller range of r, where the films all give the same morphology. Here, we pick r=1.7, 2, 2.2, and 2.4, which all give hexagonally packed PS cylinders in a P4VP(PDP) matrix, based on analysis of the GISAXS patterns[46]. Figure 3 shows AFM phase images and GISAXS profiles for the given small molecule loading as the films are annealed to f_s between 0 and 0.5. Both solvent annealing and small molecule are important to determining the characteristic features of the films.

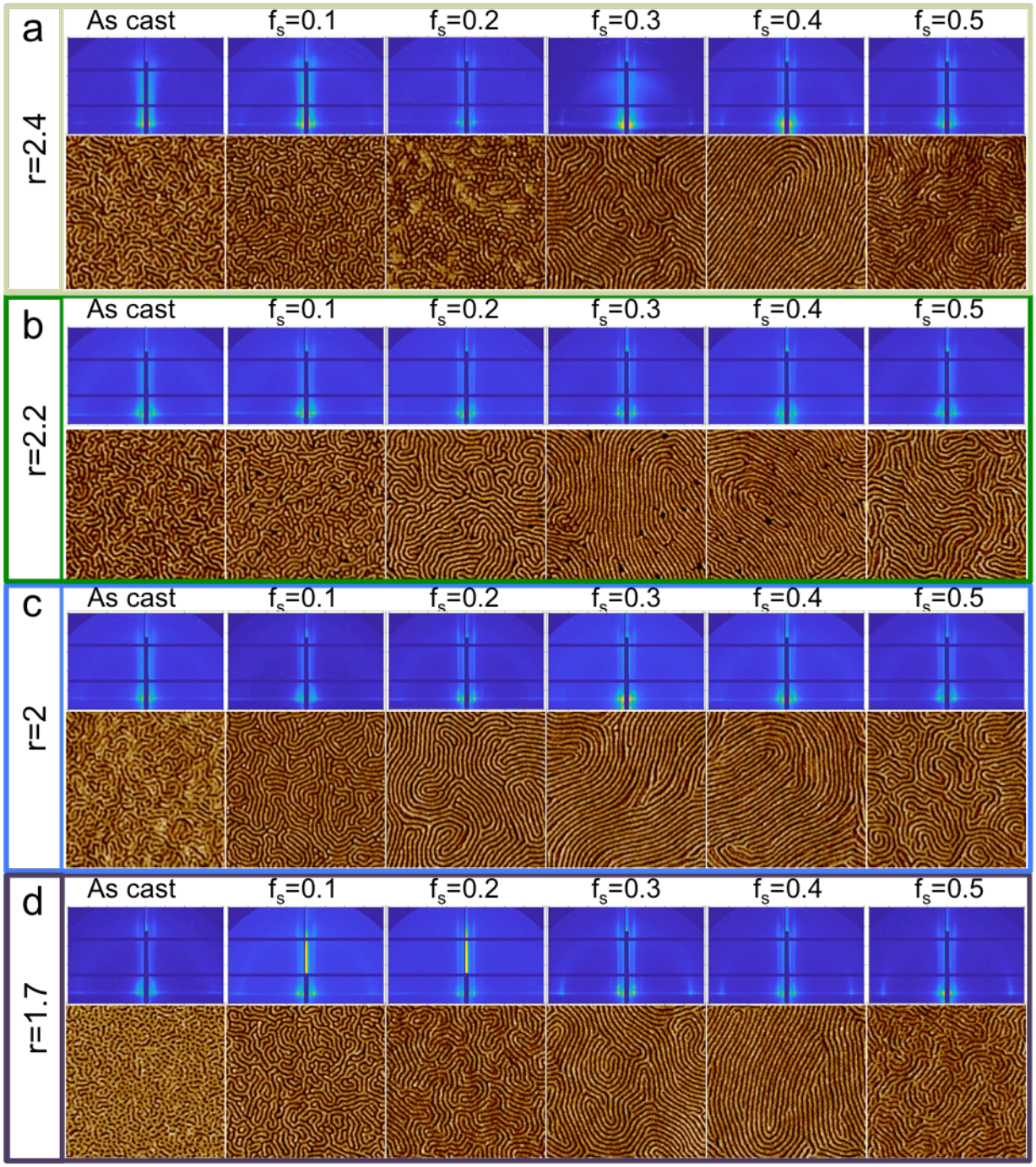

Figure 3: Supramolecular thin films at different fs for (a) r=2.4, (b) r=2.2, (c) r=2, and (d) r=1.7. All AFM phase images are 1 μm x 1 μm. The scale for the GISAXS patterns are from q_z=0-0.25Å^{-1} and q_y=-0.2-0.2 Å^{-1} with tick marks every 0.05 Å^{-1} in both q_z and q_y.

For all small molecule loading between r=1.7-2.4, solvent annealing to different f_s produces the same general effect on grain size. The trend is exemplified best by r=1.7 (Figure 3d). As-cast, the film does not show any clear ordering. Once solvent is introduced to the system, it begins to form an ordered structure, albeit one with a small grain size. Increasing f_s leads to longer grain sizes, until at f_s=0.4 the maximum grain size is reached. Once the film is annealed past this point, the grain size begins to decrease. Figure 4a shows the exact changes in grain size for all r. The grain size was obtained by using the Scherrer equation on the fitted full width half maximum of linecuts of the first order peak from the GISAXS data.

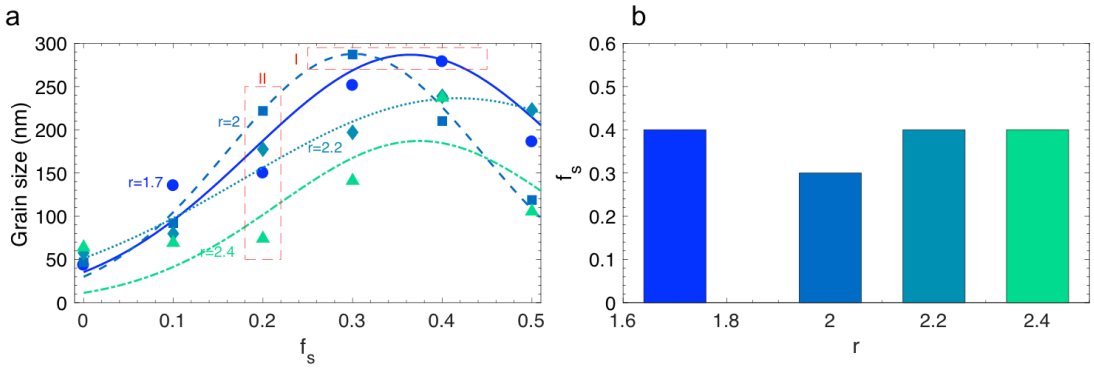

Figure 4: (a) Grain size of supramolecular thin films at different solvent annealing conditions and different small molecule ratios. (b) Solvent fraction that gives maximum grain size for each small molecule stoichiometry

Once again, the superposition of the effect of PDP and the solvent fraction can be seen. Region I highlights two separate films that have the same approximate grain size, but were prepared using different conditions. The first film was annealed

to a smaller solvent fraction and a greater PDP ratio than the second film. The second film has less PDP and so must be annealed to a higher solvent fraction to reach the same grain size. There is a tradeoff between the amount of solvent necessary and the PDP ratio needed to achieve the largest grain size. This observation is consistent with the phase diagram in Figure 2e. It should be noted that once the PDP loading is r>2, films need to be annealed to higher solvent fractions to reach their maximum grain sizes and that the maximum grain size is shorter (Figure 4b). The roll of PDP in the assembly is complex. It assists in mobility and drives long-range order, as demonstrated in Figure 2. However, excess free PDP seems to hinder long-range order of the supramolecule. Free PDP may decrease the thermodynamic driving force for separation even if it aids in the mobility of the system by lowering T_g, viscosity, and barriers for interdomain diffusion, resulting in a need for a balance between the amount of PDP and the solvent annealing condition.

Region II of Figure 4b shows how modulating the PDP ratio can be used to select a desired feature size. For a given solvent fraction, the grain size can vary by as much as 150 nm simply by selecting the PDP stoichiometry. Solvent annealing induces mobility in the system by lowering T_g and χ. But, the amount of PDP affects T_g and χ as well and can long-range ordering by mediating interactions or hurt it if the interactions are lowered enough to no longer retain the thermodynamic driving force for separation.

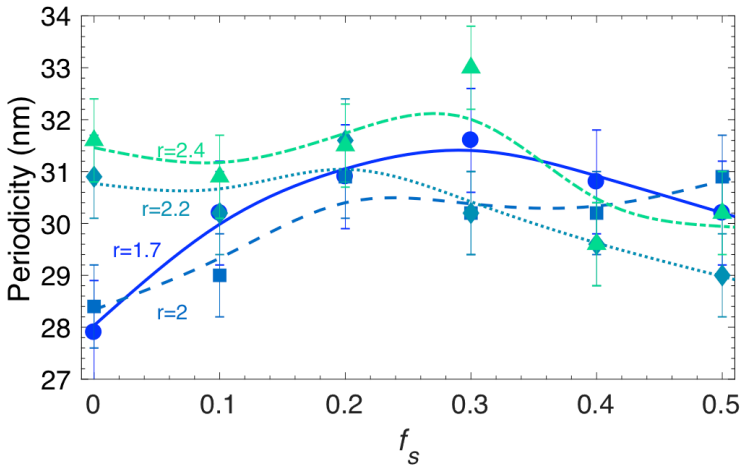

Figure 5: Periodicity of supramolecular thin films at different solvent annealing conditions and different PDP ratios.

The effect of the PDP and solvent annealing condition on the periodicity of each film is not as clear as the effect on the grain size. The periodicity for each condition is given in Figure 5. The changes in periodicity are modest as a function of both solvent annealing condition and PDP ratio—only a range of around 4 or 5 nm—and do not display a clear trend. It may be expected that increasing the amount of free PDP should swell the P4VP domain. Previous work has shown that increasing PDP loading can swell one domain and change morphology[2]. The PDP does seem to swell the P4VP domain for as-cast films: there is a difference between the lower PDP ratios (r=1.7 and 2) and the higher ratios (r=2.2 and 2.4) of 3-4 nm. However, once the system is annealed, this difference in periodicity disappears. The lack of change in periodicity suggests that the PDP does not simply swell one domain. Once solvent is introduced to the system, the free PDP gains mobility and likely rearranges throughout the polymer. It is known that PDP can become soluble in the PS domain

at high temperature, so at high solvent fractions, it is reasonable to speculate that there is PDP in both microdomains of the supramolecules.

2.3 Role of Small Molecule Loading and Solvent Annealing Condition on Patterned Substrates

The tradeoff between the amount of PDP and the solvent annealing condition for creating long rang order is apparent when these films are assembled on patterned substrates. Using a patterned substrate that is ~180 nm in width and ~50 nm deep, the supramolecule aligns with the underlying pattern (Figure 6). The degree of alignment with the underlying pattern, however, is once again a function of its condition, i.e. the amount of solvent and PDP ratio. The order parameter (OP) was calculated for each film to quantify the degree of alignment with the substrate. A perfectly aligned film will have OP=1 and an isotropic film will have OP=0. Qualitatively, the OP of films on a patterned substrate follows the same trend as the grain size for films on flat substrates at all r. Using r=1.7 as an example (Figure 6a-c), the trend is as follows: below f_s=0.3, the alignment with the underlying substrate is poor. Once at or above f_s=0.3, there is good alignment with the pattern. At f_s=0.4, the OP is the highest and there are few defect on the film. Past this solvent fraction, the alignment with the substrate decreases and the number of defects increases, particularly at the trench/mesa interface. The f_s at which the OP is the highest is dependent on r, just like the f_s at which the grain size was largest depended on r for assembly on flat substrates. The exact OP for all r and f_s is shown in Figure 7a.

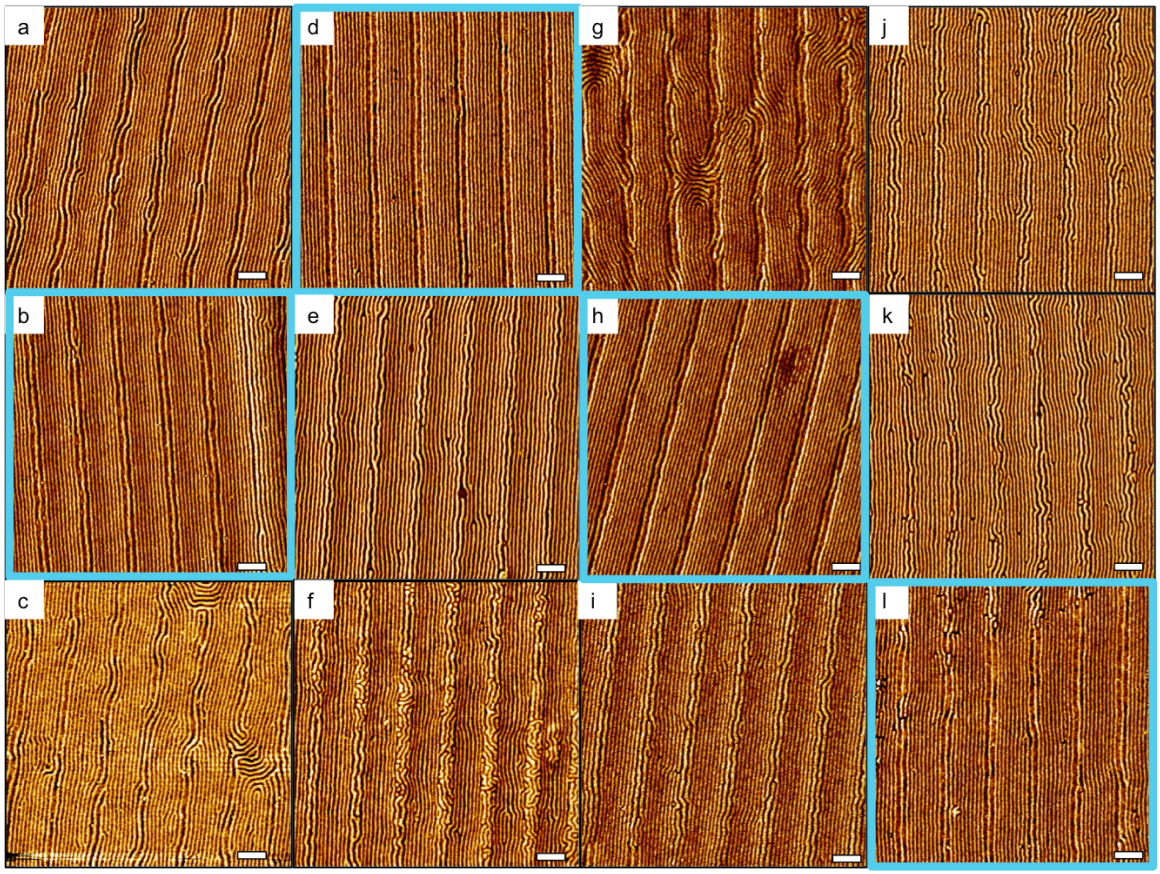

Figure 6: Supramolecule thin films with initial thickness of 60 nm on a 180 nm trench pattern with different PDP loading and solvent fraction. (a) r=1.7, f_s=0.3, (b) r=1.7, f_s=0.4, (c) r=1.7, f_s=0.5, (d) r=2, f_s=0.3, (e) r=2, f_s=0.4, (f) r=2, f_s=0.5, (g) r=2.2, f_s=0.3, (h) r=2.2, f_s=0.4, (i) r=2.2, f_s=0.5, (j) r=2.4, f_s=0.3, (k) r=2.4, f_s=0.4, (l) r=2.4, f_s=0.5. Scale bar = 100 nm.

The periodicity of the supramolecule in the trench does not depend on the ratio of PDP and is smaller than the periodicity of the supramolecule on a flat substrate (Figure 7b). The periodicity for all PDP ratios studied (r=1.7-2.4) is the same, ~26.5 nm. This lack of change in periodicity is consistent with the lack of

change in periodicity on flat substrates. It should be noted, however, that the trench periodicity is smaller by 3-4 nm as compared to the flat substrate periodicity. The presence of PDP does not swell the periodicity, but does affect the long-range order and defect density of the assembly in the patterned substrate.

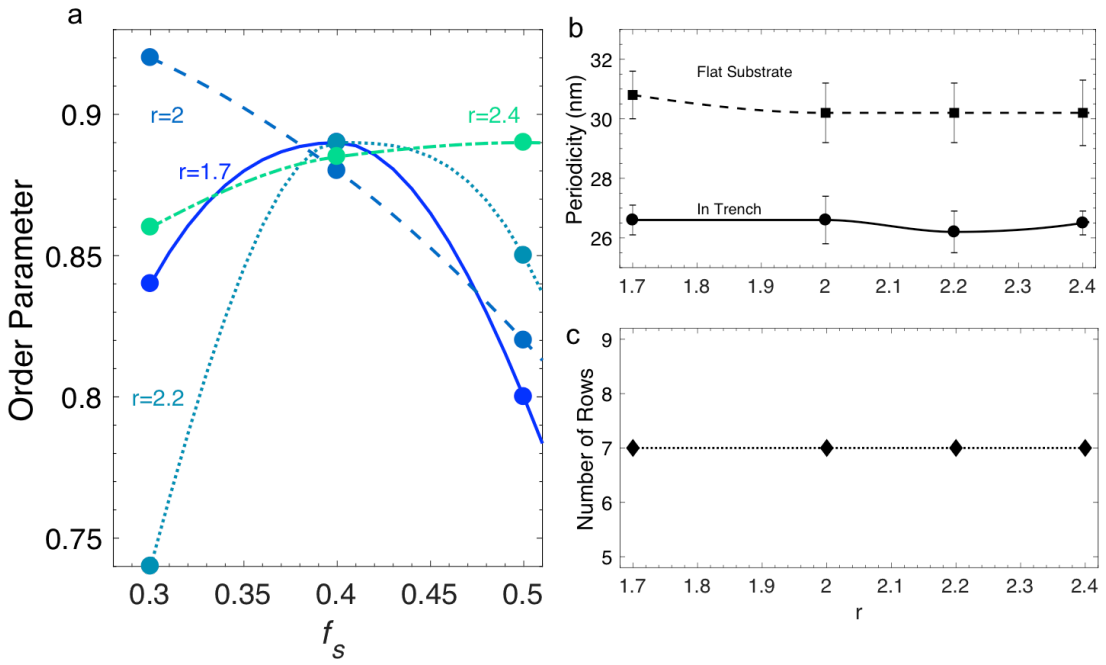

Figure 7: (a) Order parameter of films in Figure 6 as a function of solvent fraction and PDP ratio (b) Periodicity of supramolecule on lithographic substrate and flat substrate as a function of small molecule ratio, r. Periodicity of the flat substrate is given at the solvent fraction that matches the best ordering in the trench pattern (c) Number of rows of PS cylinders in the trench as a function of small molecule ratio, r.

The decrease in periodicity from the flat substrate to the patterned substrate is about 10%. Compression or expansion of periodicity has been seen in traditional

BCP films on patterned substrates in order for periodicity of the polymer to be commensurate with the width of the trench[47, 48]. However, the compression of the polymer chain leads to an entropy penalty. If the polymer must compress too much for the width of the trench to be an integer multiple of the periodicity of the confined microdomain, the polymer will not align with the trench pattern due to the loss in entropy. The BCP will rearrange so the number of rows in the trench minimizes this loss of entropy and retains as close to the equilibrium periodicity as possible.[49] Here, regardless of small molecule loading, there are 7 rows of PS cylinders in the trench (Figure 7c). If the supramolecule were to retain the approximate flat substrate periodicity in the trench pattern, there should only be 6 rows of PS cylinders since the trench width is ~180 nm and the flat substrate periodicity is ~31 nm. The assembly in the trench does not follow the basic rules of commensurability between the trench width and the supramolecule periodicity, indicating that the supramolecule can rearrange. The final features are likely dependent on the kinetic pathway taken rather than energetic considerations of incommensurability. Thus, the incommensurability effect is quite small when assembling the supramolecule in the trench pattern. It can also be observed that there are two separate periodicities, a trench periodicity and a much larger mesa periodicity. It is likely that the small molecule self-adjusts during the annealing process to produce this pathway-dependent phenomenon. However, further study is needed to understand this observation.

Alignment of the supramolecule with a patterned substrate is not limited to linear trenches. Rather, the supramolecule can assemble in concentric circle

patterns as well (Figure 8). These patterns are fabricated using electron beam lithography. There are three rings etched into the silicon, all with a width of ~165 nm but different radii.

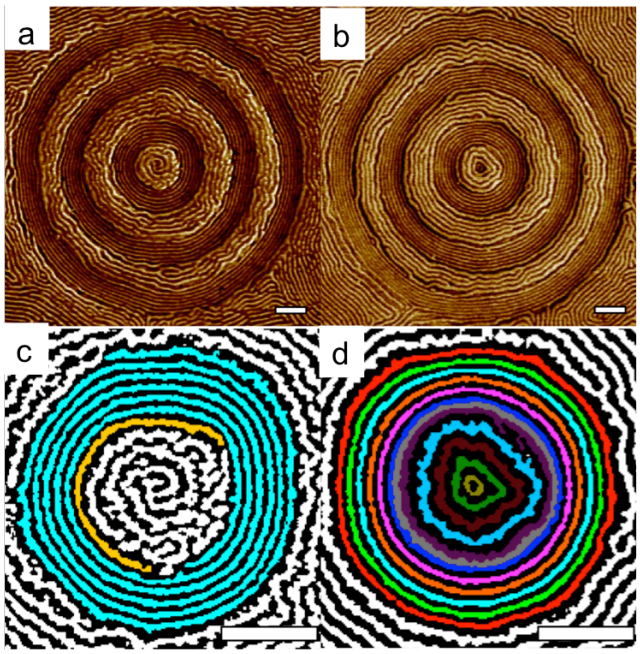

Figure 8: ~60 nm supramolecule thin films on a circular trench pattern with width ~200 nm with (a) r=2 and (b) r=2.2. Dark regions are the trench patterns. The colored regions in (c) and (d) are close ups of the inner circles of (a) and (b) respectively. The colors were added to show one continuous PS cylinder in the trench pattern.

Depending on the conditions used to prepare the films, the supramolecule can align with the rings by forming a spiral (Figure 8a) or a series of concentric rings (Figure 8b). Figures 8c and d show close ups of the innermost ring of 8a and 8b, respectively, so that the features of the PS cylinders can be easily seen. The

periodicity in the trench pattern has once again decreased to ~28 nm in the trench. As with the line patterns, the supramolecule will take a pathway that is beneficial to assembly and adjust the periodicity to conform to a pattern. Here, Figure 8a is made with supramolecule at r=2 and Figure 8b is made with r=2.2. The PDP loading can affect the resultant pattern, although more research is needed to understand why exactly the pattern would result in a spiral or concentric circles. Thus, it is hypothesized that the self-adjusting nature of the supramolecule will extend to any geometric pattern.

2.4 Discussion

The results presented above confirmed that both PDP and solvent annealing are key factors for the self-assembly of supramolecular thin films. Together, they affect the feature size, grain size and degree of ordering on flat and patterned substrates, and there is a superposition relationship between the two. The observed film features depend on the kinetic pathway that can be moderated by either the solvent annealing condition or the small molecule loading. On flat substrates, the PDP and the solvent annealing condition can be interchanged to generate a desired grain size. This observation is contributed to a balance of the thermodynamic driving force for separation and the kinetic pathway. Both solvent and the small molecule can act as a placticizer in the system[14]. As such, with the introduction of either, the χ_{eff} will begin to decrease, T_g will change following the Fox equation, and the viscosity of the system will lessen, giving the system sufficient mobility to form long range order[50, 51]. To create an ordered structure, two diffusion coefficients determine the mobility of the system, parallel diffusion (diffusion along the domain

interface) and perpendicular diffusion (diffusion across domain interface)[43, 44]. Parallel diffusion has a lower energetic penalty associated with it as compared to perpendicular diffusion due to interdomain crossing[45]. This interdomain crossing can be very energetically costly if χ is high and so has a high activation energy. Without interdomain crossing, though, the system will lack long-range order. As solvent is added to the system, χ_{eff} decreases and thus perpendicular diffusion becomes easier. This lowering of the activation energy is key for both mobility of the system and defect annihilation. Adding PDP will decrease the T_g and will also lower χ_{eff}. However, adding PDP alone is not enough to decrease the T_g below room temperature. Solvent is needed as well so that the system has enough mobility to form long-range ordered structures. Here, the cooperation between the two factors is key for the system to order. Because they affect the same parameters in the system, it makes sense that either PDP or increased solvent fraction will improve long-range order. However, it was seen in both the case of PDP and solvent that there is a narrow window over which increasing them increases the grain size. Once pass the threshold, the addition of more solvent or increasing the PDP loading begins to reduce the grain size and may even cause the system. As the system gains mobility, thermodynamic driving force for separation, captured by χ_{eff}, is important in determining whether the system will order.

The importance of the kinetic pathway on the final structure as well as the cooperative effect between the PDP and solvent is apparent in examining the supramolecule thin film assembly on a patterned substrate. There has been a lot of research into the assembly of BCPs on patterned substrates. One of the fundamental

rules to come out of the confinement of BCPs on patterned substrates is the rule of commensurability[47, 48, 52, 53]. That is, for a BCP to order in a trench pattern, the width of the trench must be an integer multiple of the BCP periodicity. The polymer can adjust somewhat from its equilibrium periodicity, L_o, but there is a loss of entropy associated with either the stretching or compression of the periodicity to so that is commensurate trench width[49]. If the polymer must stretch or compress too much to fit in the trench, it will not order. In this paper, the width of the linear trench is 180 nm, which is commensurate with the equilibrium periodicity of the supramolecule periodicity, ~30 nm, to form 6 rows of PS cylinders in the trench. While the supramolecule may have to stretch or compress by ~1 nm at some solvent annealing conditions, this only represents a deviation from the equilibrium periodicity of ~3%. However, here, regardless of PDP loading, there are 7 PS cylinders in the trench and the periodicity is uniformly 26.5 nm. While this represents only a 10% deviation from the equilibrium periodicity on a flat substrate, there is no reason for there to be any deviation. If the supramolecule were to operate under the same rules as BCPs, the fact that there are 7 rows of compressed polymer rather than 6 rows of uncompressed polymer would indicate a significant loss of entropy and be energetically unfavorable. Thus, the polymer does not follow the thermodynamically predicted structure, so it must be kinetically determined. At the beginning of the self-assembly process (Figure 9a), the film is disordered. We hypothesize that as the process continues (Figure 9b), seven rows of PS cylinders are templated into the trench. After those cylinders are templated, those cylinders grow parallel to the trench (Figure 9c). To reach the equilibrium periodicity in the

trench (Figure 9d), the system would have to go through a disordered state, which has a high energetic cost due to increased interfacial area and excessive interdomain crossing. Thus, the final structure observed here is a kinetically determined state.

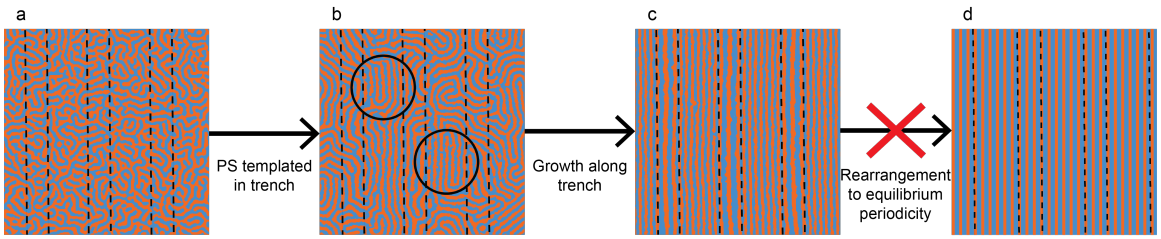

Figure 9: Scheme of the kinetic pathway resulting in smaller periodicity in trench during the assembly process, going from (a) a disordered state to (b) templating of the number of PS rows in the trench to (c) an ordered structure with a smaller periodicity in the trench. (d) The equilibrium periodicity is not accessible due to the high energetic penalty required to reach it.

The fact that this same phenomenon—shrinking of the periodicity within the trench—is observed in circular patterns as well suggests how important the kinetic pathway is. This pathway is possible because of the presence of the small molecule. The small molecule is able to redistribute throughout the film and adjust so that rather than simply forming a disordered state, as might be predicted from BCP studies, the supramolecule can self-adjust and still assemble with a smaller periodicity in the trench. Unfortunately, imaging the small molecule directly is not possible so it is hard to say precisely what it is doing, but likely it is a combination of migrating into the PS and onto the mesa portion of the trench. The solvent annealing condition and small molecule loading determine how well-ordered the assembly on

the trench is and also set the kinetic pathway to ordering. Additionally, the fact that the periodicity does not decrease on flat substrates as a function of either solvent annealing condition or PDP loading indicates that the confinement itself is the cause of the decreased periodicity.

2.5 Conclusions

In summary, the cooperative nature between the solvent annealing condition and the amount of free small molecule in producing ordered morphologies and tuning the grain size of supramolecular thin films was shown. There is a superposition between the conditions to create an ordered film and its final features. On both linear and circular patterned substrates, these two factors also affect the alignment and order parameter of the system. The assembly on patterned substrates is not driven by incommensurability as is commonly seen in BCP thin films, but rather by the kinetic pathway. The solvent annealing condition and small molecule loading affect the kinetic pathway taken during assembly and so can be used to control the features of these thin films. The understanding of this superposition and cooperation opens the door to creating supramolecular films with tunable features on both flat and patterned substrates.

2.5 Methods

Materials

BCP, polystyrene-block-poly(4-vinyl pyridine) (PS(19 000)-*b*-P4VP(5200)) (PDI = 1.09) was purchased from Polymer Source, Inc. 3-*n*-Pentadecylphenol (95%) was

purchased from Acros. Chloroform was purchased from Fisher. All chemicals were used as received.

Sample Preparation

Supramolecular solutions were prepared by dissolving the polymer and the small molecule in chloroform and then stirring for 24 hours. Thin films were prepared by spin-coating the mixed solutions onto silicon wafers at 3000 rpm. Sample thicknesses were measured using a Filmetrics F20 interferometer. For solvent annealing, samples were annealed using 300 μL of $CHCl_3$ injected inside a 250 mL top-capped jar at 22.5 °C. Once the film thickness of the nanocomposite thin film reached desired thickness, the jar was opened and the $CHCl_3$ vapor inside the jar was allowed to freely evaporate. Solvent fraction is the volume fraction present in the swollen film during annealing, calculated as $f_s=\frac{t_f-t_i}{t_f}$ where t_f is the final film thickness and t_i is the initial film thickness. The solvent annealing process was stopped at a certain f_s.

Fabrication of Patterned Substrates

The rectangular trenches were fabricated using interference lithography and have average width and height around 180 and 50 nm, respectively. Circular trenches were patterned using electron beam lithography and have a width and height around 165 nm and 50 nm, respectively.

Atomic Force Microscopy (AFM)

AFM was performed on a Bruker Dimension Edge. The spring constant of the cantilever was 5-10 N/m with a resonant frequency in the range of 90-210 kHz. The

set point for the auto tune was ~6.0V. The set point amplitude was 80-90% of the free vibration value.

Image Analysis

Image analysis was performed using ImageJ. AFM phase images of linear trenches were first thresholded to eliminate noise. The images were then skeletonized so that each PS domain in the supramolecule was traced. At each pixel in the skeletonized image, a line of best fit was determined by drawing a line through the adjacent points in a 5-pixel by 5-pixel area. The angle that line made with the x-axis, from -90˚ to 90˚ was recorded as the tangent line to the PS cylinders at a given pixel. This distribution of angles was then tabulated and used to calculate the Herman orientational parameter, $S=2\langle\cos^2\theta\rangle-1$[54, 55]. AFM phase images of circular trenches were thresholded to eliminate noise and converted to binary images.

Grazing Small Angle X-ray Scattering (GISAXS)

GISAXS experimental measurements were made at beamline 7.3.3 at the ALS in Lawrence Berkeley National Laboratory and at beamline 8-ID-E the APS in Argonne National Laboratory. X-ray wavelengths of 1.687 and 1.240 Å were used at APS, and ALS, respectively. The scattering intensity distribution was captured by a Pilatus 1 M detector at ALS and APS at an incident angle of 0.13˚. The intensities (I) are plotted with respect to q, where $q = (4\pi/\lambda)\sin(\theta/2)$, λ is the wavelength of the incident X-ray beam, and θ is the scattering angle.

Chapter 3
Directed Self-Assembly on Geometrically Patterned Substrates

3.1 Introduction

Block copolymer (BCP)-based supramolecules have shown great potential to create hierarchically ordered nanostructured thin films[1, 2]. These supramolecules are formed from a small molecule non-covalently bonded to one of the blocks of a BCP[3, 4]. By tuning the small molecule, processing conditions, incorporation of nanoparticles, and kinetic pathway, great structural control has been achieved to produce thin films with tunable periodicity, grain size, and morphology[5-15]. Directed self-assembly (DSA) of BCPs provides another level of structural control[16-23]. DSA has mainly focused on aligning BCPs and supramolecules with linear patterns[24-29].

While DSA has been widely adopted, it is fundamentally constrained by the need for commensurability: the width of the guiding feature must be approximately an integer multiple of the equilibrium periodicity (L_o) of the BCP[30-34]. Incommensurability opens a new path toward assemblies beyond the common BCP morphologies, but it requires careful matching between the pattern and BCP and control of the preferential wetting conditions at the film/substrate interface to modulate incommensurability[35, 36]. These constraints make it difficult to generate controllable heterogeneous features without compromising the long-range order[37, 38].

For many devices and applications, such as use in microelectronics, DSA must be coupled with patterns of arbitrary geometry[39]. Circular patterns are of particular interest due to their potential use in sensors, memory storage, lasers, transistors, and more[40, 41]. Due to their constantly changing radius of curvature, these patterns have additional constraints. However, it has been shown that a BCP can align with a

circle of different radius of curvature, ranging from 12 nm to 1000 nm in a single pattern, by chemically patterning commensurate stripes[42]. Concentric rings with tunable dimensions can be formed from commensurate circular patterns. In these, much finer rings are formed from a larger, rougher pattern. The rings can then be selectively etched and transferred to the pattern[41]. Chiral spiral structures can also be formed with controllably in ring patterns[40]. The assembly of a BCP in circular patterns has been successful, but is still primarily driven by commensurability.

Here, concentric circles were used as the guiding patterns for DSA of supramolecular thin films. The assembly on circular patterns of different widths was shown to be dependent on the pathway taken during assembly rather than determined by the commensurability between the supramolecular periodicity and the trench pattern width. The supramolecule is able to adjust during the self-assembly process to align with the underlying pattern regardless of trench width, degree of curvature, and molecular weight of the supramolecule. This work represents a significant departure from traditional DSA because the final film features do not depend on commensurability, but rather the kinetic pathway that is unique in a multicomponent, self-adjusting system.

3.2. Directed Self-Assembly of Supramolecules Without Nanoparticles

The supramolecule used is polystyrene-poly(4-vinlypyradine) (pentadecylphenol)$_r$ (PS-P4VP(PDP)$_r$) where r is the ratio of small molecule PDP to 4VP monomer. The supramolecule was assembled on a concentric ring lithographic pattern (Figure 1) with the features of the rings systematically varied to understand how confinement

affects the assembly process. The pattern features are shown in Table 1, where the trench width (W_t), mesa width (W_m), and inner circle diameter (C_d) were varied.

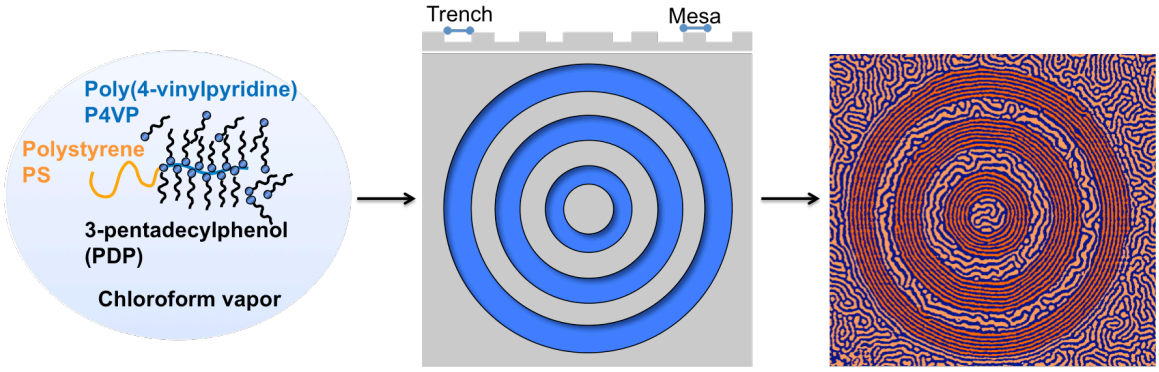

Figure 1: Schematic of DSA process. The supramolecule (left) is cast from solution onto the trench pattern (middle), solvent annealed, and aligns with the underlying pattern (right). Trench pattern shows top down as well as side-on view.

Table 1: Feature sizes of the lithographic patterns

	W_t (nm)	W_m (nm)	C_d (nm)
P1510	150	100	300
P1515	150	150	300
P1520	150	200	300
P1110	110	100	300
P2015	200	150	300
P15i	150	150	150

Circle patterns of different width were used to examine whether commensurability is needed to guide the supramolecule assembly. The equilibrium periodicity, L_o, of the supramolecule used here is ~31 nm. P1110, P1515, and P2015 were used. For these trench widths, if commensurability drives the alignment, it is

expected that the supramolecule will not align with P1110 and P2015. However, the supramolecule aligns well all three patterns (Figure 2). In order to see how well the underlying pattern aligns with the trench, the AFM phase images were binarized and PS cylinders in the trench pattern were given a color. Each color represents one continuous PS cylinder. From these color maps, the degree of alignment of the supramolecule with the trench pattern can be more easily visualized. For P1110 (Figure 2a), the inner ring forms one continuous spiral, the middle rings forms a spiral with a few rings, and the outer circle forms a series of concentric circle. P1515 (Figure 2b) shows near perfect order: concentric rings with only a few defects are seen in all three circles. P2015 does not as clearly form either concentric circles or a continuous spiral (Figure 2c).

To quantify the order, $\sin(\theta)$ was calculated, where θ is the angle between the tangent line at each point on the pattern and the circle radius. If the PS cylinder is perfectly aligned with the underlying trench pattern, the angle formed between the tangent and radius should be 90˚, and $\sin(\theta)=1$. This was turned into a colormap to visualize alignment. A defect map was superimposed, showing the location of the terminal points (red circles) and junction points (black squares) in the PS domain (Figure 2d-f). The average alignment, $\langle\sin(\theta)\rangle$, in each region of the pattern—the inner (I), middle (M), and exterior (E) ring, the raised mesa (R), and the exterior of the pattern (E)—was also calculated (Figure 2g-i). As can be seen in the colormaps and defect maps, the alignment of the supramolecule with the rings on the mesa is not as good as in the trench. For P1110 (Figure 2d), there are several defects on the mesa, even if the alignment with the pattern is still quite high, with $\langle\sin(\theta)\rangle = 0.94$.

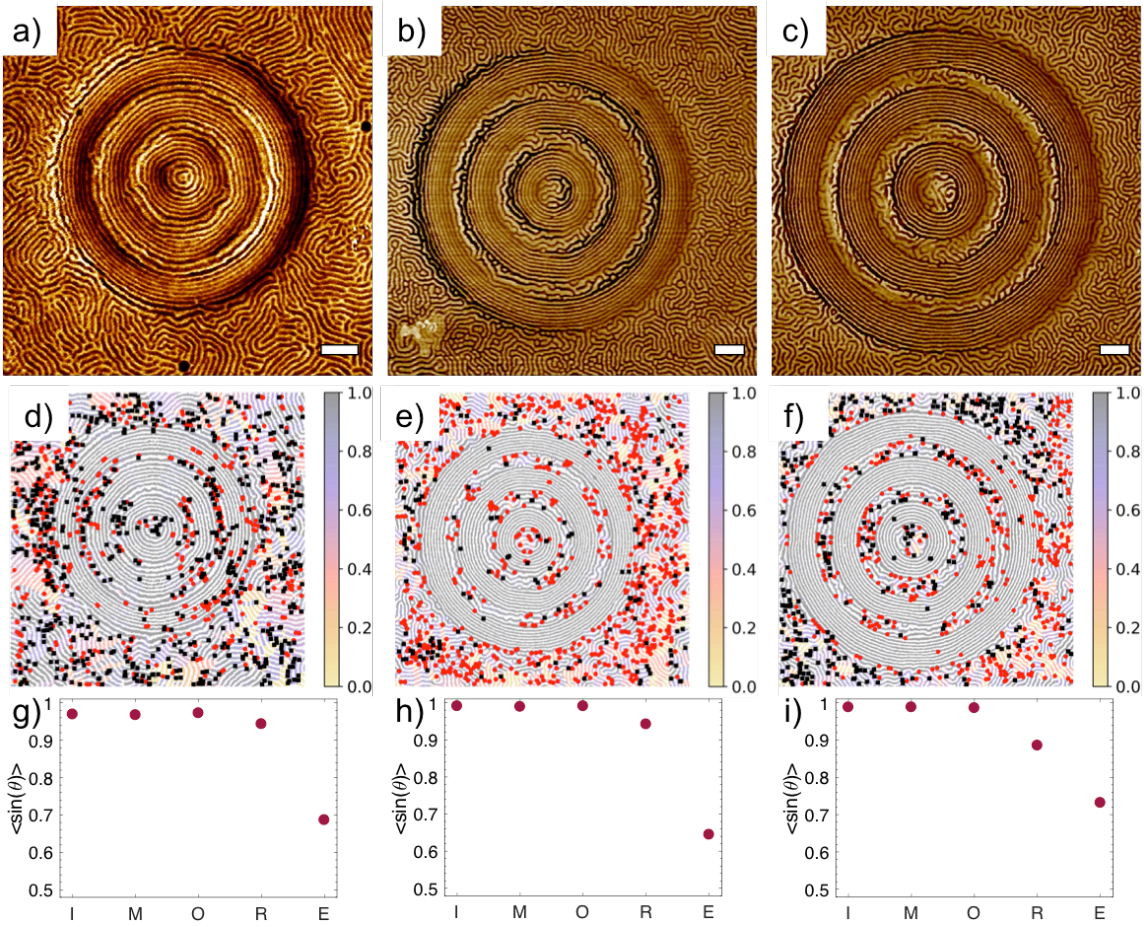

Figure 2: AFM phase image of supramolecule assembly on (a) P1110, (b) P1515, and (c) P2015. Color map with defect map in PS phase superimposed showing sin(θ) at each point for (d) P1110, (e) P1515, and (f) P2015. Junction defects are black squares and terminal points are red circles. Average alignment, <sin(θ)>, for each region of (g) P1110, (h) P1515, and (i) P2015. Regions are inner (I), middle (M), and outer (O) rings, raised mesa (R), and exterior of pattern (E). Scale bar=200 nm.

On the exterior of the pattern, there are many defects. The alignment with the pattern exists for 1-2 periodicity outside the pattern. Past that point, the pattern appears to be mainly isotropic. P1515 follows a similar pattern to P11100: defects

are concentrated on the mesa rather than in the trench, with the mesas retaining good alignment with the trench pattern. The exterior of the pattern has many defects, most of which are terminal points. The alignment once again extends 1-2 periodicities onto the exterior of the pattern before becoming isotropic. For an isotropic pattern, <sin(θ)> is expected to be ~0.5. However, this value will increase if the exterior is aligned for any distance away from the pattern, which is what happens here. For P2015, the alignment in the trench is excellent, but the mesa is not as well aligned, with <sin(θ)>=0.88. There are several defects in the trench, and even more on the exterior of the pattern. For these three patterns, the trench width does not significantly affect the order in the trench, which is quite high. The mesa ordering is somewhat affected by the trench spacing, but still mainly follows the pattern. The mesa does contain several defects, even for the highly aligned patterns, and the exterior of the pattern itself has many. The pattern can guide the trenches, but everywhere else, there are many defects.

The periodicity and number of rows of PS in each trench as a function of trench width is shown in Figure 3.For all patterns, the periodicity is the same, approximately 25 nm. This periodicity is smaller than L_o by 19%. This is a significant deviation from L_o, which is unexpected. Typically, a BCP will not align by DSA if the periodicity must deviate from L_o by more than 10% due to a significant loss in chain conformation entropy[28]. However, for this supramolecule, it is hypothesized that the system is able to self-adjust. A new periodicity is set early during the annealing process, and the small molecule is expelled to the mesa and exterior to accommodate this new feature size. The pathway of assembly is what sets the

characteristic feature size, not commensurability. Changing the trench width adjusts the number of rows, but not the fundamental periodicity.

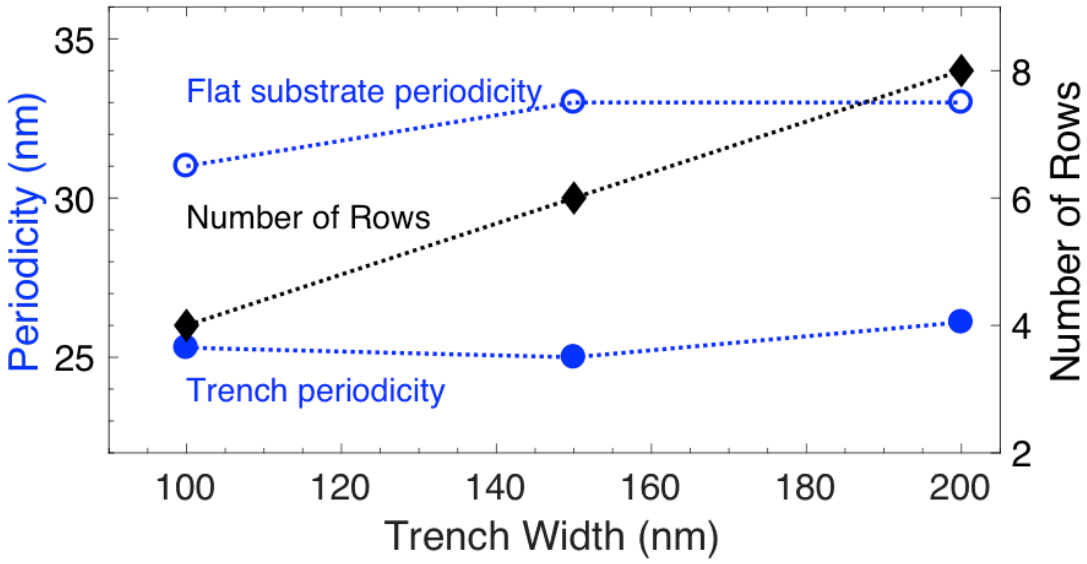

Figure 3: Periodicity of the supramolecule and number of rows of PS cylinders in the trench pattern as a function of trench width. The periodicity of the same supramolecule on a flat substrate is shown for comparison.

The trench width has a minimal effect on the alignment of the supramolecule in the trench. Next, the effect of the mesa width was examined. Two additional patterns with 150 nm trench widths were examined: P1510 and P1520, which have mesa widths of 100 nm and 200 nm, respectively (Figure 4 a, b). Once again, there is very good alignment of the supramolecule in the trench for these two patterns. On the mesa, as before, there is qualitatively good alignment with the trench, but with many defects, as can be seen in the alignment and defect map (Figure 4d, e). P1510 is an interesting case. It has the same mesa spacing as P1110, which had a

continuous spiral. However, even with the same ~3 periodicity spacing on the mesa, there is a clear separation between the alignment in the trench and the lesser alignment on the mesa. In the trench, the PS forms very long cylinders, with few if any junction points. On the mesa, however, there are much shorter PS cylinders, with very clear junctions. The aspect ratio of the PS cylinders has decreased considerably on the mesa, so that even if they are still well aligned, with $\langle \sin(\theta) \rangle = 0.96$, there is a clear distinction in how the supramolecule behaves on the mesa versus in the trench. These shorter aspect ratio PS cylinders are seen on the mesa for all patterns used, with the exception of P1110. The smaller mesa width is not enough to produce a continuous pattern, but rather, it seems to be a function of both mesa width and trench width. For the larger mesa pattern, P1520, the order on the mesa decreases somewhat as compared with P1510 and P1515, with $\langle \sin(\theta) \rangle = 0.92$. As the mesa width increases, the ordering on the mesa decreases.

The alignment in the trench does not appear to depend on the alignment in the mesa: for P1510, P1515, and P1520, $\langle \sin(\theta) \rangle$ is above 0.98 for all three rings. This suggests that the mechanism of self-assembly is such that alignment begins in the trench pattern. Changing the mesa spacing also affects the radius of curvature. Even if all three patterns have a trench spacing of 150 nm, the middle and outer rings will have a different radius of curvature. Again, this does not appear to affect the ability of the supramolecule to align with the underlying pattern.

To test the affect of the radius of curvature on the alignment of the supramolecule further, a pattern with smaller ring diameters was used, P15i. For

this pattern, the innermost mesa, a circle of silicon, was decreased from 300 nm for all previous patterns to 150 nm.

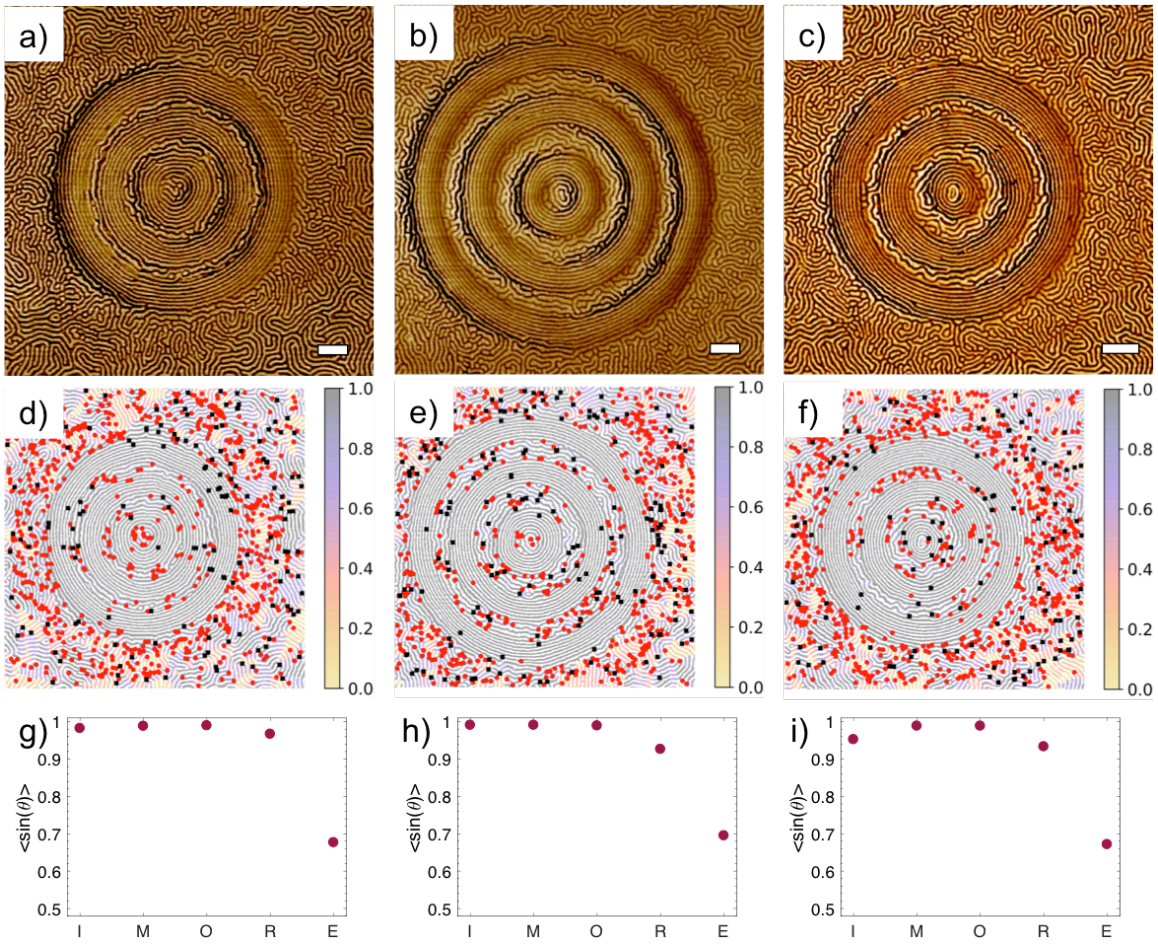

Figure 4: AFM phase image of supramolecule assembly on (a) P1510, (b) P1520, and (c) P15i Color map with defect map in PS phase superimposed showing sin(θ) at each point for (d) P1510, (e) P1520, and (f) P15i. Junction defects are black squares and terminal points are red circles. Average alignment, <sin(θ)>, for each region of (g) P1510, (h) P1520, and (i) P15i. Regions are inner (I), middle (M), and outer (O) rings, raised mesa (R), and exterior of pattern (E). Scale bar=200 nm.

This creates a much tighter radius of curvature for the inner ring of the pattern. The film assembled on P15i is shown in figure 4c. The supramolecule aligns well with the pattern, even with a much tighter degree of curvature. Here, the innermost mesa forms a series of concentric circles that extent to the first ring, which was not seen in other patterns. Interestingly, rather than having a PS dot at the center, there is a short PS line, forcing the circles to be more ellipsoidal. However, even with this change, the tight curvature radius still allows for good alignment. For all patterns examined here, with different trench width, mesa width, and radius of curvature, there is excellent alignment of the supramolecule in the trench with the pattern. The DSA of a supramolecule on ring patterns occurs successfully regardless of condition, but only in the trench pattern. On the mesa, it is still qualitatively aligned, but with more defects and a changing aspect ratio in the cylinders. This change in morphology occurs on the exterior of the pattern directly around the exterior ring. This suggests the pattern is self-adjusting: the small molecule is being expelled from the trench during the assembly process.

More careful analysis was done P1515, which had the best supramolecule alignment with the pattern (Figure 5). Each continuous PS domain was individually colored to examine the defects (Figure 5a). Here, they form a series of nearly perfect concentric circles, with only a few defects in the actual PS cylinders. The map showing defects in the PS domain only in Figure 5b confirms this, with few defects in the trenches, and only some on the mesa. The majority of PS defects occurs on the exterior, with a ring concentrated directly outside the outermost circle. The defect map in the P4VP(PDP) domain follows the same trend: few defects in the trench,

more on the mesa, but most defects are on the exterior of the film. In both maps, there number of junction and terminal points is not the same: there are many more terminal points (red circles) in the PS domain than junction points, with a correspondingly greater number of junction points (yellow squares) than terminal points in the P4VP(PDP) domain.

Individual histograms of the distribution of sin(θ) in each region of the patterns are shown in figure 5d. As expected from the high average in each trench as well as on the exterior, there few places were sin(θ) deviates from 1. The mesa portion has a slight tail away from sin(θ)=1, as expected from the greater number of defects located there. The exterior of the film has, as expected, the greatest distribution of sin(θ), with a mode value of 1. This is due to the fact that 1-2 periodicities on the exterior, the supramolecule continues to align with the outer ring trench.

The periodicity of each concentric circle within a trench is shown to see how the degree of curvature within one and across all three rings affects the supramolecule (Figure 5e). The changes are small, but there is a general trend: the periodicity is smaller toward the interior of the trenches versus the exterior of the trench for each of the trenches. There is local rearrangement, causing a change in periodicity, even if it is small, as the small molecule rearranges across the pattern. The diameter of each concentric PS ring is shown in figure 5f. It is plotted as change in diameter from the inner diameter of the trench it is in so that trends can be compared across all three trenches. The change in diameter is approximately constant across all three rings. Local rearrangement occurs, but there is a desired

feature size that is reached, suggesting templating of the supramolecule in each of the three rings.

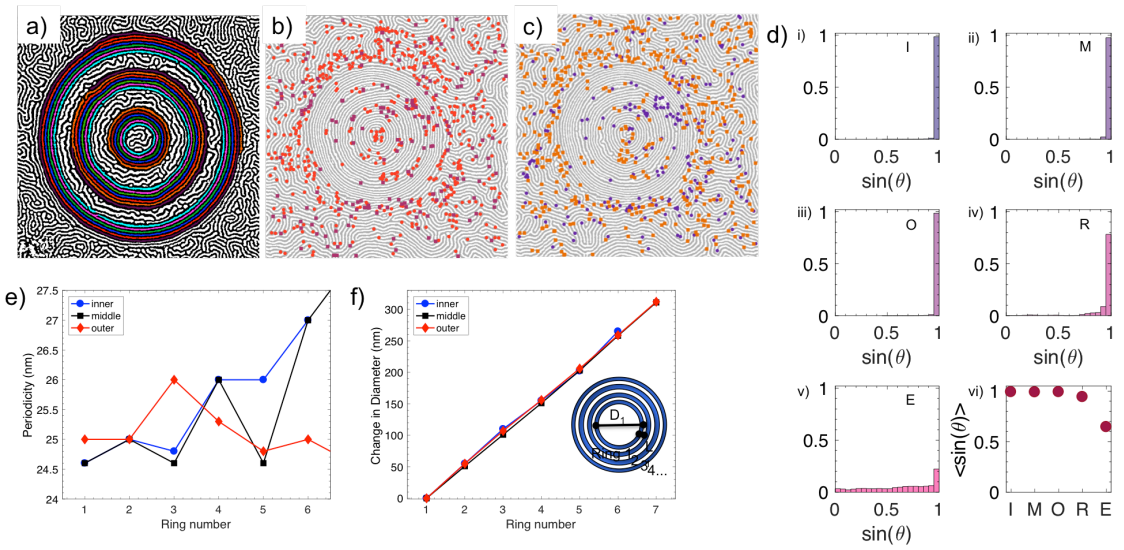

Figure 5: In depth analysis of alignment of the supramolecule with the trench pattern. (a) Colormap showing continuous PS cylinders in the trench, (b) defect map for PS domain, with terminal points in red circles and junction points in purple squares, (c) defect map for P4VP domain, with terminal points in purple circles and junction points in yellow squares, (d) distribution of sin(θ) in each region of the pattern. (e) Periodicity of each PS concentric ring in the three different trenches. (f) Diameter of each ring in the inner, middle, and outer trenches. The diameter is plotted diameter of ring n minus the diameter of the trench it is in so that the change can be compared across the rings.

To further visualize the self-adjusting nature of the assembly process, a larger area image was taken of a supramolecule thin film assembled on P2015

(Figure 6a). From this larger image, the change in morphology and the high number of defects can be more clearly seen. In the orientation and defect map, there are many defects on the exterior (Figure 6b).

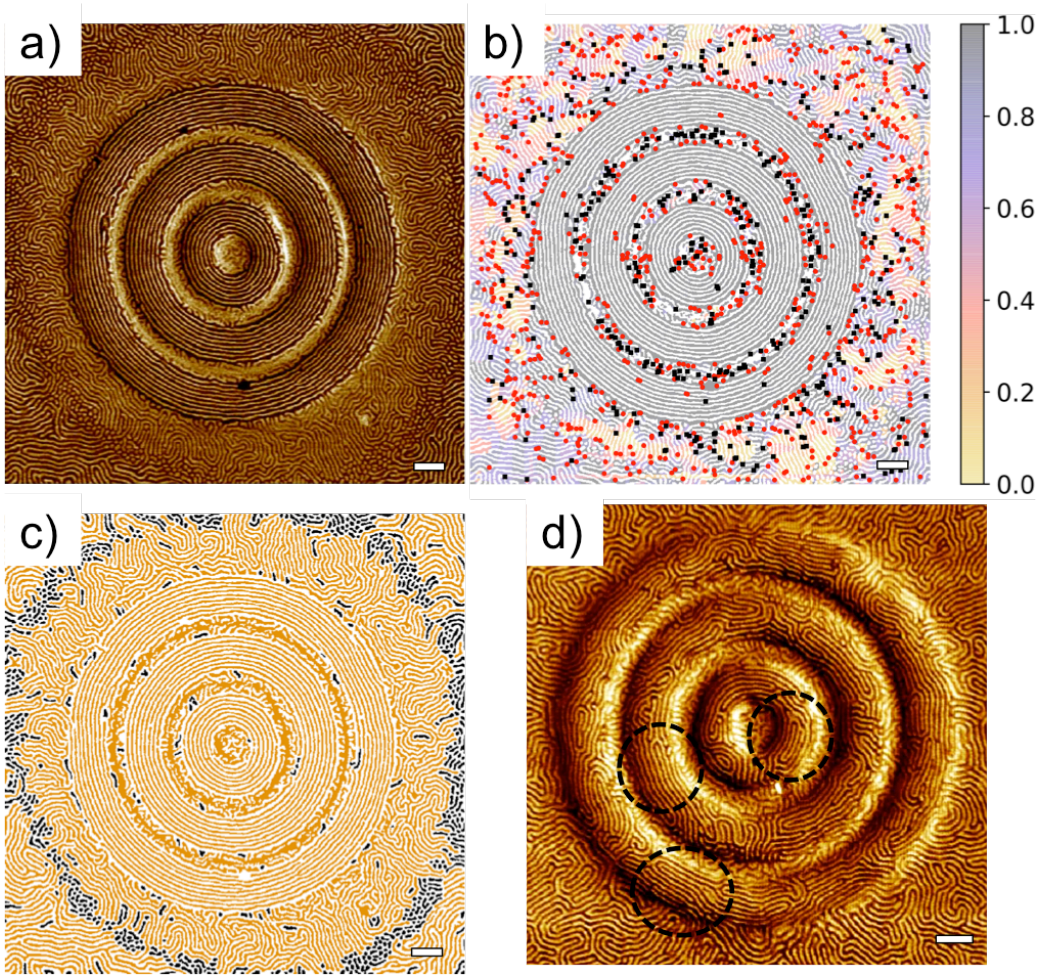

Figure 6: (a) AFM phase image of P2015 with a wider field of view, (b) Orientation color map and defect map of image in (a), (c) Morphology map showing PS cylinders (yellow) or PS dots (black) of image in (a). (d) P2020 solvent annealed to f_s=0.2. Scale bar=200 nm.

In particular, there are many PS termination points that extend in a ring around the pattern for a few hundred nanometers. Figure 6c shows a morphology map of the same image where PS cylinders are yellow, regardless of their length, and PS dots are in black. There is a clear ring 300-400 nm away from the pattern on the exterior of PS dots. Within that ring, most of the defects on the pattern exist and there are many shorter aspect ratio PS cylinders. There is a characteristic distance away from the pattern that there is rearrangement: small molecule is expelled from the trench pattern during the annealing process, and it diffuses to the raised area of the pattern on the mesa and exterior a characteristic distance away.

The proposed mechanism during annealing is as follows: at the beginning, short range diffusion templates a set number of rows into the trench pattern. This is not based on the equilibrium periodicity. Support for this can be seen in Figure 6d, which was taken after the film was annealed a short time, to f_s=0.2. The film is still by and large disordered, but there are regions where the set number of rows has formed that are aligned with the pattern, shown in the circled region. After the number of rows has been set, there is growth along those regions that results in total alignment in the trench pattern. During this process, small molecule is expelled to the mesa and exterior, resulting in a higher defect density, since the higher interfacial area of defects is stabilized by the small molecule, as well as a change in morphology as the P4VP domain is swollen from the excess PDP.

The effect of the solvent removal rate was also explored to understand the origin of the non-equilibrium periodicity in the trench. By allowing a longer

deswelling process post-solvent annealing, it is possible that the system may return to an equilibrium periodicity given time to diffuse.

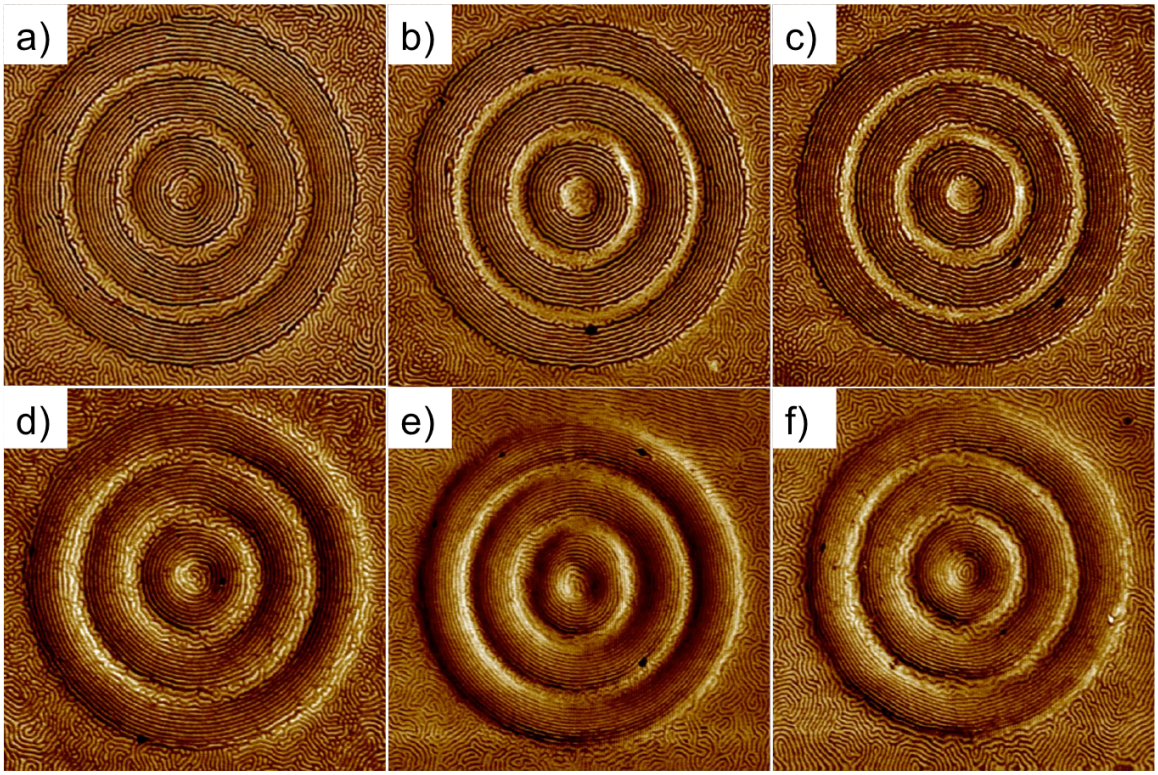

Figure 7: AFM phase images of P2015 with different solvent annealing conditions. The film was annealed with 300 µL $CHCl_3$ with solvent removal time of (a) instantaneous or after (b) 1 minute, (c) 3 minutes, (d) 10 minutes, or the solvent removal was instantaneous and annealed with (e) 175 µL or (f) 600 µL $CHCl_3$.

The smaller periodicity may simply be a kinetically trapped state by instantaneous solvent removal. Figure 7a-d shows P2015 as a function of solvent removal rate. Even when the solvent removal occurs between 1-10 minutes, which is more than twice as long as the annealing process, the same smaller trench periodicity persists.

The drying process does not change the final film: once it reaches an ordered state, it is locked in. The film structure may very well be a kinetically trapped state, but it cannot escape that state. The solvent annealing rate may also affect the final trench periodicity. If the pattern does in fact self-adjust, a very fast annealing time may not allow for this process and the film may not order. A very long annealing time may result in the equilibrium periodicity. The amount of solvent used determines the time it takes to reach the desired f_s. The solvent was varied from 175 μL (Figure 7e) to 600 μL (Figure 7f), as compared to the standard 300 μL (Figure 2c), which took 2.5, 6, and 4 minutes to reach f_s=0.35, respectively. Using a greater amount of solvent resulted in the film dewetting before getting to the desired f_s. For the different annealing times, the supramolecule aligns nicely with the pattern and there is no change in trench periodicity. Interestingly, the exterior of the film and mesa both seem to have a greater grain size on the exterior portion. The pathway taken during solvent annealing, not the rate of swelling or deswelling, determines the final film features in the trench.

3.3 Directed Self-Assembly of Supramolecules With Nanoparticles

Similar experiments were carried using the DSA of a supramolecular nanocomposite, where 5 nm iron oxide particles were added to the film. Table 2 shows the composition of the nanocomposite, including the molecular weight of the supramolecule and NP loading. The same ring patterns were used for the DSA as before.

Table 2: Composition of Nanocomposites

	PS molecular weight (kDa)	P4VP molecular weight (kDa)	4VP:PDP ratio (r)	Equilibrium periodicity (nm)	5 nm NP loading (v%)
NC1	19	5.2	2	31	3
NC2	50	17	1.8	62	3

Figure 8a shows the AFM phase image of P1110 with NC1. The PS domain is light, and the P4VP(PDP)+NP domain is dark. The NPs are difficult to see due to the AFM resolution, but have previously shown to incorporate in prior work[43, 44]. The nanocomposite aligns with the pattern, creating a continuous spiral of PS cylinders from the center of the pattern to the outermost ring, albeit with defects. The changing degree of curvature as the radius increases does not inhibit alignment. Outside the trench, the nanocomposite is oriented isotropically.

The pattern parameters were varied, with both the trench and mesa width increasing, in P1520 (Figure 8b). The nanocomposite aligns in the trench, with the PS domain forming a spiral. On the mesa, the PS cylinders have a smaller aspect ratio, with shorter, discrete lines or dots. There is not a continuous spiral across the entire pattern.

The pattern width increases again in P2015 (Figure 8c). In the trench itself, the nanocomposite aligns with the pattern, a forming continuous spiral, with defects, in each individual trench. This pattern has a greater trench width as well as extending to a larger confinement diameter than P1110 or P1520, but still results in good alignment in the trench pattern: the confinement diameter and degree of curvature can extend over a range of tens to hundreds of nm and still guide the

sample. On the mesa, the PS cylinders are not continuous, but form shorter line, as in P1520. This occurs even on a smaller mesa—both absolutely and relative to the trench width—than in P1520. This suggests an upper threshold on the mesa width to generate a continuous spiral across the entire pattern.

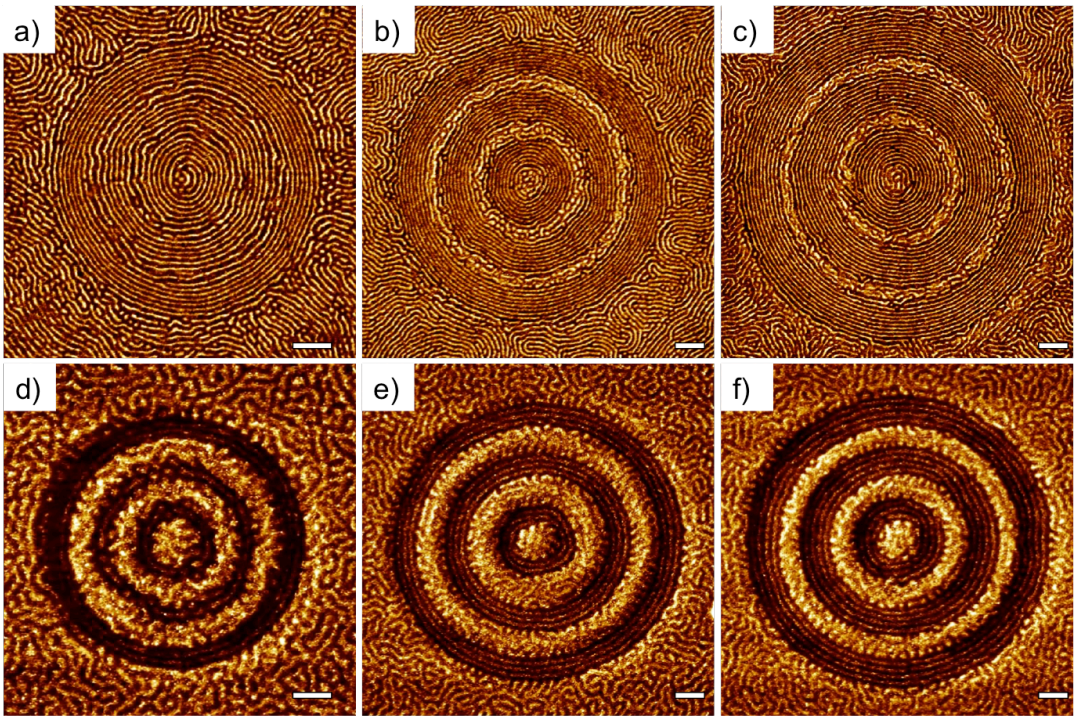

Figure 8: DSA of SM1 (a-c) and SM2 (d-f) with 3v% 5 nm IO NPs in P1110 (a,d), P1520 (b, e), and P2015 (c, f). Scale bar=200 nm.

A nanocomposite with a larger periodicity, NC2, aligns with P1110, P1520, and P2015 (Figure 8d-f). The nanocomposite on the mesa does not align at all with the underlying pattern for any of the trenches, though this may be a function of film thickness. For the larger feature size supramolecule, the degree of curvature affects the alignment: the inner trench on all three patterns, which has the tightest curvature, has one fewer PS ring than the outermost trench pattern. For P1110, the middle trench also has one fewer PS ring than the outermost trench. The number of

rings in the trench can vary from 1-4, which is controllable by changing the trench width as well as degree of curvature. Neither of the nanocomposites is commensurate with the patterns used here. However, successful alignment within the trench is possible for a radius of curvature between 150 nm and 1050 nm with varying confinement width and nanocomposite feature size.

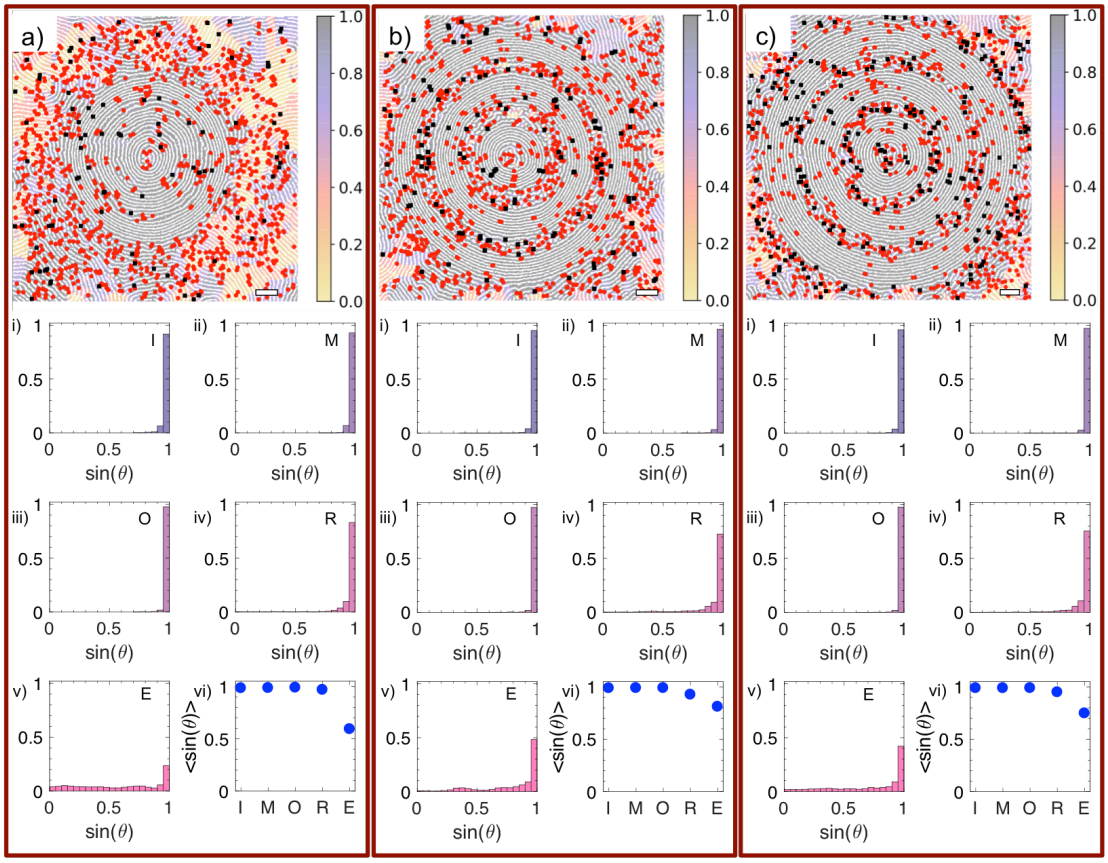

Figure 9: Colormap of alignment of NC1 with trench pattern and defect map of PS domain from Figure 1 a-c for (a) P1110, (b) P1520, and (c) P2015 with SM1. Junction defects are black and terminal points are red. A histogram with the frequency of sin(θ) is shown for the (i) inner trench (I), (ii) middle trench (M), (iii) outer trench (O), (iv) raised mesa between trenches (R), and (v) exterior of the pattern (E) is shown, as is (vi) <sin(θ)> in each region. Scale bar=200 nm.

To better understand the assembly mechanism, the alignment of NC1 with each pattern was quantified by examining the angle between the tangent line at each point in the nanocomposite with the radius, θ. As expected, the color maps indicate excellent alignment of the nanocomposite with the trenches. In P1110, the continuous spiral across the entire pattern has almost perfect alignment in each of the three rings, as can be seen in by $\langle \sin(\theta) \rangle$ and the histogram (Figure 9a i-iii). The mesa has slightly lower average alignment, but still well above $\langle \sin(\theta) \rangle = 0.9$. There are some defects, located mainly on the mesa.

The nanocomposite on the exterior is oriented isotropically, except for in the area directly surrounding the exterior ring, where it remains aligned for 1-2 periods. However, there is a high concentration of terminal defects in a ring surrounding the pattern. This is a result of a morphology change: rather than continuous PS cylinders with a high aspect ratio of shorter lines with a smaller aspect ratio and PS dots.

In P1520, the color map shows good alignment of the nanocomposite in each of the three trenches, with $\langle \sin(\theta) \rangle = 0.98$ (Figure 9b). The nanocomposite on the mesa also aligns well with the trench, with $\langle \sin(\theta) \rangle = 0.9$. Despite this, there are many defects on the mesa, most of which are terminal points. On the exterior of the film, there are similarly many terminal points. This once again shows a change in morphology on the mesa and exterior of the film. The alignment on exterior once again extends to a few periodicities outside the trench. Given the larger size of the pattern, there is less area on the exterior, so $\langle \sin(\theta) \rangle$ is closer to 1 than perhaps it should be.

The alignment of the nanocomposite of P2015 is similar to P1520 (Figure 9c). The nanocomposite is highly aligned in the trench ($\langle \sin(\theta) \rangle = 0.98$) and on the mesa ($\langle \sin(\theta) \rangle = 0.95$). There are more defects in the trenches in P2015, likely a result of the larger confinement width. Once again, there are many PS terminal points on the mesa and especially the exterior. In the regions on all three patterns where alignment is the lowest, there is a change in morphology. The pattern self-adjusts, resulting in small molecule being expelled to the mesa and causing the PS cylinders to form discrete lines and dots.

The self-adjusting nature of the assembly process on the circle patterns results in a decrease in periodicity in the trench as compared to the mesa and the equilibrium periodicity. Figure 10a-c shows the change in periodicity as a function of distance from the center of the pattern (top), as well as highlighting the periodicity in the trenches themselves (bottom).

For P1110, the periodicity in the trenches is smaller than the equilibrium periodicity (Figure 10a). The periodicity on the mesa is larger than in the trench. On the outer ring/exterior interface, the periodicity is on the order of the mesa periodicity. Further onto the exterior, the periodicity decreases somewhat. This pattern of periodicity changing suggests a global adjustment: there is an increase in periodicity on the raised portions of the pattern as the small molecule is expelled from the trench, which has a smaller periodicity.

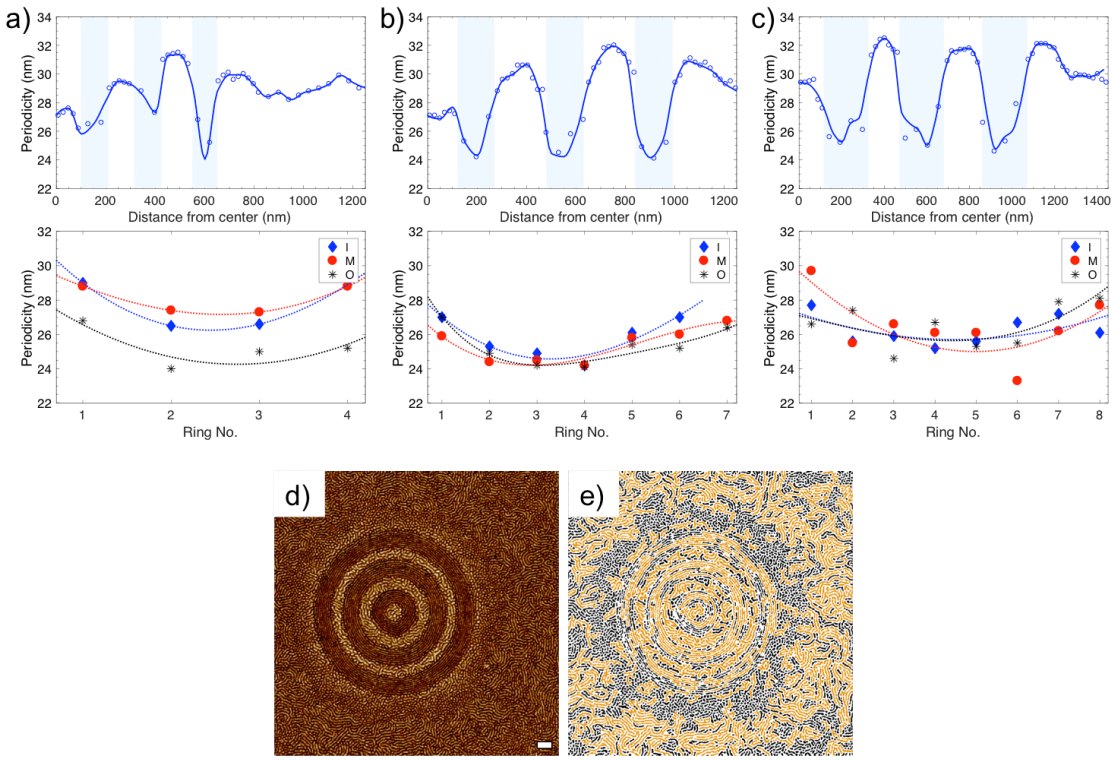

Figure 10: The periodicity as a distance from the center of the pattern (top) and the periodicity of each PS cylinder in the inner, middle, and outer trench (bottom) for (a) P1110, (b) P1520, and (c) P2015. Region in trench is marked by shaded area. (d) Zoomed out AFM phase image of 150 nm wide trench and (e) color-coded morphology (black=dots, yellow=cylinders) showing phase change. Scalebar =200 nm.

In the trench itself, the periodicity is not uniform across all PS rings, but rather varies by ~3 nm. For the inner, middle, and outer trench, the periodicity is at its lowest in the middle of the trench. The inner and middle rings have approximately the same periodicity values at each point across the trench, with a minimum periodicity of ~26.5 nm. The outer ring has smaller periodicity, with its

minimum reaching 24 nm. This represents a change of 22% from the equilibrium periodicity. The changing periodicity within each trench demonstrates the local self-adjusting nature of the supramolecular nanocomposite.

P1520 and P2015 have the same trend in the change of periodicity as a function of distance from the center of the trench as P1110 (Figure 10b, c). The trench periodicity is smaller than equilibrium, the mesa periodicity is ~7 nm larger, and the exterior has a similar periodicity as the mesa on the interface with the outermost ring before decreasing slightly further away from the pattern. For both patterns, there are different periodicities within each trench. For P1520, the change in periodicity across the trench is the same for all three rings. The minimum periodicity is in the middle of the trench and has a value of 24 nm, which is the same as the outer ring periodicity in P1110. In P2015, the minimum trench periodicity is in the middle for all three rings and is 25 nm for the inner and outer ring and 24 nm for the middle ring. For each of the three patterns, the trench periodicity changes by ~4 nm, showing the local self-adjusting nature.

The global self-adjustment is seen in a larger area AFM phase image of NC1 in P1520 with 5v% IO NPs (Figure 10d). The increase in NPs makes the trend observed in Figure 2 more obvious. There is a change in morphology in a ring surrounding the pattern. Figure 3e shows the same image as in Figure 3d, but the morphology has been color-coded: PS cylinders are in yellow, and PS dots are in blue. On the mesa, and the exterior, there is a high concentration of dots.

Wherever the pattern is not aligned, there is a change in morphology to short PS cylinders and dots. This occurs in circular patterns with and without NPs, which

strongly points to the small molecule rearranging, rather than the NP rearranging, although that is possible as well. This was hypothesized previously in the DSA of a supramolecule on a linear pattern[45]. The change in periodicity and the change in morphology suggest local and global self-adjustment, rather than commensurability, drive the assembly process.

3.4 Discussion

Alignment of a supramolecule with or without NPs with rings of various widths, degrees of curvature, and molecular weight of the supramolecule is possible with a high degree of order. For all patterns used here, the periodicity in the trench pattern is smaller than equilibrium periodicity. In DSA of BCPs, the trench periodicity can shrink by up to ~10% of the equilibrium periodicity and still align. In a system without NPs, P1515 is approximately commensurate with the periodicity of the supramolecule. P1110 trench is ~$3.5L_o$, which means that commensurability requirements dictate there would be some regions with 3 rows of a much larger periodicity (~36.6 nm) and some regions with 4 rows and a much smaller periodicity (27.5 nm). This large change would be spread among only a few polymer chains, meaning the entropic penalty per chain would be very large, so that the supramolecule should not align at all. The significant deviation from the equilibrium periodicity is not expected based on commensurability. Table 3 shows how the actual trench periodicity in samples with NPs deviates from the commensurate periodicity without NPs. Under those conditions, it is expected the BCP will compress or expand so there are an integer number of rows in the trench. If the

trench width divided by L_o, n, is not an integer, there will be either n+1 or n-1 rows. Based on the predicted number of rows, a commensurate periodicity, L_c, and the deviation of that periodicity from L_o, can be calculated.

Table 3: Predictions for trench periodicity under commensurability (L_c) and the actual measured periodicity in the trench (L_t) for different trench widths and how they deviate from the equilibrium periodicity (L_o=31 nm) in a supramolecule without NPs

	n*	L_c (n-1) (nm)	% change	L_c (n+1) (nm)	% change	L_t (nm)	% change
P1110	3.54	36.6	18	27.5	11	25	19
P1515	4.8	37.5	21	30	3.3	25	19
P2015	6.45	33.3	7.5	28.6	7.8	25	19

For P1110, P1515, and P2015, the percent change of L_c from L_o is smaller than the percent change of the actual trench periodicity, L_t from L_o. For these three patterns, there is a commensurate periodicity that would result in ~10% change in the periodicity from L_o. And yet, that is not the periodicity that is adopted in the trench pattern. The assembly process is not driven by commensurability, but instead, there is a new pathway taken in the DSA of a supramolecule.

The new pathway relies on the self-adjustment of the supramolecule. This self-adjustment is seen in the smaller periodicity in the trenches, regardless of trench width or confinement diameter, the change in morphology on the mesa and

exterior of the pattern. The proposed pathway of assembly is shown in FIGURE. During the assembly process, a specific number of rows is templated into the trench. Once these are set, the order grows in the direction of the trench. Locally, the small molecule is expelled to nearby mesas and distributed unevenly in the trench. Globally, the movement of the small molecule results in a change in morphology on the mesa and surrounding the pattern, leaving a small molecule poor trench and small molecule rich exterior. This pathway is unique to a multicomponent system.

3.5 Conclusion

The DSA of a supramolecule was shown to be a successful to align supramolecules with and without NPs into a ring shaped pattern. It was shown that commensurability of the periodicity supramolecule with the trench does not dictate the final film features. These highly versatile films are not limited by NP type, periodicity, or pattern width due to the self-adjusting nature of the supramolecular self-assembly. Locally, the pattern can rearrange, resulting in a smaller and variable periodicity in the trench. Globally, there is cooperativity across the entire pattern as seen in the change in morphology, periodicity, and long-range order in the regions just outside the pattern. The mechanism during self-assembly is as follows: during the annealing process, the (non-commensurability dictated) number of rows is set in the trench, and from that template, the supramolecule follows it to become aligned throughout the entire trench, and then order on the mesa likely follows. During the alignment process, small molecule is expelled to the raised portions, causing a high defect density and change in morphology from long PS cylinders to

shorter aspect ratio cylinders and dots. This change in morphology exists a characteristic distance away from the pattern. The alignment in the trench does not depend on the time to anneal it or the time over which solvent is removed. The pathway that occurs without regard to commensurability offers new opportunities for DSA.

3.6 Methods

Materials

PS(19 kDa)-*b*-P4VP(5.2 kDa) (PDI = 1.06) and PS(50 kDa)-*b*-P4VP(17 kDa) (PDI = 1.15) were purchased from Polymer Source, Inc. 3-*n*-Pentadecylphenol (90%–95%) was purchased from ACROS Organics. Chloroform (Amylene as preservative) was purchased from Fisher Scientific. 5 nm iron oxide NPs dispersed in chloroform were purchased from Ocean Nanotech.

Sample Preparation

Supramolecular solutions were prepared by dissolving the polymer and the small molecule in chloroform and then stirring for 72 h. Thin films were prepared by spin-coating the mixed solutions onto silicon wafers at 3000 rpm. Sample thicknesses were measured using a Filmetrics F20 interferometer. For solvent annealing, samples were annealed using 300 μL of $CHCl_3$ injected inside a 250 mL top-capped jar at 24°C. Once the film thickness of the nanocomposite thin film reached the desired thickness, the jar was opened and the $CHCl_3$ vapor inside the jar was allowed to freely evaporate. Solvent fraction is the volume fraction present in the swollen film during annealing, calculated as $f_s = \frac{t_f - t_i}{t_f}$ where t_f is the final film

thickness and t_i is the initial film thickness. The solvent annealing process was stopped at the desired f_s and the sample was quenched within 10 seconds.

Lithographic Pattern Fabrication

Circular patterns were fabricated using electron beam lithography with dimensions shown in table 1. All patterns have a height of 50 nm.

Atomic Force Microscopy (AFM)

AFM was performed on a Bruker Dimension Edge. The spring constant of the cantilever was 5–10 N/m with a resonant frequency in the range 90–210 kHz. The set point for the auto tune was ~6.0 V. The set point amplitude was 80–90% of the free vibration value.

Image Analysis

Image analysis was performed in Python using methods inspired by the *ADAblock* application[46]. The periodicity of the supramolecule determined from the fast Fourier transform (FFT). For defect analysis, AFM phase images were binarized using a local thresholding technique. NPs were deleted by filtering out small elements. The images were then skeletonized. Defects were found by scanning each pixel: a pixel with two nearest neighbors was considered defect-free, a pixel with only one nearest neighbor was labelled an end, and a skeleton pixel with three or more nearest neighbors was labelled a junction. This analysis was done for both the PS and P4VP(PDP) phase.

Chapter 4
High Molecular Weight-Based Polymer Nanocomposites with Feature Sizes Greater than 50 nm

4.1 Introduction

Hierarchically structured nanocomposites have shown promise for creating functional materials[1-3]. These materials can arrange nanoparticles (NPs) into 1-, 2-, and 3-dimensional assemblies to harness the unique optical, electronic, magnetic, and thermal properties of the NPs[4]. While several methods have been developed to create such nanocomposites, block copolymer (BCP)-based supramolecules are of particular interest[5-8]. Supramolecules, formed from a BCP backbone with a small molecule non-covalently bonded to one of the blocks, have been studied for the past 20 years due to their ability to form hierarchically structured functional materials[9-13]. Structural control over the supramolecules in bulk and thin film morphology has been achieved, with a variety of morphology, periodicity, and long-range order possible[14-18]. This structural control was first studied in supramolecules without NPs, but has been shown to extend to nanocomposites with different NP size and shape[19-24]. However, both traditional BCPs and supramolecules are often limited to small feature sizes.

The characteristic periodicity of a BCP or supramolecule is often limited to 10-50 nm due to the thermodynamic and kinetic restraints of self-assembly. The periodicity of a BCP scales with its molecular weight (MW) as well as the driving force for separation, given by the Flory-Huggins interaction parameter, χ[25, 26]. As the MW increases, the degree of entanglement and the viscosity of the polymer sharply increase, generally following $\eta \propto MW^{3.4}$ in polymer melts, leading to a reduction in mobility[27]. To circumvent the limitation imposed by viscosity and entanglement and achieve periodicities greater than 50 nm, homopolymers can be added to a BCP to

swell one or both domains, thereby increasing the periodicity[28-30]. This can be successful, but is limited due to the potential of macrophase separation of the homopolymer and BCP[31-33]. Periodicity as large as 200 nm in can be achieved in thin films via a combined thermal and solvent annealing process, although this takes several hours to accomplish[34]. Other strategies use bottle-brush copolymers, which have periodicities on the order of the contour length of the backbone[35, 36]. Thermally switchable supramolecules with large MW have been demonstrated in bulk[37]. There, the large periodicity is key to tuning the photonic bandgap. Despite successes in generating functional composites with large periodicity, there are still limitations. Processing time is on the order of several hours to days and the structures are often limited to equilibrium structures in bulk.

Polymer nanocomposites have also been limited by the size of the NP that can be incorporated. For traditional BCP systems, the incorporation of NPs causes a loss of entropy due to chain stretching. When the ratio diameter of the NP (d) to the size of the block into which it is incorporating (L) is greater than 0.3, the particle will be expelled from the polymer matrix and phase separate[38, 39]. Coupled with the limitation on domain size, this means particles larger than ~10 nm are difficult to incorporate. Supramolecules have been shown to circumvent this limitation. By controlling the kinetic pathway during assembly, NPs as large as 20 nm can be incorporated into a supramolecule thin film, with a d/L ratio of greater than 1, to generate nonequilibrium structures[40-42]. To create functional nanocomposites, there must not be limitations to the feature sizes (periodicity or NP diameter), new morphologies must be reached, and processing should take minutes.

Here, the kinetic pathway of assembly of high MW-based supramolecular nanocomposites was investigated. It was determined that NPs facilitate the assembly process by modulating the polymer viscosity, allowing for long-range order as well as inducting exact morphologies for three different MW supramolecules when coupled with solvent annealing. NP size, NP loading, solvent annealing condition, and MW were all found to be handles that could be used to create thin films with specific feature sizes, morphologies, and interparticle distances. This work begins to create a roadmap for making exactly tunable nanocomposite thin films without size limitation via modulation of the mobility of the components.

4.2. High MW Assembly Without and With Nanoparticles

The supramolecule used here was polystyrene-*b*-poly(4-vinylpyradine)(pentadecylphenol)$_r$ (PS-P4VP(PDP)$_r$). Four different MW supramolecules were used in this study (Table 1). The four supramolecules were constructed so that the volume fraction of the P4VP(PDP) block (f_{comb}) is ~0.65. The volume fraction and size of the NPs was systematically varied for SM1, SM2, and SM3 to determine the effect of NP incorporation on the assembly process of high MW supramolecules. SM0 has been extensively studied, and is included for the sake of comparison.

Table 1: Molecular weight and morphology of supramolecules in bulk

Sample	$M_{n,\,PS}$ (g/mol)	$M_{n,\,P4VP}$ (g/mol)	*r*	f_{comb}	Bulk Morphology
SM0	19000	5200	1.7	0.62	Cylinder
SM1	47000	10000	2.4	0.63	Cylinder
SM2	50000	17000	1.8	0.68	Cylinder
SM3	104000	30000	2	0.66	Cylinder

Initially, SM1, 2, and 3 were studied in bulk without NPs (Figure 1). The P4VP(PDP) domain was stained with iodine and so appears as the dark domain in the transmission electron microscopy (TEM) images. In bulk, SM1, SM2, and SM3 form a hexagonally packed cylindrical morphology.

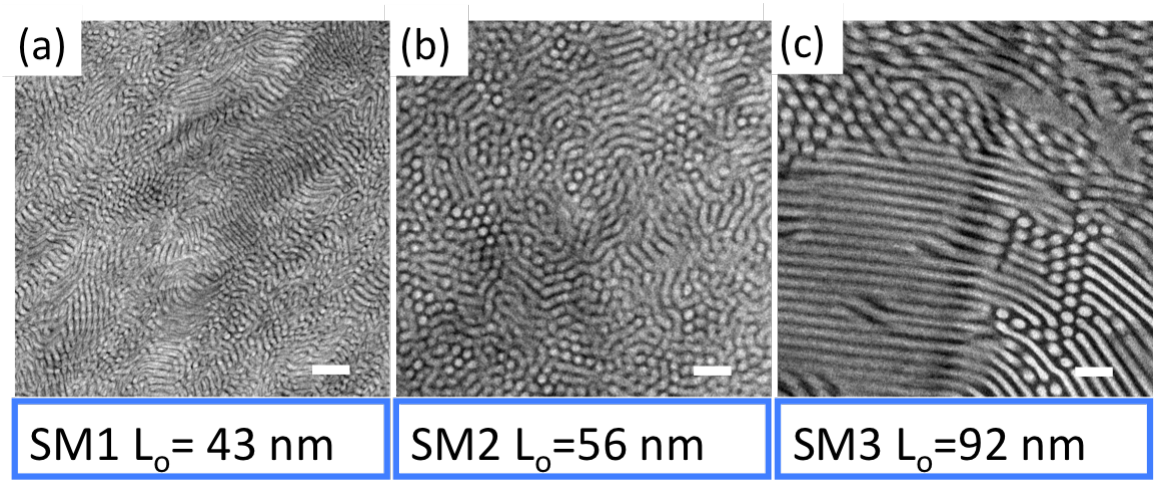

Figure 1: TEM images of bulk samples of (a) SM1, (b) SM2, and (c) SM3. P4VP(PDP) domain has been stained with iodine. Scale bar=200 nm.

SM1 has a periodicity of ~45 nm, SM2 has a periodicity of ~55 nm, and SM3 has a periodicity of ~90 nm. The long-range order of these samples is limited: each TEM image shows several different orientations of the grains. Interestingly, the shortest grain size is seen in SM2 rather than the higher MW SM3. These bulk samples set the thermodynamically expected morphology and periodicity against which thin film samples will be compared

These supramolecules were processed into thin film via solvent vapor annealing. Solvent annealing has been shown to be a necessary step for giving the samples sufficient mobility to create ordered structures, and that the solvent annealing condition will determine the grain size of the film[43, 44]. The films were annealed to a desired solvent fraction (f_s) and then quenched within 10 seconds.

Figure 2 shows SM0-4 annealed to two different solvent fractions, f_s=0.35 and f_s=0.5.. The low MW sample, SM0, has clear microphase separation and long-range order at both solvent annealing conditions. For the high MW samples, SM1-3, this behavior is not observed: the long-range order of the thin film is poor under the annealing conditions used here. As the MW of the supramolecule increases, the long-range order decreases. For SM3 (Figure 2d), the highest MW sample, there is limited microphase separation present at all, unlike the bulk sample and lower MW samples. For SM 1 and 3, increasing the solvent fraction causes the system to disorder rather than changing the grain size.

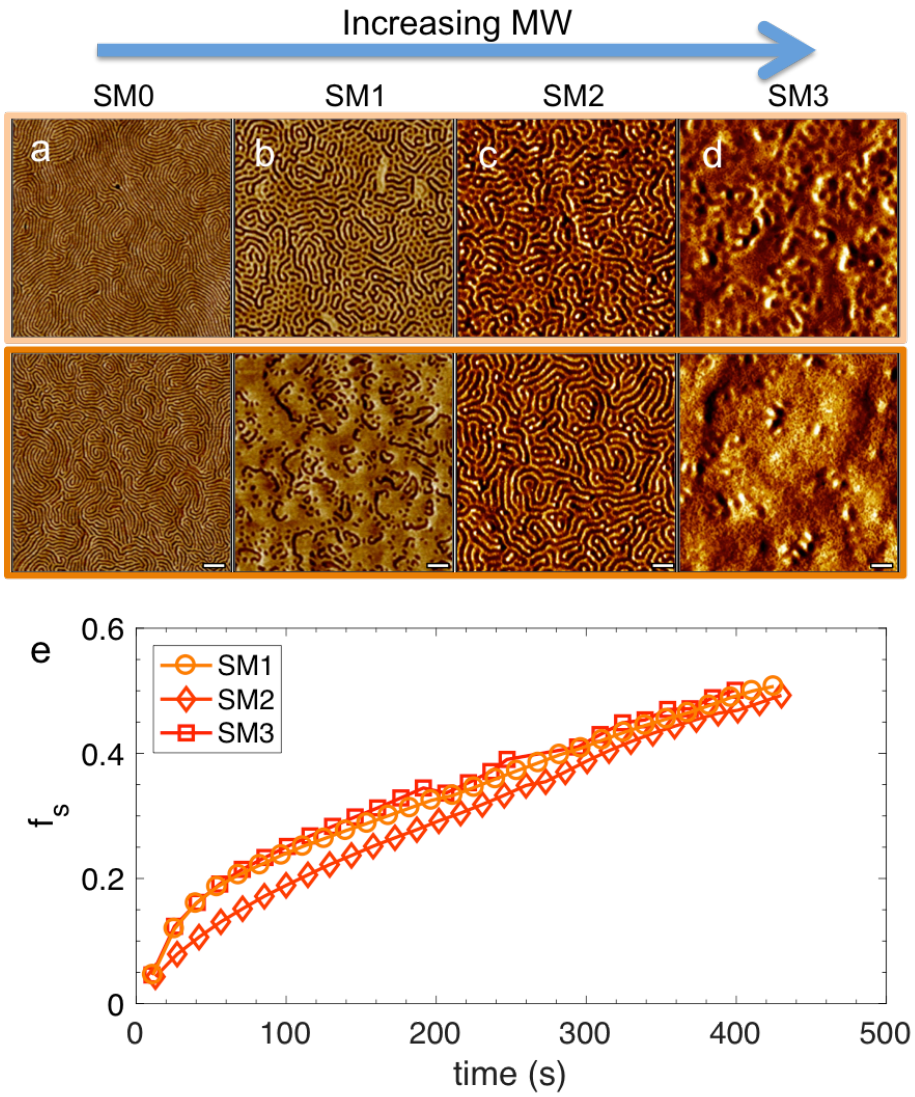

Figure 2: Phase image of supramolecular thin films of four MWs at two different annealing conditions (a) SP4, (b) SP1, (c) SP2, (d) SP3. Top: f_s=0.35. Bottom: f_s=0.5 Scale bar= 200 nm. (e) Profile of film thickness of the four samples during the solvent annealing process.

For SM 2, increasing the solvent fraction increases the grain size slightly, but the maximum grain size is on the order of 10s of nm. The higher viscosity of the high MW samples limits long-range order. The swelling profile of the films during the

annealing process is shown in Figure 2e. The profiles are remarkably similar: the MW of the polymer does not affect the rate at which the solvent vapor enters and swells the thin film. Rather, the lack of long-range order originates from the limited mobility of the larger MW polymer even as solvent is added.

4.3 High MW Assembly with Large Nanoparticles

While there is limited ordering in high MW films without NPs, the incorporation of NPs greatly changes the resulting films. NPs with diameters between 5-25 nm at a loading of 3v% were incorporated into SM1, SM2, and SM3 (Figure 3). For each thin film, the periodicity and d/L ratio was calculated. The addition of NPs leads to clear a clearly ordered structure for all sizes of NPs and all supramolecules used. However, different morphologies are present depending on the size of the NP and the MW of the underlying supramolecule. For the highest MW-based polymer, SM 3 (Figure 3c), the incorporation of NPs has the most obvious effect: there is clear microphase separation and structure formed, unlike in the pure supramolecule sample. The incorporation of NPs increases the mobility of the system sufficiently so that an ordered structure can be formed within a matter of minutes under solvent annealing. Particles with up to a d/L ratio of 0.4 were incorporated into the supramolecule matrix. For SM3, particles of up to 30 nm were added to reach a larger d/L ratio, 0.29. By changing the MW, a greater library of structures and features are achievable.

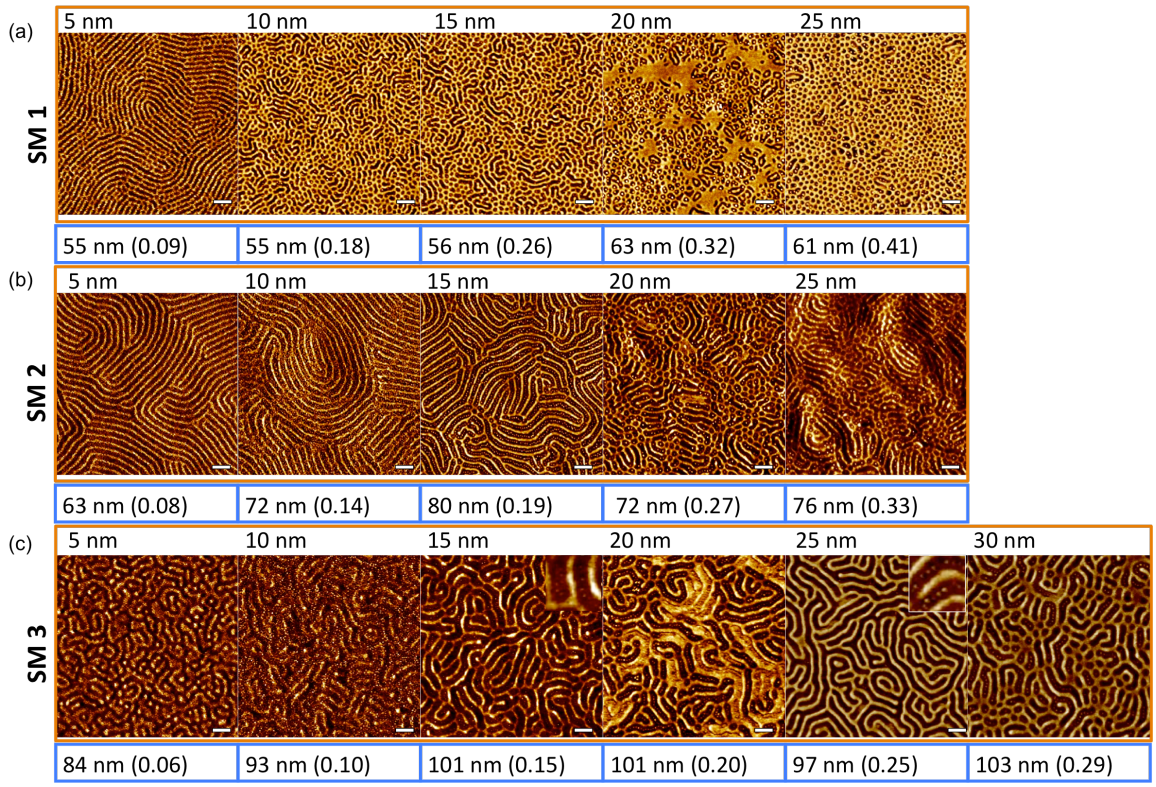

Figure 3: AFM phase images of supramolecule thin films of (a) SM1 with 3v% 5-25 nm NPs, (b) SM2 with 3v% 5-25 nm NPs, and (c) SM3 with 3v% 5-30 nm NPs. The periodicity of each film is shown in the box below, as is the d/L ratio in parentheses. Insets are used to show NP packing the in domain when it cannot be directly visualized from the larger AFM image. Scale bar=200 nm.

The morphology transitions from a parallel cylindrical morphology to a honeycomb-like structure as the NP size increases. For SM1, this transition occurs at d/L~0.18. For SM2, the transition occurs at d/L~0.27. For SM 3, only a partial honeycomb structure is seen when d/L=0.28. Previously, this same honeycomb structure has been seen in a lower molecular weight supramolecule nanocomposite thin film[40, 42]. There, the appearance of this structure was attributed to the diffusion

kinetics of the NPs in the supramolecule matrix, causing co-assembly of the NPs and supramolecule, as opposed to supramolecule-guided assembly of the NPs. The appearance of this structure occurred at high solvent fraction, where the supramolecule matrix is somewhat because of the low driving force for separation. This allows for fast NP diffusion through the supramolecule matrix and a low energetic barrier. Here, the similar arguments can explain the honeycomb structure and the dependence of MW on where it occurs. In a high MW system, the diffusion of the supramolecule will be slow because of high viscosity and entanglements. The diffusion of the NP, however, will be faster, allowing for a greater number of particles to reach the surface of the film. Since the system is still largely disordered, there will be a direct pathway for the NPs to reach the surface with low energy barrier. Having several large particles on the surface of the film is necessary for the formation of this structure: the particles force the curvature of the supramolecule for coassembly of the supramolecule and the NPs. Larger particles, as defined by the d/L ratio, are needed to guide the curvature of the supramolecule, but must be balanced with the overall diffusion of each of the components. As the MW of the supramolecule increases, the mobility will decrease, making the co-assembly harder because particles and supramolecule alike do not diffuse as much due to the highly viscous matrix. This explains why the full honeycomb structure is never formed for SM2 and barely seen for SM3: the system is stuck in a kinetically trapped state. Additionally, it is worth nothing that the smaller d/L ratio needed to force a change from the cylinder to honeycomb morphology for SM1 could be due to the amount of free small molecule. SM1 has a greater amount of free small molecule than SM2,

which could facilitate the formation of the honeycomb structure at smaller d/L. The small molecule could help minimize any entropic penalty associated with the greater curvature of the supramolecule wrapping around a particle and make the increased interface from this morphology less energetically costly.

While long-range order is possible with SM1 and SM2, true long-range order is never achieved with SM3. This is true both in the cylindrical morphology as well as the honeycomb morphology. While adding NPs is enough to drive the formation of an ordered structure in a high MW polymer, the much slower dynamics of the highest MW polymer still do not allow for the formation of long-range diffusion that is necessary for long-range order.

The periodicity of the supramolecule increases as the MW of the polymer increases, as expected. SM1 has a periodicity of ~55 nm, SM 2 has a periodicity of ~65 nm, and SM 3 has a periodicity of ~90 nm. The exact periodicity is a function of the size of NP incorporated as well as the MW of the supramolecule (Figure 4a). The periodicity in thin film with small NPs are approximately the same as the values in the bulk supramolecule without NPs, suggesting that the incorporation of small NPs does not significantly change the chain conformation of the supramolecule.

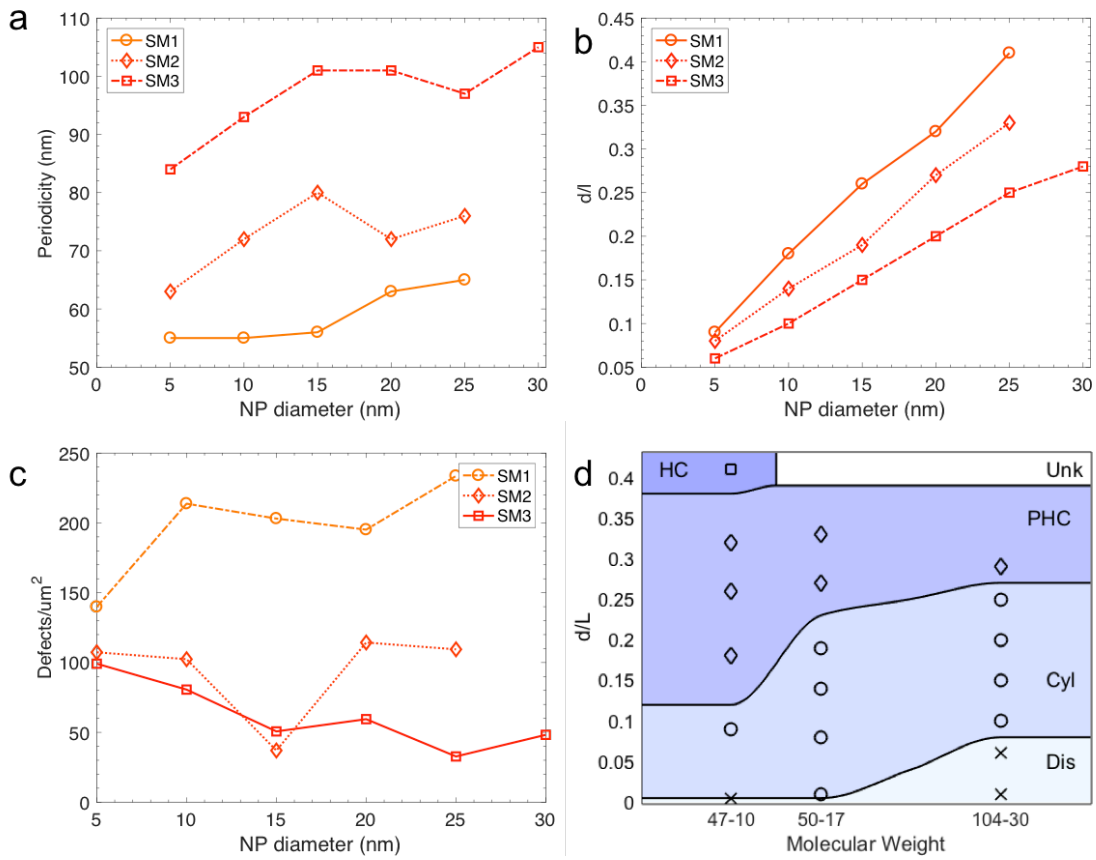

Figure 4: (a) Periodicity and (b) d/l ratio as a function of NP diameter, and (c) defect density for SM1, 2, and 3. (d) Phase diagram as a ratio of molecular weight and d/L ratio.

The trend for the periodicity of SM1 is slightly different than for SM2 and SM3. For SM1, there is little change in the periodicity until 15 nm particles are added, which begins an uptick of the periodicity, resulting in a final periodicity that is 18% larger than the initial periodicity. The increase in periodicity occurs when the morphology transitions from parallel cylinders to a honeycomb structure. For SM2 and 3, the increasing size of the NP increases the periodicity until the phase transition from parallel cylinders to honeycomb. At the transition point, the periodicity decreases somewhat, but then starts to increase again. For SM 2, the

largest periodicity is 27% larger than the smallest periodicity, and for SM 3, the largest periodicity is 25%. These large changes give the films quite a bit of tunability within a single supramolecule.

The d/L ratio increases sharply and its shape follows the same basic trends as the periodicity, as expected (Figure 4b). The slope of the line is basically constant, until the onset of the honeycomb structure, where there is a sharper slope. When films form cylindrical structures, the d/L ratio guides the packing of NPs in the P4VP(PDP) domain. Around d/L of 0.2, there is a transition from multiple rows of particles in the domain to a single row of particles, as seen in SM2 and SM3. This also affects the interparticle distance, giving the system another handle by which it can be tuned.

The defect density of each of the three supramolecules is shown in Figure 4c. Here, automated image analysis identified junction points and terminal points in each AFM phase image to give a defect density. The trend for all three supramolecules is the same: as the grain size grows, the number of defects decreases. Once the honeycomb morphology starts to form, there are a greater number of defects. The honeycomb morphology inherently has more junctions, explaining this trend. SM3 has the fewest defects per area, despite its relatively short grain size for all conditions.

From this analysis, a phase diagram can be made as a function of the MW and the d/L ratio (Figure 4d). As the MW of the supramolecule increases, the cylindrical structure exits over a greater value of d/L. This phase diagram reflects the underlying kinetics that determine each structure. The honeycomb is a kinetically

determined structure. It only exists over an entire film when film with the lowest MW supramolecule, SM1. The supramolecule must have sufficient mobility to achieve this structure. A partial honeycomb structure (PHC) is possible for all 3 supramolecules used here, but the onset of where the honeycomb occurs depends on the MW of the supramolecule. For higher MW supramolecules, there is a higher d/L ratio needed: there must be more of an entropic penalty associated with chain deformation to force the switch to a coassembly regime. This phase diagram begins to map out the necessary conditions to get specific structural control without changing the supramolecule used. There is greater structural control in the lowest MW supramolecule, but this is likely due to the missing corner of the phase diagram. Currently, the particle sizes with correct ligand chemistry, solubility, and monodispersity are limited to about 30 nm or less, so higher d/L ratios in the highest MW supramolecule are not possible.

Detailed image analysis was conducted into three films that form a cylindrical morphology and one that forms a honeycomb morphology sample to visualize the defect. Junction points, where the supramolecule domain branches in three or more directions, and terminal points, where the supramolecule ends, are shown for both the PS phase and the P4VP(PDP) phase. The NPs were removed prior to image analysis (Figure 5). An orientational order map for each was also made to give a visual representation of the grain size.

For SM 1, the longest cylindrical grain size was with 5 nm (Figure 5a) The PS domain (middle column) in particular has many junction defects, accompanied by several terminal defects in the P4VP(PDP) domain (right column). This happens as

the morphology shifts to the honeycomb morphology. Despite the high defect density, there are still fairly long grain sizes, as can be seen in the orientation domain map (left column).

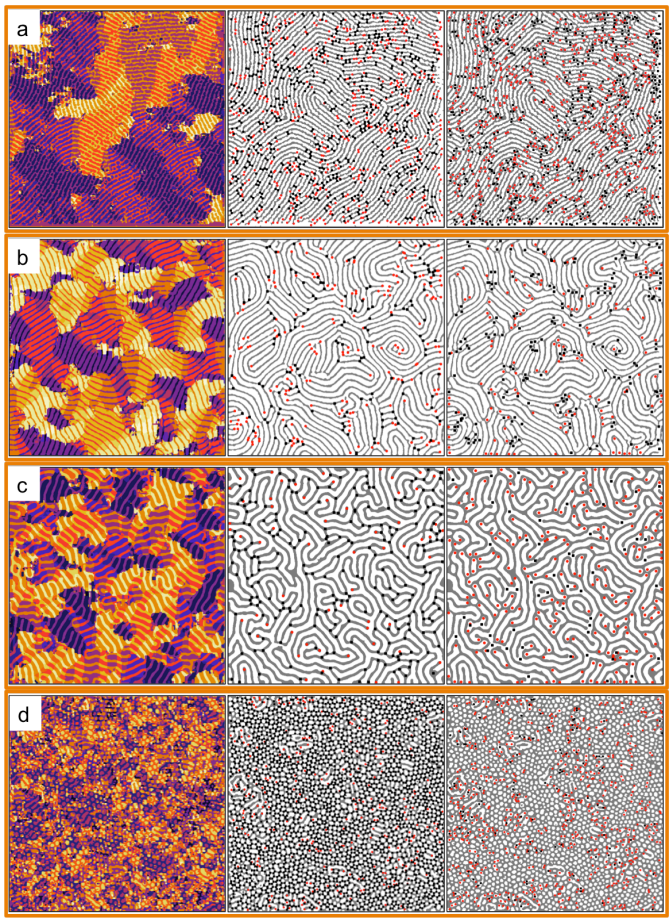

Figure 5: Defect Analysis for (a) SM1 with 3v% 5 nm particles (b) SM2 with 3v% 15 nm NPs, (c) SM3 with 3v% 25 nm NPs and (d) SM1 with 3v% 25 nm NPs. Left column is a orientation domain map, center column shows terminal point (red) and junction (black) defects in PS phase, and right column shows terminal point (red) and junction (black) defects in P4VP(PDP) phase. Each image is 3 μmx 3 μm.

The defects are not forcing a change in direction of the PS cylinders, but rather occurring as a phase transition from cylinders to honeycomb begins. This is contrasted to the case where there is a full honeycomb structure across the entire film, given for SM1 with 25 nm particles (Figure 5d). Here, there is a very high defect density in the PS domain, as the full honeycomb structure has several defects. The orientational order map appears to have no order, because the PS cylinders curve around the NPs.

SM2 with 15 nm particles forms a well-ordered structure with few defects in either phase (Figure 5b). The PS and P4VP(PDP) domain form continuous lines. However, despite the low defect density, the grain size is still relatively short: there are long PS cylinders, but they curve often. For SM3, the longest cylindrical grain occurs for the film with 25 nm. As with SM2 with 15 nm, the low defect density gives a false sense that there is a large grain size. However, that is not the case. The grain sizes are still short, which is due to the limited mobility of high MW systems.

Despite the limited grain size, the incorporation of NPs into the supramolecular thin films allows the highest MW based supramolecule, SM 3, to form an ordered structure. However, there is little long-range order. Prior work has shown that changing the fraction of solvent present in the film during solvent annealing can increase the grain size considerably. For this to happen in the time scale of a few minutes, though, the viscosity of the solution and degree of entanglement will need to be low. Figure 6 shows SM 2 and SM 3 solvent annealed to different solvent fractions, f_s, defined as the fraction of solvent present in the film upon quenching the annealing process.

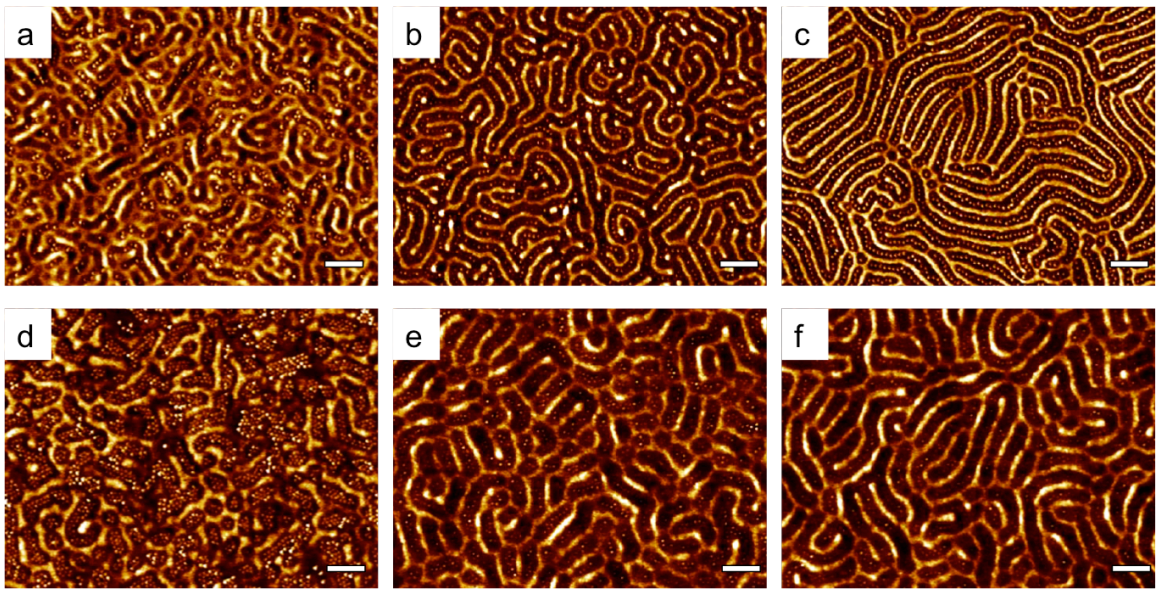

Figure 6: SM2 (a-c) and SM 3 (d-f) annealed to f_s=0.2 (a, d), 0.35 (b, e), and 0.5 (c, f). Films are ~180 nm thick with 3v% 15 nm iron oxide NPs. Scale bar=200 nm.

For SM2 (Figure 6a-c), the solvent annealing condition clearly affects the grain size. As the solvent fraction increases, the grain size grows from tens of nanometers to a few hundred nanometers. For SM3, however, solvent annealing has a limited effect on the grain size. The grain size does grow, but the largest grain size possible is on the order of tens of nanometers. For the larger MW nanocomposite, the mobility of the system is still low, despite the additional solvent. On the time scale of a few minutes, even with lowered viscosity from the addition of nanoparticles, the system cannot form long-range order.

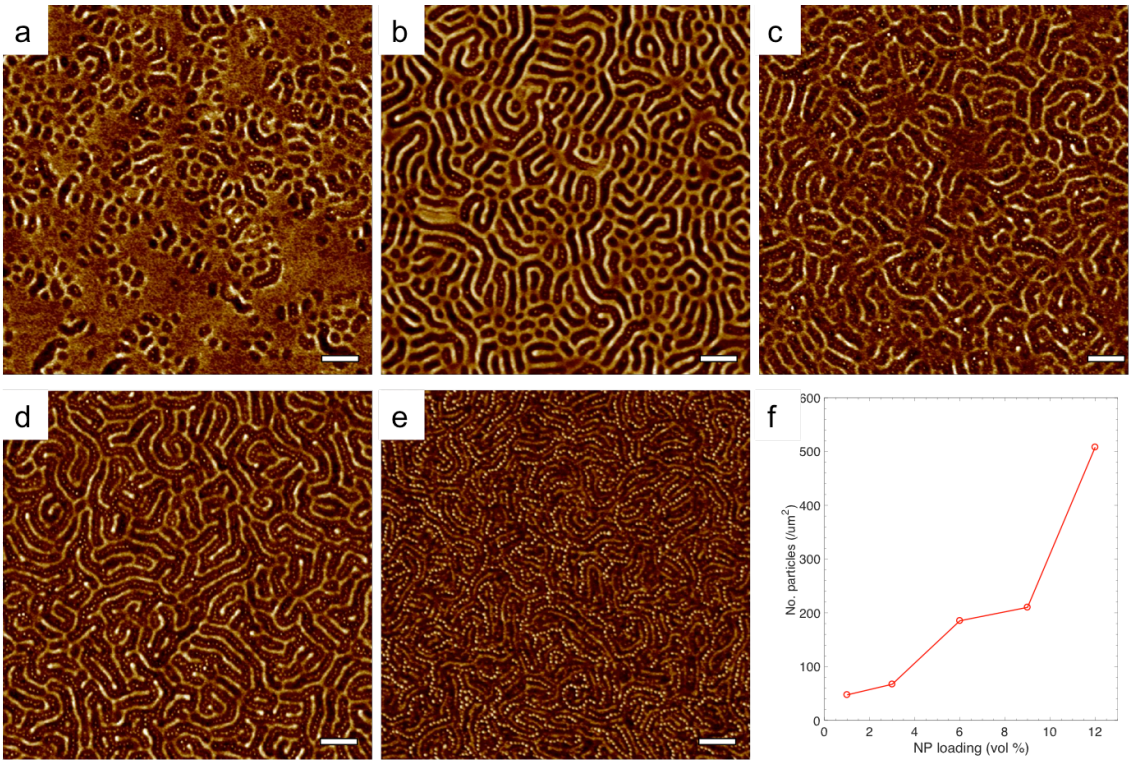

Figure 7: SM3 with 30 nm particles at (a) 1v%, (b) 3v%, (c) 6v%, (d) 9v%, and (e) 12 v%. (f) Number of NPs/area on the surface of a supramolecular thin film. Scale bar=200 nm.

While solvent annealing had a limited effect on the long-range order of the structure, increasing the NP loading has a greater effect (Figure 7). Here, the addition of solvent is not sufficient to improve the mobility under the time frame used to anneal the sample (>10 minutes). The NPs, however, can increase the mobility of the system by lowering the viscosity and reducing chain entanglement. As a result, the loading of particles acts as a handle to tune the long-range order of a high MW polymer. At low loading amounts, (1v%), the system lacks long-range order due to slow diffusion of the supramolecule (Figure 7a). As the volume loading

is increased up to 12v%, the grain size grows (Figure 7e). This growth in grain size is attributed to greater mobility of the supramolecule as well as the NPs. The number of NPs on the surface significantly increases as the particle loading changes (Figure 7f). The trend is not linear, which would be expected if the increased number of particles on the surface was only due to the increased number of particles in the system overall. Instead, there is a significant jump in particles on the surface between 9v% and 12v%, which also corresponds to a growth in the grain size. More particles are able to reach the surface due to a lower viscosity of the matrix, which also allows the nanocomposite to form longer grain sizes.

The increase of particle loading has a different effect when the starting morphology is honeycomb, not cylinders. The particle loading was increased from 3-9v% in SM1, 2, and 3 with NPs selected such that the d/l ratio for all three supramolecules was ~0.27 (Figure 8). This d/l should yield a honeycomb structure for all three morphologies at 3v% loading, although only a partial honeycomb is observed for SM3. As the particle loading increases, the honeycomb structure lessens and the system switches back to a cylindrical structure. The increase in NPs gives the system sufficient mobility to form the equilibrium cylindrical structure by lowering the viscosity of the supramolecule matrix. The honeycomb structure is a kinetically determined state, so once the mobility of the supramolecule increases, it reverts to the equilibrium cylindrical structure. This is also a deviation from what has previously been reported in supramolecule systems: large particles can form cylindrical structures, albeit ones with relatively short grain sizes. This is important for being able to tune the interparticle distance. In the honeycomb morphology, the

interparticle distance is necessarily far, since each particle is separated by a PS domain. In the cylindrical morphology, there can be quite close interparticle distance, on the order of the NP diameter. It is worth noting that for all these structures, with d/L of ~0.28, the particles pack in a single row.

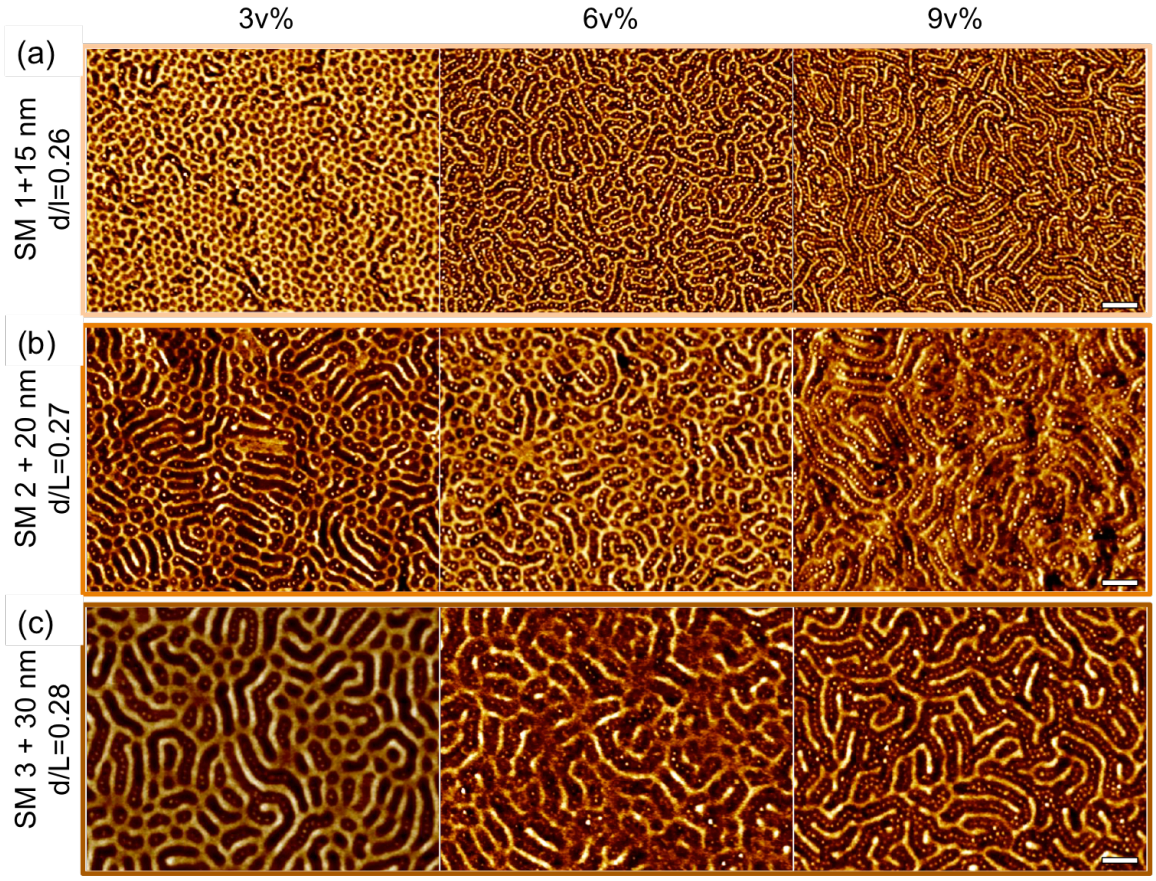

Figure 8: Increasing the volume loading of NPs for structures with a d/l ratio of around 0.27 (a) SM1 with 15 nm NPs (b) SM 2 with 20 nm NPs and (c) SM 3 with 30 nm NPs.

The effect of particle loading was also explored for a purely cylindrical forming system. Here, SM2 with 15 nm particles was selected (Figure 9). The AFM

phase images show that the system forms a cylindrical morphology when the particle loading is 3v%, 6v%, and 9v% (Figure 9a-c). The long-range order of the films and particle packing, however, changes as the particle loading increases. When the loading is 3v% and 6v%, the particle pack in a single row. For 9v%, the particles begin to form zigzags or multiple rows. There are more particles on the surface, which forces a change in the particle packing. This is also shown in the periodicity, which increases from 65 nm to 69 nm as the particle loading increases from 3v% to 9v%. The grain size of the 9v% films is also larger.

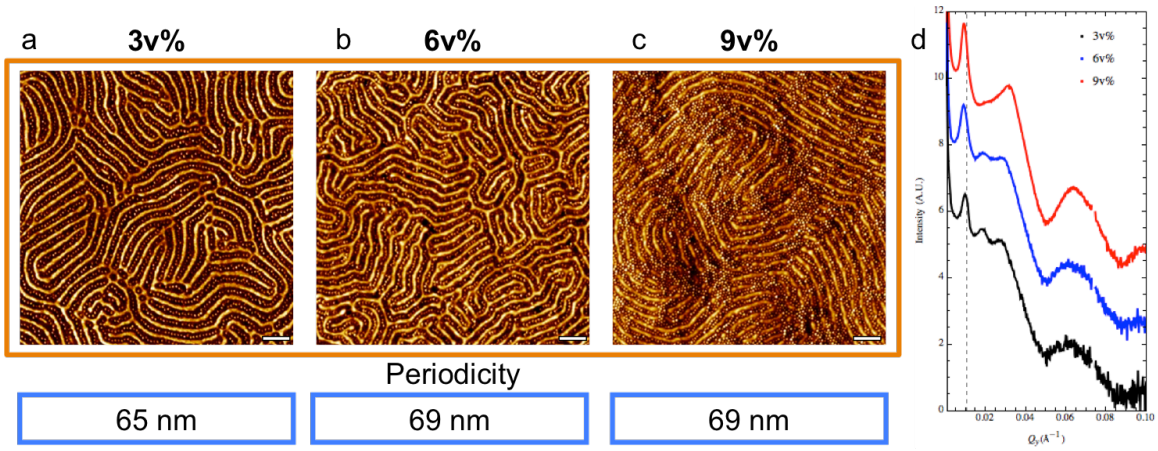

Figure 9: SM 2 with 15 nm particles at (a) 3v%, (b) 6v%, and (c) 9v%. (d) Horizontal GISAXS linecut profiles.

4.4 Discussion

Adding NPs to a high MW supramolecule allows the system to form an ordered structure on a short time scale. This is done by lowering the viscosity of the polymer matrix, allowing for greater mobility. Prior research shows that adding nanoparticles to a polymer solution can either decrease solution's viscosity if the

size of the NP is small relative to the polymer[45]. For entangled systems, particles are defined as small if they are less than approximately ten times the size of the polymer tube diameter. The particles decrease the viscosity by diluting entanglements and improving chain mobility.

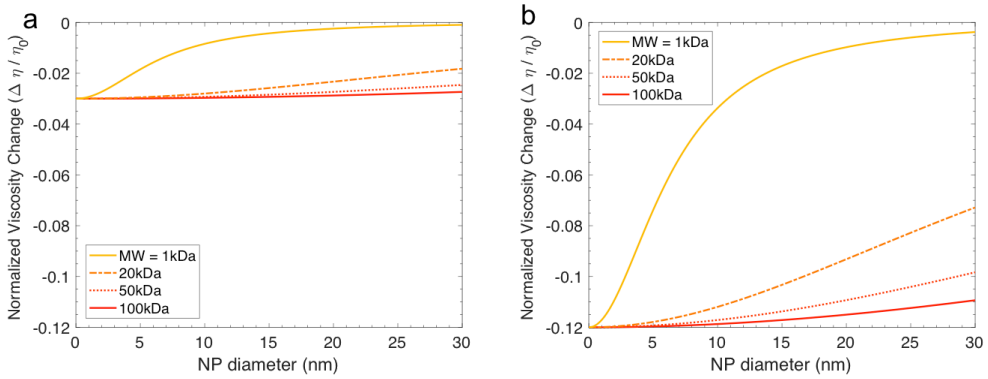

Figure 10: Plot of normalized viscosity for a polystyrene polymer with the addition of NPs up to 30 nm for four different MW showing that the addition of NPs lowers the viscosity of the polymer for (a) 3v% loading and (b) 12v% loading

The effect of NPs on polymer matrix viscosity has been modeled in homopolymers. The net change in viscosity Δη, normalized by the viscosity without nanoparticles η_0, is written

$$\frac{\Delta\eta}{\eta_0} = \frac{3-96\lambda\beta^2}{2(1+5\lambda+48\lambda\beta^2)}\phi$$

where the parameter β is the ratio of relevant sizes, Rg/R, for polymer radius of gyration Rg and nanoparticle radius R; φ is the particle volume fraction[46]. The parameter λ describes slip between the nanoparticle and the polymer. This value depends on the polymer and nanoparticle being used, and is difficult to estimate. Here, an intermediate value of 2.5*N is used, where N is the number of polymer

segments. The PS-P4VP(PDP) supramolecular system is approximated as PS homopolymer in a good solvent, and this relationship is plotted for a range of molecular weights (Figure 10a). While this is an approximation, it should at least describe the behavior of the supramolecule system. Due to the coil-comb architecture, the PS component will be entangled, while the P4VP(PDP) block should have fewer entanglements. The free PDP will act as a selective solvent for the P4VP block that can additionally lower viscosity, so the PS block should be the determining factor in the mobility of the system. It is worth noting that, because of the preferential interaction of the NP ligand with the small molecule, the NPs will mainly be located in the P4VP(PDP) domain, which likely has few entanglements due to the brush structure from the small molecule. The PS domain will have more entanglements due to its higher MW and coil formation. While the NPs may not be primarily located in the PS domain, they still will cross into it due to the needed interdomain crossing for the formation of an ordered structure. As such, it is expected the NPs will still lower the viscosity.

Figure 10a shows the relative viscosity of four different MW PS polymers with 3v% particle loading from 0-30 nm. As can be seen, for 20k, 50k, and 100k polymers, which correspond to SM 0, SM1/2, and SM 3, respectively, NPs at all sizes still lower the viscosity of the system. If the polymer used were instead 1kg/mol, adding NPs would not significantly affect the viscosity. Small particles lower the viscosity by more than larger particles. Increasing the particle loading to 12 v% (Figure 10b) shows that having more particles will decrease the viscosity of the polymer matrix as well. This is important especially for the highest MW

supramolecule. The balance created by increasing the mobility of all the components and the governing thermodynamics changes the energy landscape during self-assembly. The changing landscape is complex and relies on many parameters, but controlling it offers the opportunity to design thin films without size constraint.

4.5 Conclusion

The addition of NPs to high MW-based supramolecules allows for the formation of ordered structures that are highly tunable in less than 10 minutes by modulating the kinetics of assembly. The tunability comes form the ability to control the pathway during assembly by using the inherent parameters. NP size, NP loading, solvent annealing condition, and MW were all found to be handles that could be used to create thin films with specific feature sizes, morphologies, and interparticle distances. Feature sizes ranging from 55-105 nm in cylindrical and a honeycomb morphology has been achieved. The particle loading and particle size can be changed to select a specific morphology, although the pathway depends on the MW. The supramolecule allows for a much greater range in periodicity and NP sizes that can be incorporated than traditional BCP systems. This work begins to create a roadmap for making exactly tunable nanocomposite thin films in feature size and structure by modulating the kinetics during assembly.

4.6 Methods

Materials

PS(47 kDa)-*b*-P4VP(10 kDa) (PDI = 1.10), PS(50 kDa)-*b*-P4VP(17 kDa) (PDI = 1.15), and PS(104 kDa)-*b*-P4VP(30 kDa) (PDI = 1.07) were purchased from Polymer Source, Inc. 3-*n*-Pentadecylphenol (90%–95%) was purchased from ACROS Organics. Chloroform (Amylene as preservative) was purchased from Fisher Scientific. Iron oxide NPs dispersed in chloroform were purchased from Ocean Nanotech. All chemicals and materials were used as received.

Sample Preparation

Supramolecular solutions were prepared by dissolving the polymer and the small molecule in chloroform and then stirring for 72 h. Thin films were prepared by spin-coating the mixed solutions onto silicon wafers at 3000 rpm. Sample thicknesses were measured using a Filmetrics F20 interferometer. For solvent annealing, samples were annealed using 300 µL of $CHCl_3$ injected inside a 250 mL top-capped jar at 24°C. Once the film thickness of the nanocomposite thin film reached the desired thickness, the jar was opened and the $CHCl_3$ vapor inside the jar was allowed to freely evaporate. Solvent fraction is the volume fraction present in the swollen film during annealing, calculated as $f_s=\frac{t_f-t_i}{t_f}$ where t_f is the final film thickness and t_i is the initial film thickness. The solvent annealing process was stopped at the desired f_s and the sample was quenched within 10 seconds. Bulk samples were obtained by evaporating solvent from the solution mixtures in Teflon beakers and drying in a vacuum oven at room temperature, followed by thermal annealing at 100 °C for 8 h.

Transmission Electron Microscopy (TEM)

TEM imaging was performed on a FEI Tecnai 12 TEM at an accelerating voltage of 120 kV. Bulk samples were embedded in epoxy resin (Araldite 502, Electron Microscopy Sciences) and cured at 60 °C overnight. Thin film samples were floated off the Si substrates by dipping into 5% HF aqueous solution. The floated film was picked up by an epoxy block and left at room temperature overnight to ensure the adhesion of the thin film to the epoxy. The samples were then sectioned using an RMC MT-X Ultramicrotome (Boeckeler Instruments) with a section thickness of 60 nm. The thin sections were then caught on a 200-mesh carbon film-coated copper grid for TEM imaging.

Atomic Force Microscopy (AFM)

AFM was performed on a Bruker Dimension Edge. The spring constant of the cantilever was 5–10 N/m with a resonant frequency in the range 90–210 kHz. The set point for the auto tune was ~6.0 V. The set point amplitude was 80–90% of the free vibration value.

Image Analysis

Image analysis was performed in Python using methods inspired by the *ADAblock* application[47]. The periodicity of the supramolecule determined from the fast Fourier transform (FFT). For defect analysis, AFM phase images were binarized using a local thresholding technique. NPs were deleted by filtering out small elements. The images were then skeletonized. Defects were found by scanning each pixel: a pixel with two nearest neighbors was considered defect-free, a pixel with only one

nearest neighbor was labelled an end, and a skeleton pixel with three or more nearest neighbors was labelled a junction. This analysis was done for both the PS and P4VP(PDP) phase. The defects/μm^2 quantity shown in Figure 4(c) was calculated as $(PS_E + PS_J)/2 + (P4VP_E + P4VP_J)/2$, where E and J denote ends and junctions, respectively, as has been previously reported[47].

Grazing Small-Angle X-Ray Scattering (GISAXS)

GISAXS experimental measurements were made at beamline 7.3.3 at the ALS in the Lawrence Berkeley National Laboratory and at beamline 8-ID-E the APS in the Argonne National Laboratory. X-ray wavelengths of 1.687 and 1.240 Å were used at APS and ALS, respectively. The scattering intensity distribution was captured by a Pilatus 1M detector at ALS and APS at an incident angle of 0.13°. The intensities (I) are plotted with respect to q, where $q = (4\pi/\lambda)\sin(\theta/2)$, λ is the wavelength of the incident X-ray beam, and θ is the scattering angle.

Chapter 5
Probing the Self-Assembly Process of a Supramolecular Nanocomposite Thin Film Using *In Situ* Grazing-Incidence Transmission Small Angle X-Ray Scattering

5.1 Introduction

Solution-based processing is a promising method for creating self-assembled thin films with specific structure and desired functionality. These techniques, which include inkjet printing, 3D printing, dip-coating, blade-coating, spray-coating, controlled drying, and more, have been studied extensively and applied to a variety of applications[1-10]. However, even with widespread adoption of solution-based processing, there is still a lack of knowledge about the pathway taken during assembly. While the system design and the final structure have been correlated, the ultimate structure depends on the assembly pathway and the balance of several competing processes. In order to create and access new structures and properties, the kinetic pathway of assembly must be understood in thin films[11, 12]. For bulk solution self-assembly, *in situ* transmission scattering using small angle X-ray scattering (SAXS) has been commonly used as a technique to understand the assembly pathway[13, 14]. The nucleation and growth of structure has been carefully tracked to understand what forces during the assembly process result in the final sample features, leading to samples that can be tailored.

In thin films, scattering studies can be performed *in situ* to understand the pathway of block copolymer assembly under solvent annealing and drying[15-20]. SAXS has been used to probe polymer thin films, however, it is limited due to the small sample volume[21, 22]. The most commonly used technique is grazing-incidence small-angle X-ray scattering (GISAXS). GISAXS is a surface-sensitive technique, so only the air-sample interface can be carefully studied. The interior of the film and the substrate-sample interface are difficult to probe with GISAXS, thus the ensemble

behavior of a thin film during assembly remains unknown. Grazing-incidence transmission small angle X-ray scattering (GTSAXS) is a relatively new technique that can be used to probe both interfaces as well as the interior of the film[23, 24]. GTSAXS has been used to probe a few model systems, but has yet to be widely adopted a technique. Here, GTSAXS is used to monitor the self-assembly of a multicomponent system *in situ* during controlled drying of a thin film.

The system used here is a block copolymer (BCP)-based supramolecular nanocomposite. This system has been extensively studied in bulk and thin films with a variety of different types of nanoparticles (NP)[25-27]. In thin films, a variety of morphologies can be achieved with long-range order by tuning the NP size, NP loading, and NP type[13, 25, 28-31]. These assemblies have been largely generated via solvent vapor annealing. The kinetic pathway of these assemblies shows a strong dependence on the solvent annealing condition[12, 32]. It is an open question, however, if solvent vapor annealing follows the same kinetic pathway as a controlled drying process. The supramolecular nanocomposite is also advantageous to use in an *in situ* GTSAXS study due to the large scattering contrast between the NPs and supramolecule. One of the limitations of GTSAXS is the need for a strongly scattering sample due to the pathway of the beam through the sample as well as the substrate, which results in attenuation of the signal. The supramolecular nanocomposite here has strong scattering, making it an ideal candidate to study using GTSAXS.

Here, a supramolecular nanocomposite was investigated using *in situ* GTSAXS during controlled drying to understand the assembly pathway of a supramolecular nanocomposite. GTAXS proved to be an effective technique for

probing these films to understand the pathway during. It was found that there are three stages during the drying process. By probing the system *in situ*, the kinetic pathway of a solution-processed thin film is better understood, creating a map for how highly ordered structures can be achieved.

5.2. Comparison of Grazing-Incidence Transmission Small Angle X-Ray Scattering and Grazing-Incidence Small Angle X-Ray Scattering

The supramolecular nanocomposite used here was polystyrene-*b*-poly(4-vinylpyridine)(pentadecylphenol) (PS-P4VP(PDP)) with 5 nm iron oxide nanoparticles. Drop-cast films were monitored *in situ* using GTSAXS. At several points during the drying process, the incident angle was lowered so that GISAXS profiles were taken to compare with the higher incident angle GTSAXS profiles.

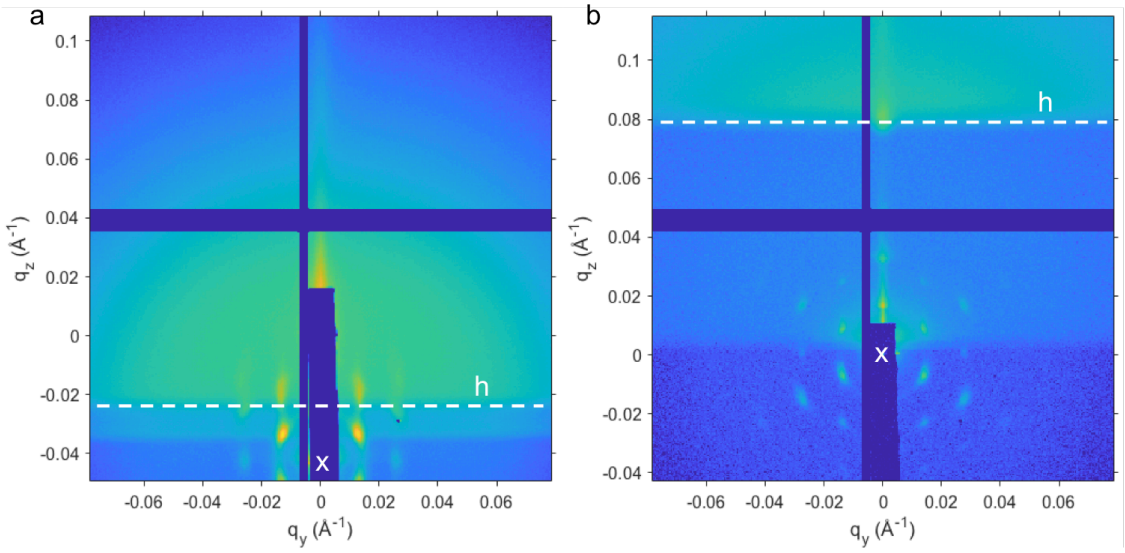

Figure 1: (a) GISAXS profile versus (b) GTSAXS profile during drying. Dotted like labeled h indicates the horizon, x is the beam center.

Figure 1 shows scattering profiles of two during drying using GISAXS with an incident angle of α=0.14˚ (Figure 1a) and GTSAXS with an incident angle of α=0.8˚ (Figure 1b). Both samples were taken after drying for ~50 minutes under the same conditions. Peaks can be distinguished on the GISAXS profile, but appear as vertical streaks, commonly referred to as Bragg Rods. In the GTSAXS profile, the Bragg Rods can be resolved into individual peaks. Additionally, the horizon is at a higher q_z value in the GTSAXS profile due to a higher incident angle so it does not interfere with the region of interest. The GISAXS profile shows some transmission features, centered on the incident beam. However, they are difficult to exactly resolve and all transmission features are not present due to the limited range in negative q_z. The GTSAXS profile clearly displays these negative q_z features. The clearer features in GTSAXS makes it a better technique to investigate during *in situ* drying. More importantly, GTSAXS samples the entire film, not just the surface, so information about the interior of the film and the substrate-sample interface is available.

5.3 Stages of Drying

Using GTSAXS, the supramolecular nanocomposite thin films were monitored every 2-3 minutes during the initial stages of the drying process. Filmetrics was also used to monitor the samples *in situ* to attempt to quantify the solvent content in the film at each stage. Figure 2 shows select GTSAXS profiles and Filmetrics during stage I of the drying process, the initial formation of an ordered structure. At early times, the incident angle was set to α=0.5˚ due to a weak scattering signal as the structure begins to order.

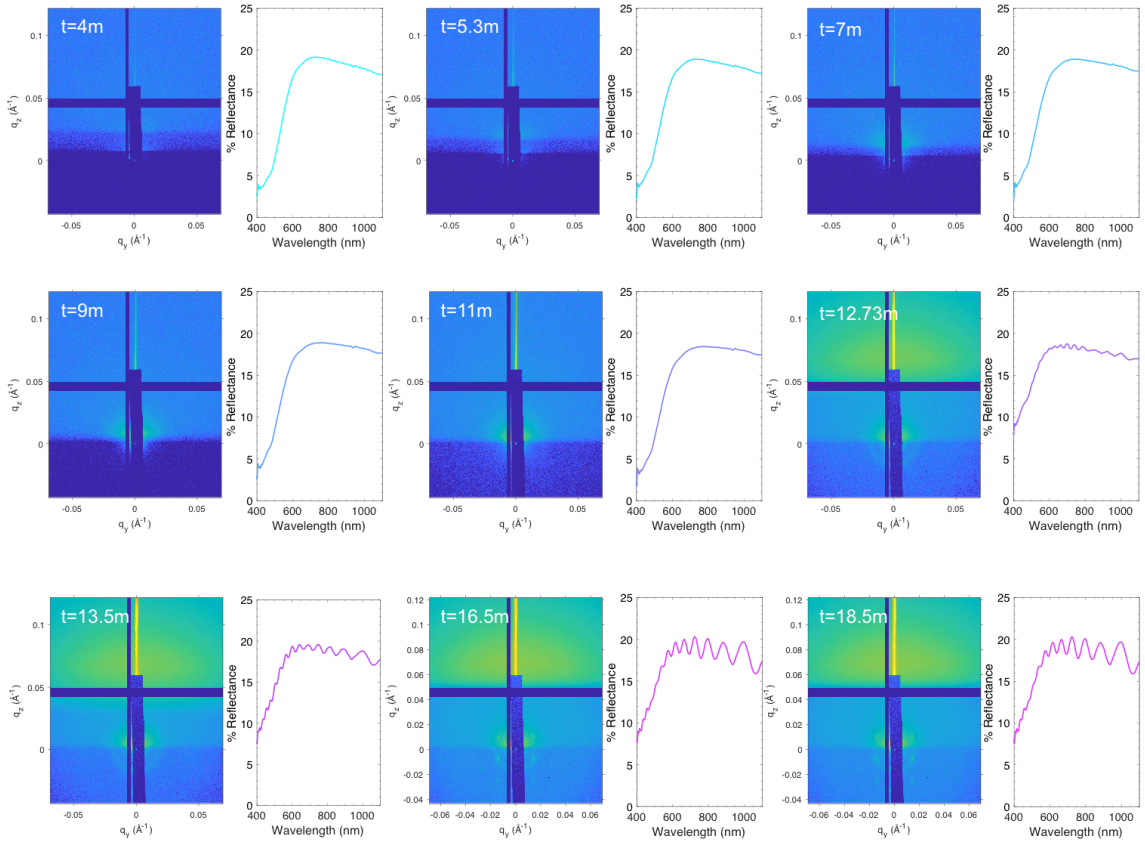

Figure 2: GTSAXS (incident angle α=0.5˚) and Filmetrics profiles of a supramolecular nanocomposite at the early stages of drying, during stage I of the drying process. Time each profile was taken is in the upper left hand corner of the GTSAXS profile.

Initially, there are no clear features in the GTSAXS profiles. At around 12-13 minutes after drying has started, a ring appears in the scattering profile. After the formation of the ring, clear peaks emerge in the scattering profiles quickly. These peaks indicate a hexagonally packed structure. Second order peaks appear within minutes of the appearance of defined peaks, which indicates a highly ordered structure. The system goes from a quasi-disordered structure to a highly ordered structure in a matter of minutes.

The changes in the scattering profile are accompanied by changes in the Filmetrics profile. Initially, the Filmetrics profile shows a smooth curve. When a ring appears in the GTSAXS profile, the Filmetrics profile begins showing oscillations. As the scattering peaks get clearer in the GTSAXS profile, the amplitude of the oscillations increases and the frequency of oscillations decreases. The Filmetrics measurements are based on interference spectroscopy, so the oscillations can be fit to determine a film thickness[33]. This fit is based on the index of refraction of the solution and the roughness of the film, both of which are difficult to calculate in a multicomponent liquid. Due to the multiple components, the solution is not homogenous. Thus, the solution will have a different index of refraction at different points. The multiple components constitute multiple interfaces for light to reflect off, creating complex interferences. As such, a satisfactory fit of the data was unable to be calculated. A rough fit was calculated for the Filmetrics profile at t=18.5m to approximate the solvent fraction when clear peaks emerge in the GTSAXS profiles (SI Figure 2). Based on the fit, the film should be ~2900 nm. The final film thickness, based on a scratch test, is ~800 nm, so that the solvent content of the film, denoted f_s, is $f_s \approx 0.72$. While this is a rough value, it does indicate that there is a high solvent content when a highly ordered structure forms. Figure 3c shows pictures taken on identical films *ex situ*. These films were also monitored using Filmetrics. It is clear from these pictures there is still high solvent content. The picture on the left was taken after the oscillations appeared in the Filmetrics data. The edges of the film have dried somewhat, making them look brown and matte, but the interior of the film is reflective because it is still liquid-like. The picture on the right was taken after

the drying process was complete and the Filmetrics data no longer had oscillations. There is little if any solvent still in the film and the whole film has become brown. There is still high solvent content when the film forms an ordered structure, during stage I of drying, supporting the rough calculation of f_s=0.72 as the solvent content when peaks appear in the GTSAXS data.

Before the formation of a ring, the scattering pattern suggests the system is beginning to form an ordered structure (Figure 3). The sector integration of the GTSAXS data at early times during the drying process shows the formation of a characteristic correlation wavelength. As the drying process continues, the shape of the integration cut changes from flat to having a clearly defined decaying peak, likely a result of the formation of a correlation hole. The intensity of the peaks also change during the drying process (Figure 3b), which could indicate a characteristic correlation wavelength, but is could also be attributed to the attenuation of the beam. During drying, the film thickness will decrease as solvent evaporates, resulting in a shorter pathway of the beam through the sample. However, the distance the beam travels through the sample is on the order of tens of microns, is much smaller than the distance the beam travels through the underlying silicon substrate, tens of millimeters, suggesting beam attenuation through the film is negligible as compared to attenuation through the substrate.

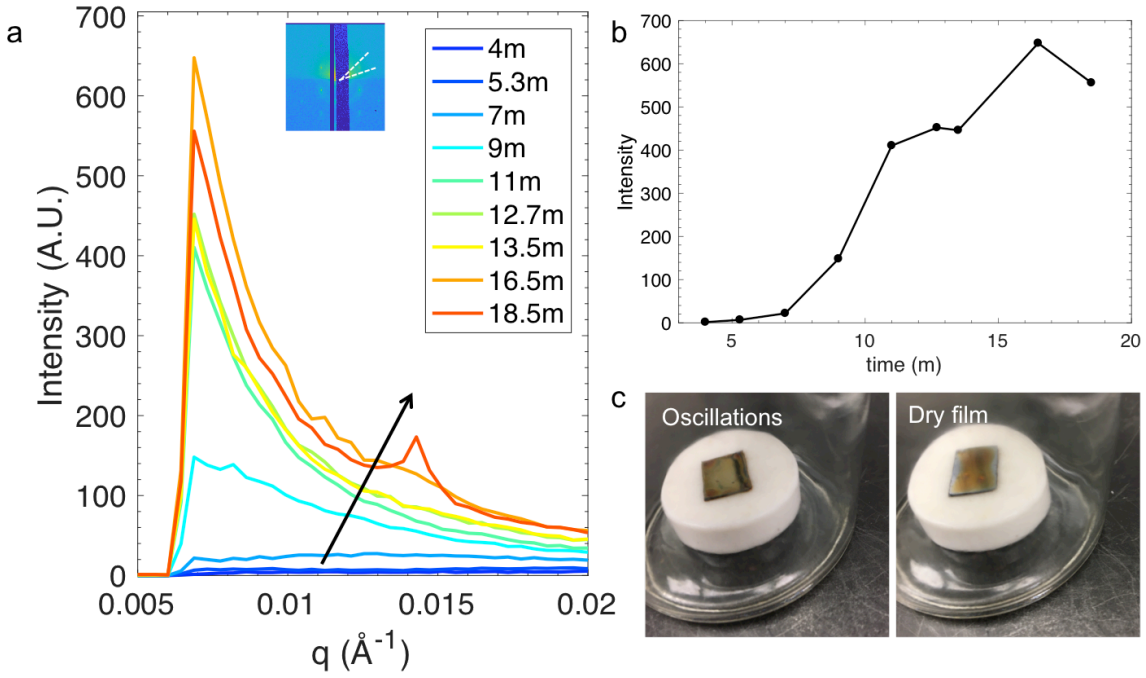

Figure 3: (a) Sector integration of GTSAXS profiles during the initial stages of assembly process. Inset shows the sector integrated. (b) Intensity of sector integration from (a) at q=0.07Å^{-1} as a function of time. (c) Picture of a sample during drying process. The picture on the left was taken after the oscillations appeared in the Filmetrics data, and the right picture was taken after the drying process was complete.

During stage II of the drying process, the system remains in a highly ordered state (Figure 4). Once an ordered structure was formed, the incident angle was set to α=0.8° to minimize distortion of the scattering features. Additionally, at α=0.8°, the direct beam intensity is low enough that the beamstop can be lowered so that more scattering peaks are observed. The sharp peaks present in the GTSAXS images indicate that there is one periodicity throughout the sample: ordering happens simultaneously throughout the entire film. Both interfaces drive the formation of a highly organized structure. This almost crystalline structure persists during the

drying process for approximately half of the drying time, while higher order peaks appear, indicating the formation of long-range order.

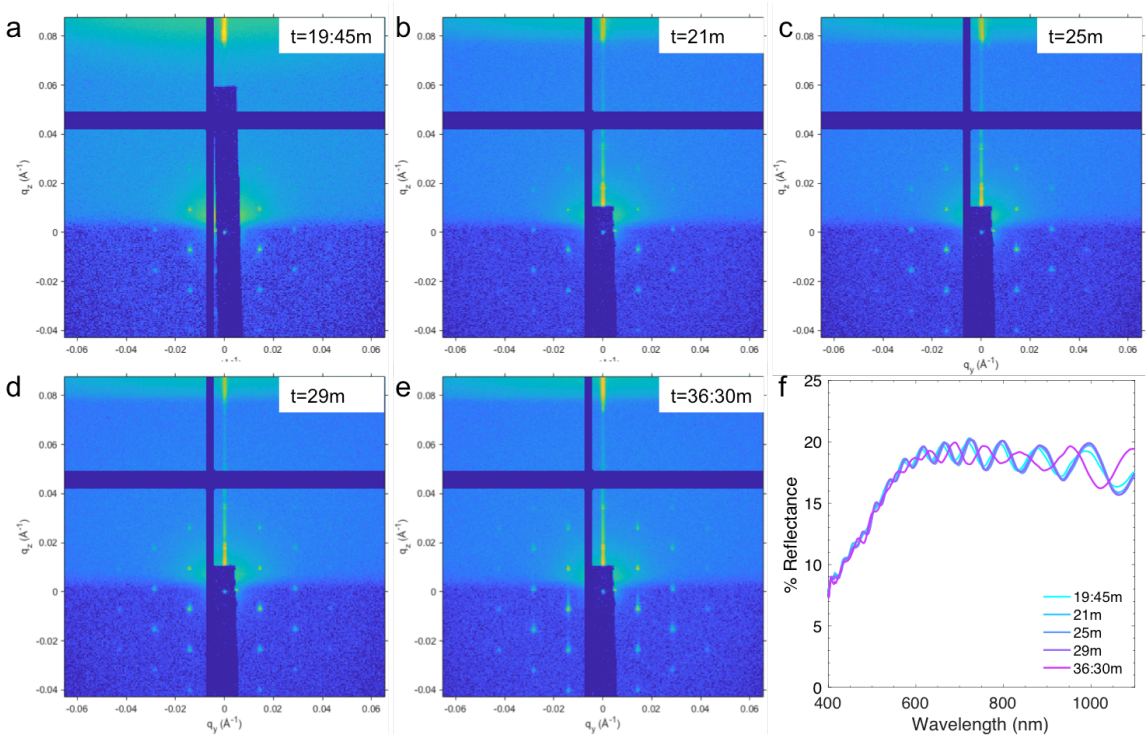

Figure 4: (a-e) GTSAXS profile (α=0.8°) and Filmetrics profiles of a supramolecular nanocomposite during stage II of the drying process. The time each profile was taken is in the upper right hand corner of GTSAXS profile. (f) Filmetrics data taken at corresponding times to GTSAXS profiles.

During this stage drying process, the oscillation Filmetrics data mirrors the peaks (Figure 4f). The oscillation in this data appears simultaneously to the appearance of peaks in the GTSAXS data. The earliest oscillations in the Filmetrics data are offset slightly in phase from the oscillations that appear for most of stage II. When the film is ordering, the oscillations are in a different phase than when the film has formed a highly ordered structure. During this middle part of stage II, from 20-30 minutes into the drying process, the peaks in the GTSAXS profiles are clear

and higher order peaks appear while the oscillations in the Filmetrics data are the same in phase and amplitude. Once the GTSAXS peaks begin to broaden (Figure 4e), the phase of the oscillations shifts and the amplitude decreases slightly. Even if the Filmetrics data cannot be fit to give an exact film thickness, it can be used to monitor where the film is during the drying process. Stage II of the drying process is characterized by the film adjusting slightly within the initial templated structure. The appearance of second and third order scattering peaks suggests the long-range order is growing due to long-range diffusion.

In stage III of the drying process, the sharps peaks in the GTSAXS data broaden (Figure 5). As the peaks broaden, the oscillations in the Filmetrics data begin to disappear. These oscillations change in amplitude as well as frequency as the peaks broaden. Generally, the frequency of the oscillations is proportional to the film thickness, so as the frequency decreases, the film is getting thinner. This trend is to be expected as the solvent evaporates from the film. As the peaks broaden, however, there are still clear higher order peaks present in the GTSAXS data, indicating there is still good long-range order. In this stage, short-range diffusion guides the assembly. The overall structure of the film is set in a template from stage I. From that template, the system can only undergo local rearrangement, leading to the broadening peaks as the periodicity changes in the film.

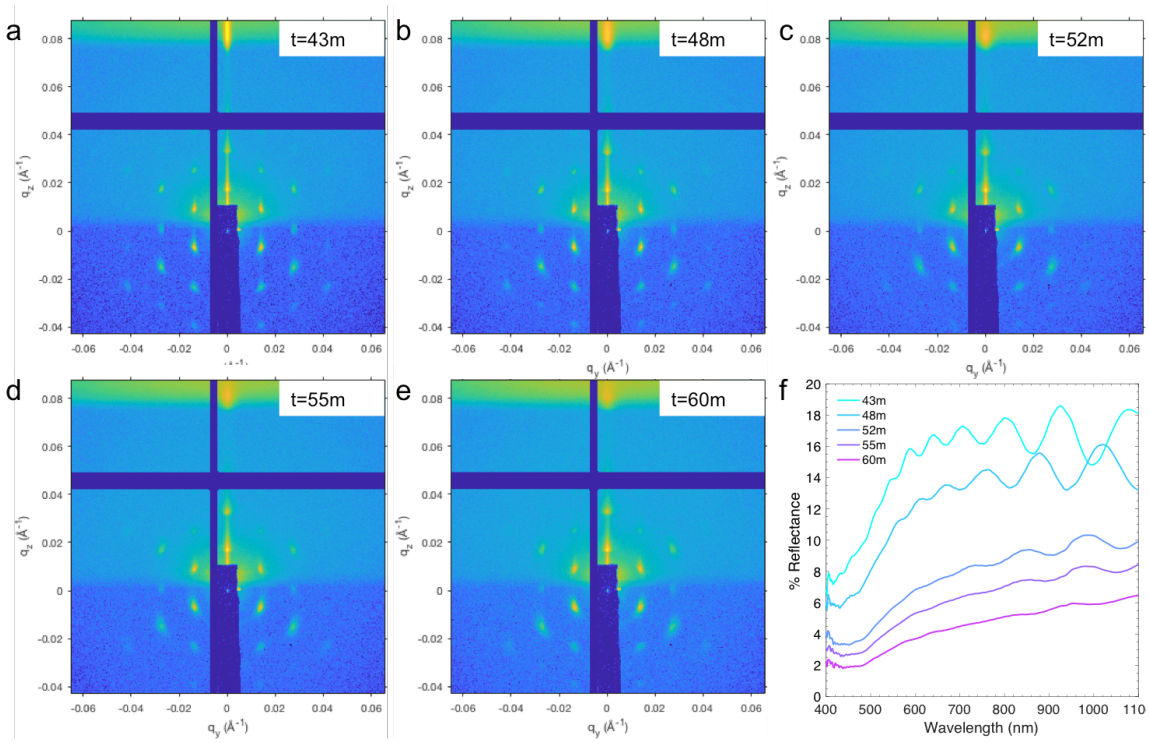

Figure 5: (a-e) GTSAXS profile (α=0.8°) and Filmetrics profiles of a supramolecular nanocomposite during stage III of the drying process. The time each profile was taken is in the upper right hand corner of GTSAXS profile. (f) Filmetrics data taken at corresponding times to GTSAXS profiles.

Peak position and full width at half maximum (FWHM) was calculated from the radial integration of each plot to quantify how the domain spacing and long-range order change during the drying process (Figure 6). The position and FWHM the second order peak was used to avoid distortion of the first order peak from background scattering. The radial integration profiles are shown in Figure 6a. At all times after the formation of an ordered structure, higher order peaks are observed, indicating good long range order in the film. These profiles also show a small change in the position of the peaks during the drying process as well as a broadening of the

peaks. The peak position in as function of time is shown in Figure 6b. During the drying process, the location of the peak forms a u-shaped pattern.

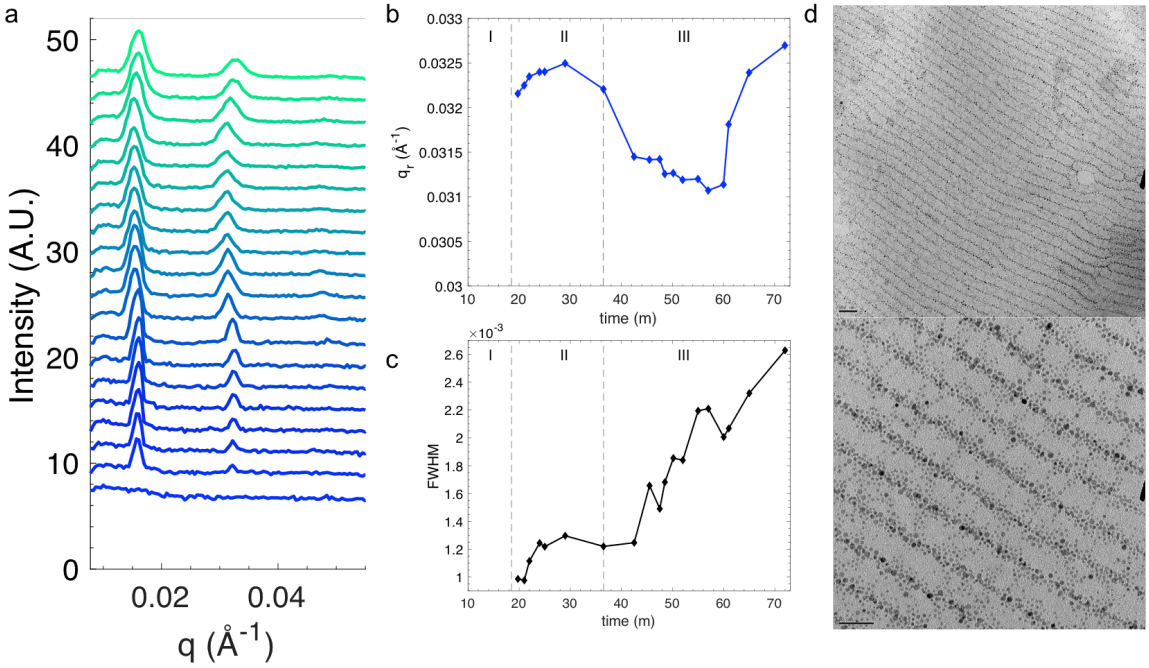

Figure 6: (a) Radial integration of GTSAXS profiles. Second order peak (b) position and (c) full width at half maximum as a function of drying time. (d) TEM of ~100 nm nanocomposite films at two magnifications.

At short drying times during stage II, t=20-30 minutes, the peak position increases, indicating a reduction in the periodicity of the film. From t=30-40 minutes, the peak position decreases sharply/the periodicity increases. The peak position continues to decrease from t=40-60 minutes, during stage III of the drying process, although more gradually. After t=60 minutes, the peak position increases sharply to a larger value than the initial peak position, indicating a smaller periodicity than was present at the beginning of the drying process. The change in the peak position from the beginning of the drying process to the end follows the

expected increase in peak position/decrease in periodicity as solvent evaporates. Without the *in situ* experiment, the additional information about the pathway taken would be unknown. The overall change in peak position is small, corresponding to a range of a few nm. Once the periodicity of the film forms, there are only small changes. This suggests templated assembly: an ordered structure is formed quickly during the drying process. Once that structure has been formed, the system is unable to rearrange significantly and can only undergo short-range diffusion.

The FWHM of the second order peak is shown in Figure 6b. Overall, the peaks get broader as the drying process continues. The FWHM does not appear to have the same characteristic regions as the peak position. However, there are changes in the FWHM curve that occur at the same time points as the changes in the peak position. Initially, the FWHM increases. During the sharp drop-off in peak position at t=30-40m, the FWHM plateaus. The system undergoes a slight rearrangement in spacing without while maintaining a similar grain size. From t=40-60 minutes, the FWHM increases again as the peak position changes more gradually. Here, there is decrease in long-range order with a corresponding smaller change in nanocomposite periodicity. The FWHM continues increasing, although there is a slight decrease when the peak position begins decreasing again**.** The increase of the FWHM during the drying process points to templated assembly. Although the system forms an ordered structure quickly, it still has mobility. But if there is an ordered framework, the system is limited to short-range diffusion, so it can only rearrange locally, which leads to a disordering of the system. Higher order peaks in the GTSAXS patterns

indicate there is still good long-range order in the system overall, so the broadening of peaks is coming from local disorder rather than the entire system disordering.

Transmission electron microscopy (TEM) images of a 100 nm nanocomposite film that was prepared using the same conditions are shown in Figure 6d. The top image shows clearly that there is long-range order in the film after the drying process is finished. This observation is consistent with the higher order peaks in the GTSAXS data. The bottom image provides a possible explanation for the broadening of the peaks. From the top image, it appears that the NPs are segregated into one domain of the supramolecule. However, at a higher magnification, the TEM image shows that there are NPs in both domains. The fact that NPs are in the PS domain indicates that, during the drying process, the small molecule likely becomes soluble in both domains. The scattering signal comes from the NPs, so having particles in both domains will broaden the peaks because there is a lack of order locally even if there is long-range order in the film overall.

The distance between peaks in both q_y and q_z gives additional information about how nanocomposite lattice changes during the drying process (Figure 7). For both Δq_y and Δq_z, the changes are small, corresponding to a few nanometers, suggesting that any rearrangement of the nanocomposite is limited by the initial arrangement. They follow the same general trend, albeit with different inflection points. Initially, there is no change in spacing in either direction. Then, there is an increase in q spacing, corresponding to a decrease in lattice spacing, followed by a decrease in in q spacing. In the q_y direction, the increase in peak spacing persists for longer whereas the q_z peak spacing begins to decrease sooner.

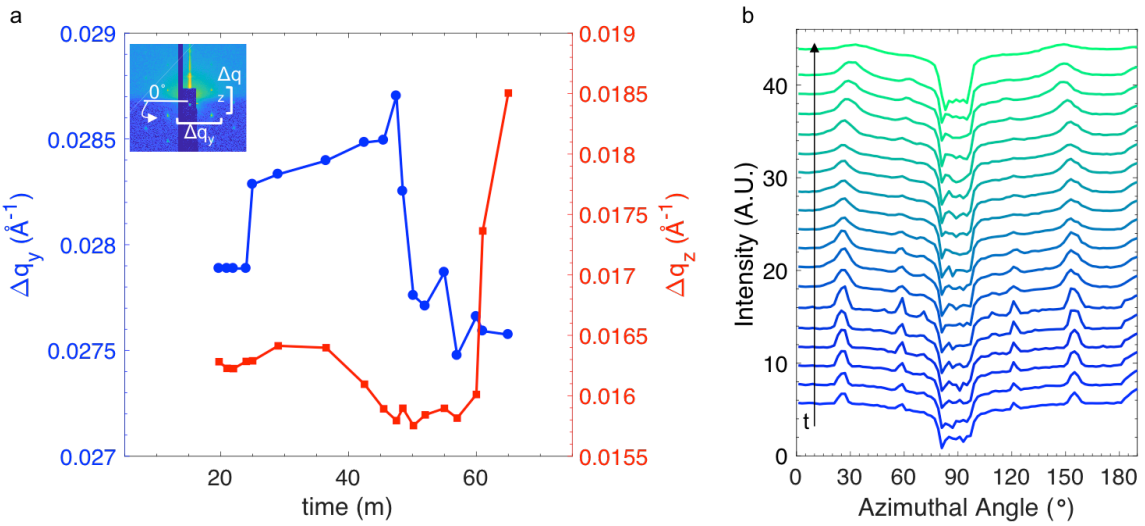

Figure 7: (a) Distance between peaks in q_y (left axis) and q_z (right axis). Inset shows how the two distances were measured (b). Azimuthal integration at different drying times. The starting point and direction of integration is shown in the inset in (a). Fix (b)

The Δq_z has a large increase at t=60 minutes, when the chamber was vented, meaning solvent was removed quickly. As the solvent is removed, the film will collapse in the z-direction. There is no corresponding change in Δq_y during the fast removal of solvent, which is consistent with previous studies, where the system does not have time to rearrange and the spacing of the supramolecule is frozen in. The magnitude Δq_z and Δq_y is different, meaning that the lattice is not perfectly symmetric.

The azimuthal angle integration of the GTSAXS patterns is show in Figure 7b. The definition of where the integration starts and its direction is shown in the inset of figure 7a. The azimuthal integration data confirms that, once the system forms an ordered structure, there is little change in the lattice. At short drying times, there are clear, sharp peaks that lessen in intensity and broaden as the drying process

continues. There is little shift in the peak position as the drying process continues, indicating the lattice does not rearrange orientation, which is to be expected. The disappearance of some of the peaks, such as those at ~60˚ and ~120˚, is due to the loss of higher order peaks toward the end of the drying process.

5.4 Discussion

GTSAXS has been used to monitor films during *in situ* drying. It has shown to be effective for investigating the drying process due to the strong scattering from the NPs in the sample. The long-range order of the film occurs simultaneously to the formation of order, not as a gradual process. Controlled drying of a supramolecular nanocomposite is a three-step process (Figure 8).

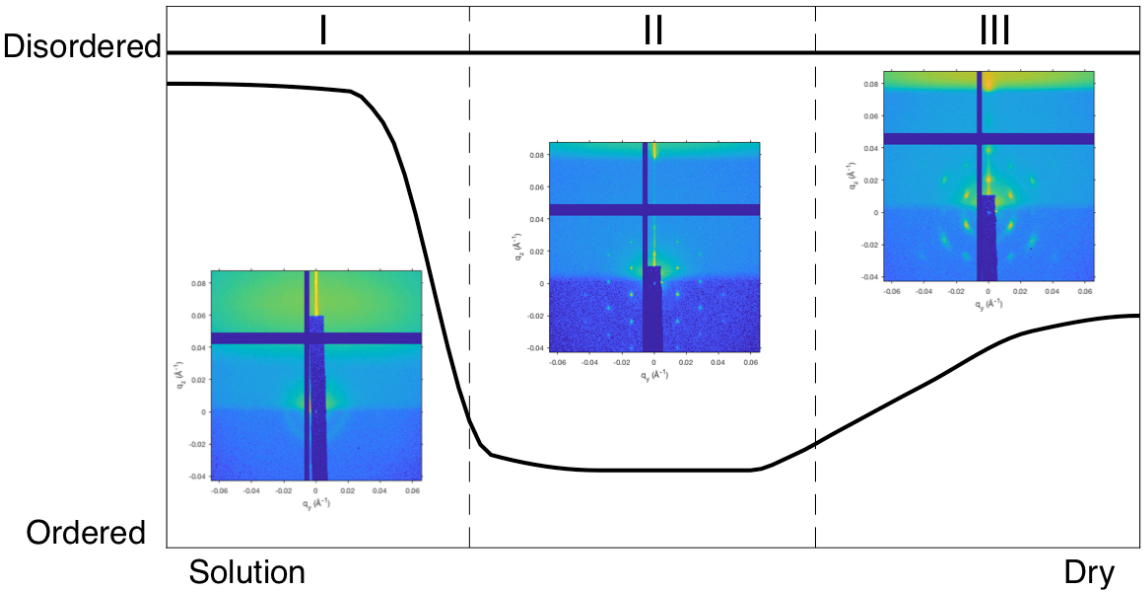

Figure 8: Schematic of stages of drying of supramolecular thin film nanocomposites

During stage I, the initial formation of order can be monitored by the scattering profile until the appearance of a ring in the GTSAXS pattern that is followed very quickly by sharp, almost crystalline. These peaks appear at short drying times, when the solvent content of the film is still high, estimated to be f_s=0.72. This observation seems counterintuitive, as a high solvent content should lead to a weak thermodynamic force for separation, since the Flory-Huggins interaction parameter decreases with increasing solvent[34]. However, the high solvent content means the system should have high mobility, leading to the formation of an ordered structure quickly.

In stage II, the highly ordered structure persists and grows, as indicated by the appearance of higher order peaks. The sharp peaks indicate that there is one periodicity throughout the entire film. The ordering of the film is not driven by the solvent gradient from the surface, but rather emanates from both interfaces throughout the film almost instantaneously. During this stage of the drying process, a highly ordered structure is maintained with little change in lateral periodicity throughout the film. Long-range diffusion governs this period of the drying process where film grain sizes increase and the system overall rearranges while maintaining good order. In stage III of the process, the GTSAXS peaks broaden, but there are still higher order peaks, indicating the system retains its long-range order. This process is templated assembly. The framework for the structure is set early during the drying process. Once the framework is set, even if the system has mobility, only short-range diffusion and local rearrangement is possible. Templated assembly is a result of the kinetic pathway taken rather than the thermodynamic driving force for

ordering. Once a template is set, the energetic cost to interdomain diffusion too high, trapping the system[35, 36]. Solvent leaves in the direction perpendicular to the film, allowing changes to the lattice in the z direction, but only small, local rearrangement is possible in plane to the thin film.

5.5 Comparison to Other Scattering Methods

GTSAXS is an effective method to monitor supramolecular nanocomposites *in situ*: clear transmission scattering peaks can be measured. However, there are several constraints as to what systems can be studied using GTSAXS due to the inherent constraints of the set-up. The parameters governing the set up and a schematic of the geometry are shown in Figure 9.

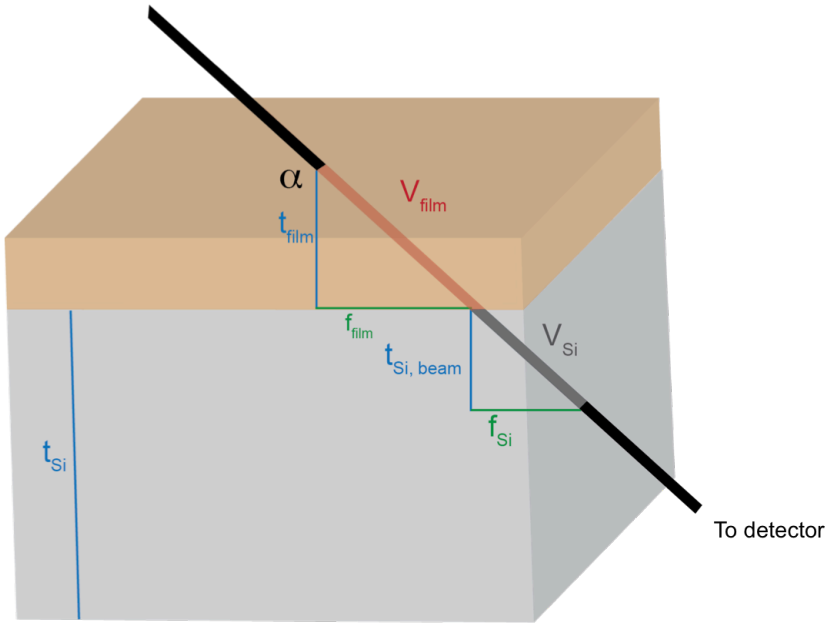

Figure 9: Schematic of GTSAXS set up. Schematic is not to scale so that relevant lengths and the beam pathway can be seen

The schematic is not drawn to scale so that the features are clear. Due to the small angle used (α=0.8˚), the beam passes through a considerable distance in the polymer film before reaching the silicon. It does not pass through the entire thickness of the silicon substrate, but rather exits through the side. Beam size is determined by the slit size, which in turn determines the volume of the sample or substrate the beam passes through. Here, the slit size was 50 μm x 100 μm. Table 1 shows the volume and distance the beam travels through the sample, and the horizontal footprint of the beam on the sample for the nanocomposite at its initial and final thickness. The beam passes through approximately one million cubic microns of the sample during the GTSAXS experiment. By contrast, if a SAXS experiment were to be carried out, the beam would only pass through approximately one thousand cubic microns. The volume of the sample is much higher in GTSAXS, which gives a larger signal than in SAXS experiments

Table 1: Length scale of beam pathway through the sample at its initial thickness, the sample at its final thickness, the silicon substrate, and a corresponding SAXS experiment.

	Thickness (t) (μm)	Beam pathway length through sample (μm)	Footprint (f) (μm)	Volume of sample (V) (μm^3)
Thin film (initial)	2.9	207.7	207.7	1.04×10^6
Thin film (final)	0.8	57.3	57.3	2.87×10^5
Thin film in SAXS (final)	0.8	0.8	-	4.0×10^3
Si	500	6000	6000	3.0×10^7

For any signal to be present in the final GTSAXS profile, the scattering from the sample must be strong since the signal passes through the substrate. The scattering length density (SLD) of all components in this nanocomposite is shown in Table 2[37]. The SLD of PS, P4VP, and PDP are all small, with minimal contrast between them. The SLD of the iron oxide NPs, however, is much higher, indicating that the scattering peaks come from the contrast between the NPs and the rest of the sample.

Table 2: Scattering length density (SLD) of each component in the nanocomposite

	PS	P4VP	PDP	Fe_2O_3
SLD(x10^{-6} Å)	1.39	1.70	0.19	7.18

Even if the contrast in SLD is strong, the signal will still be attenuated by the substrate. The expected intensity of a sample due to loss from attenuation can be determined following the exponential attenuation law $\frac{I}{I_o} = e^{-\left(\frac{\mu}{\rho}\right)*x}$, where I_o is the incident intensity, μ/ρ is the mass attenuation coefficient, and x is the mass thickness, defined as the density, ρ, times the sample thickness, t[38]. Table 3 shows the values used to calculate the attenuation of the signal by silicon as well as by polystyrene, which corresponds to the attenuation by the substrate and the sample, respectively. The mass attenuation coefficient was found from literature, and changes depending on the incident X-ray beam energy. For this experiment, the X-ray beam was at 12 keV. The listed values for mass attenuation coefficients are for 10 keV and 15 keV, so the intensity attenuation was calculated for both values, with

the assumption that the true attenuation value should lay between the two calculated values.

Table 3: Values used to calculate signal intensity attenuation

	Mass attenuation coefficient (cm^2/g)		Thickness (cm)	ρ (g/cm^3)	Mass thickness (g/cm^2)	I/I_o	
	at 10 keV	at 15 keV				at 10 keV	at 15 keV
PS	2.21	0.7738	$2.9x10^{-4}$	1.06	0.0219	0.95	0.98
Silicon	33.8	10.34	0.6	2.33	1.398	$3x10^{-21}$	$5x10^{-7}$

The sample, approximated as polystyrene, barely attenuates the signal, with I/I_o=0.95-0.98. The silicon substrate, however, attenuates the sample quite a bit, with I/I_o=$5x10^{-7}$ $3x10^{-21}$. The signal must be extremely strong for GTSAXS to be an effective method. The NPs are key to seeing any sort of signal in the GTSAXS profiles, limiting the use of this technique for polymer-only samples. However, using a neutron source rather than an X-ray source, for grazing-incidence small angle neutron scattering could open the door for investigating samples without large scattering contrast, since the substrate would not attenuate the sample. Even with the constraints of GTSAXS, it can be used to investigate nanocomposites both *in situ* and *ex situ* to determine the pathway of assembly and final film features of thin films using transmission geometry.

5.6 Conclusion

Here, GTSAXS has been used to monitor supramolecular nanocomposite thin films during *in situ* drying. It has shown to be effective for investigating the drying process due to the strong scattering from the NPs in the sample, despite large attenuation from the underlying substrate. These experiments have shown a three-step drying process where a highly ordered structure is quickly formed throughout the entire film. GTSAXS, as a transmission technique, was able to verify that this structure is formed throughout the entire film. In the final stage of drying, short-range diffusion dominates the pathway so the film disorders locally, but maintains long-range order across the entire film. The system rearranges locally, following templated assembly, resulting only in small changes in periodicity and lattice ordering. This study offers insight into how solution-based assembly can be used to create highly ordered nanocomposites.

5.7 Methods

Materials

The BCP, polystyrene-block-poly(4-vinyl pyridine) (PS(47 000)-*b*-P4VP(10 000)) (PDI = 1.10) was purchased from Polymer Source, Inc. 3-*n*-Pentadecylphenol (PDP) (95%) was purchased from Across. Chloroform was purchased from Fisher. Iron oxide NPs with core size of 5 nm were purchased from Ocean Nanotech. All chemicals were used as received.

Solution Preparation

The supramolecule was prepared by dissolving PS-P4VP with an appropriate amount of PDP in chloroform and stirred for a week. 3v% of 5 nm core iron oxide

nanoparticles were added to the supramolecular solution and mixed via vigorous shaking. The solution was then diluted with chloroform to a concentration of 0.8 wt%. The final film thickness of samples after drying was 800 nm.

Grazing Transmission Small Angle X-Ray Scattering (GTSAXS)

GTSAXS/GISAXS experimental measurements were made at beamline 8-ID-E the APS in Argonne National Laboratory and at beamline 7.3.3 at the ALS in Lawrence Berkeley National. X-ray wavelengths of 1.687 and 1.240 Å were used at APS, and ALS, respectively. The scattering intensity distribution was captured by a Pilatus 1 M detector at ALS and APS. The intensities (I) are plotted with respect to q, where $q = (4\pi/\lambda)\sin(\theta/2)$, λ is the wavelength of the incident X-ray beam, and θ is the scattering angle. A 2 cm x 2 cm silicon substrate was placed in a chamber designed for *in situ* measurements and aligned with the beam. A 500μL chloroform reservoir was injected into the chamber to slow the drying process and then ~100μL of sample was drop cast onto the substrate. Films were initially monitored at an incident angle of $\alpha=0.5^\circ$ until the initial formation of structure, when measurements were taken at $\alpha=0.8^\circ$ and the beamstop was lowered. GISAXS images were taken at $\alpha=0.14^\circ$.

Transmission Electron Microscopy (TEM)

TEM imaging was performed on a FEI Tecnai 12 TEM at an accelerating voltage of 120 kV. Thin film samples for TEM studies were prepared as described previously, except that the Si wafer was replaced a 200-mesh carbon film-coated copper grid and the film thickness was 100 nm.

References

Chapter 1: Structured Polymer Nanocomposites

1. Kim, H.; Abdala, A. A.; Macosko, C. W., Graphene/Polymer Nanocomposites. *Macromolecules* **2010,** *43* (16), 6515-6530.
2. Moniruzzaman, M.; Winey, K. I., Polymer nanocomposites containing carbon nanotubes. *Macromolecules* **2006,** *39* (16), 5194-5205.
3. Balazs, A. C.; Emrick, T.; Russell, T. P., Nanoparticle polymer composites: Where two small worlds meet. *Science* **2006,** *314* (5802), 1107-1110.
4. Kumar, S. K.; Benicewicz, B. C.; Vaia, R. A.; Winey, K. I., 50th Anniversary Perspective: Are Polymer Nanocomposites Practical for Applications? *Macromolecules* **2017,** *50* (3), 714-731.
5. Winey, K. I.; Vaia, R. A., Polymer nanocomposites. *Mrs Bulletin* **2007,** *32* (4), 314-319.
6. Gangopadhyay, R.; De, A., Conducting polymer nanocomposites: A brief overview. *Chemistry of Materials* **2000,** *12* (3), 608-622.
7. Paul, D. R.; Robeson, L. M., Polymer nanotechnology: Nanocomposites. *Polymer* **2008,** *49* (15), 3187-3204.
8. Goldstein, A. N.; Echer, C. M.; Alivisatos, A. P., MELTING IN SEMICONDUCTOR NANOCRYSTALS. *Science* **1992,** *256* (5062), 1425-1427.
9. Alivisatos, A. P., Perspectives on the physical chemistry of semiconductor nanocrystals. *Journal of Physical Chemistry* **1996,** *100* (31), 13226-13239.
10. Tolbert, S. H.; Alivisatos, A. P., HIGH-PRESSURE STRUCTURAL TRANSFORMATIONS IN SEMICONDUCTOR NANOCRYSTALS. *Annual Review of Physical Chemistry* **1995,** *46*, 595-625.
11. Alivisatos, A. P., Semiconductor clusters, nanocrystals, and quantum dots. *Science* **1996,** *271* (5251), 933-937.
12. Glotzer, S. C.; Solomon, M. J., Anisotropy of building blocks and their assembly into complex structures. *Nature Materials* **2007,** *6* (8), 557-562.
13. Choi, C. L.; Alivisatos, A. P., From Artificial Atoms to Nanocrystal Molecules: Preparation and Properties of More Complex Nanostructures. In *Annual Review of Physical Chemistry, Vol 61*, Leone, S. R.; Cremer, P. S.; Groves, J. T.; Johnson, M. A.; Richmond, G., Eds. Annual Reviews: Palo Alto, 2010; Vol. 61, pp 369-389.
14. Grzelczak, M.; Perez-Juste, J.; Mulvaney, P.; Liz-Marzan, L. M., Shape control in gold nanoparticle synthesis. *Chemical Society Reviews* **2008,** *37* (9), 1783-1791.
15. Grzelczak, M.; Vermant, J.; Furst, E. M.; Liz-Marzan, L. M., Directed Self-Assembly of Nanoparticles. *Acs Nano* **2010,** *4* (7), 3591-3605.
16. Mackay, M. E.; Tuteja, A.; Duxbury, P. M.; Hawker, C. J.; Van Horn, B.; Guan, Z. B.; Chen, G. H.; Krishnan, R. S., General strategies for nanoparticle dispersion. *Science* **2006,** *311* (5768), 1740-1743.
17. Liu, J.; Gao, Y. G.; Cao, D. P.; Zhang, L. Q.; Guo, Z. H., Nanoparticle Dispersion and Aggregation in Polymer Nanocomposites: Insights from Molecular Dynamics Simulation. *Langmuir* **2011,** *27* (12), 7926-7933.
18. Rao, J. P.; Geckeler, K. E., Polymer nanoparticles: Preparation techniques and size-control parameters. *Progress in Polymer Science* **2011,** *36* (7), 887-913.

19. Kao, J.; Thorkelsson, K.; Bai, P.; Rancatore, B. J.; Xu, T., Toward functional nanocomposites: taking the best of nanoparticles, polymers, and small molecules. *Chemical Society Reviews* **2013,** *42* (7), 2654-2678.
20. van Zoelen, W.; ten Brinke, G., Thin films of complexed block copolymers. *Soft Matter* **2009,** *5* (8), 1568-1582.
21. Ikkala, O.; ten Brinke, G., Functional materials based on self-assembly of polymeric supramolecules. *Science* **2002,** *295* (5564), 2407-2409.
22. Faul, C. F. J.; Antonietti, M., Ionic self-assembly: Facile synthesis of supramolecular materials. *Advanced Materials* **2003,** *15* (9), 673-683.
23. Hammond, M. R.; Mezzenga, R., Supramolecular routes towards liquid crystalline side-chain polymers. *Soft Matter* **2008,** *4* (5), 952-961.
24. Ikkala, O.; Knaapila, M.; Ruokolainen, J.; Torkkeli, M.; Serimaa, R.; Jokela, K.; Horsburgh, L.; Monkman, A.; ten Brinke, G., Self-organized liquid phase and co-crystallization of rod-like polymers hydrogen-bonded to amphiphilic molecules. *Advanced Materials* **1999,** *11* (14), 1206-1210.
25. Osuji, C.; Chao, C. Y.; Bita, I.; Ober, C. K.; Thomas, E. L., Temperature-dependent photonic bandgap in a self-assembled hydrogen-bonded liquid-crystalline diblock copolymer. *Advanced Functional Materials* **2002,** *12* (11-12), 753-758.
26. Chao, C. Y.; Li, X. F.; Ober, C. K.; Osuji, C.; Thomas, E. L., Orientational switching of mesogens and microdomains in hydrogen-bonded side-chain liquid-crystalline block copolymers using AC electric fields. *Advanced Functional Materials* **2004,** *14* (4), 364-370.
27. Chao, C. Y.; Li, X. F.; Ober, C. K., Directing self-assembly in macromolecular systems: Hydrogen bonding in ordered polymers. *Pure and Applied Chemistry* **2004,** *76* (7-8), 1337-1343.
28. de Wit, J.; van Ekenstein, G. A.; Polushkin, E.; Kvashnina, K.; Bras, W.; Ikkala, O.; ten Brinke, G., Self-assembled poly(4-vinylpyridine) - Surfactant systems using alkyl and alkoxy phenylazophenols. *Macromolecules* **2008,** *41* (12), 4200-4204.
29. Soininen, A. J.; Tanionou, I.; ten Brummelhuis, N.; Schlaad, H.; Hadjichristidis, N.; Ikkala, O.; Raula, J.; Mezzenga, R.; Ruokolainen, J., Hierarchical Structures in Lamellar Hydrogen Bonded LC Side Chain Diblock Copolymers. *Macromolecules* **2012,** *45* (17), 7091-7097.
30. Gopinadhan, M.; Majewski, P. W.; Beach, E. S.; Osuji, C. O., Magnetic Field Alignment of a Diblock Copolymer Using a Supramolecular Route. *Acs Macro Letters* **2012,** *1* (1), 184-189.
31. Rancatore, B. J.; Mauldin, C. E.; Tung, S. H.; Wang, C.; Hexemer, A.; Strzalka, J.; Frechet, J. M. J.; Xu, T., Nanostructured Organic Semiconductors via Directed Supramolecular Assembly. *Acs Nano* **2010,** *4* (5), 2721-2729.
32. Sary, N.; Richard, F.; Brochon, C.; Leclerc, N.; Leveque, P.; Audinot, J. N.; Berson, S.; Heiser, T.; Hadziioannou, G.; Mezzenga, R., A New Supramolecular Route for Using Rod-Coil Block Copolymers in Photovoltaic Applications. *Advanced Materials* **2010,** *22* (6), 763-+.

33. Lee, K. H.; Bai, P.; Rancatore, B. J.; He, B.; Liu, Y.; Xu, T., Improved Hierarchical Ordering in Supramolecules via Symmetrically Bifunctionalized Organic Semiconductor. *Macromolecules* **2016,** *49* (7), 2639-2645.
34. Valkama, S.; Kosonen, H.; Ruokolainen, J.; Haatainen, T.; Torkkeli, M.; Serimaa, R.; Ten Brinke, G.; Ikkala, O., Self-assembled polymeric solid films with temperature-induced large and reversible photonic-bandgap switching. *Nature Materials* **2004,** *3* (12), 872-876.
35. Ruokolainen, J.; Makinen, R.; Torkkeli, M.; Makela, T.; Serimaa, R.; ten Brinke, G.; Ikkala, O., Switching supramolecular polymeric materials with multiple length scales. *Science* **1998,** *280* (5363), 557-560.
36. Rancatore, B. J.; Mauldin, C. E.; Frechet, J. M. J.; Xu, T., Small Molecule-Guided Thermoresponsive Supramolecular Assemblies. *Macromolecules* **2012,** *45* (20), 8292-8299.
37. Zhao, Y.; Thorkelsson, K.; Mastroianni, A. J.; Schilling, T.; Luther, J. M.; Rancatore, B. J.; Matsunaga, K.; Jinnai, H.; Wu, Y.; Poulsen, D.; Frechet, J. M. J.; Alivisatos, A. P.; Xu, T., Small-molecule-directed nanoparticle assembly towards stimuli-responsive nanocomposites. *Nature Materials* **2009,** *8* (12), 979-985.
38. Kosonen, H.; Valkama, S.; Ruokolainen, J.; Torkkeli, M.; Serimaa, R.; ten Brinke, G.; Ikkala, O., One-dimensional optical reflectors based on self-organization of polymeric comb-shaped supramolecules. *European Physical Journal E* **2003,** *10* (1), 69-75.
39. Ruokolainen, J.; Saariaho, M.; Ikkala, O.; ten Brinke, G.; Thomas, E. L.; Torkkeli, M.; Serimaa, R., Supramolecular routes to hierarchical structures: Comb-coil diblock copolymers organized with two length scales. *Macromolecules* **1999,** *32* (4), 1152-1158.
40. Bates, F. S., Polymer-Polymer Phase Behavior. *Science* **1991,** *251* (4996), 898-905.
41. Albert, J. N. L.; Epps, T. H., Self-assembly of block copolymer thin films. *Materials Today* **2010,** *13* (6), 24-33.
42. Vukovic, I.; ten Brinke, G.; Loos, K., Hexagonally Perforated Layer Morphology in PS-b-P4VP(PDP) Supramolecules. *Macromolecules* **2012,** *45* (23), 9409-9418.
43. Tung, S. H.; Xu, T., Templated Assembly of Block Copolymer toward Nonequilibrium Nanostructures in Thin Films. *Macromolecules* **2009,** *42* (15), 5761-5765.
44. Valkama, S.; Ruotsalainen, T.; Nykanen, A.; Laiho, A.; Kosonen, H.; ten Brinke, G.; Ikkala, O.; Ruokolainen, J., Self-assembled structures in diblock copolymers with hydrogen-bonded amphiphilic plasticizing compounds. *Macromolecules* **2006,** *39* (26), 9327-9336.
45. Kao, J.; Tingsanchali, J.; Xu, T., Effects of Interfacial Interactions and Film Thickness on Nonequilibrium Hierarchical Assemblies of Block Copolymer-Based Supramolecules in Thin Films. *Macromolecules* **2011,** *44* (11), 4392-4400.
46. Tung, S. H.; Kalarickal, N. C.; Mays, J. W.; Xu, T., Hierarchical assemblies of block-copolymer-based supramolecules in thin films. *Macromolecules* **2008,** *41* (17), 6453-6462.

47. Amundson, K.; Helfand, E.; Davis, D. D.; Quan, X.; Patel, S. S.; Smith, S. D., EFFECT OF AN ELECTRIC-FIELD ON BLOCK COPOLYMER MICROSTRUCTURE. *Macromolecules* **1991,** *24* (24), 6546-6548.
48. Singh, G.; Yager, K. G.; Berry, B.; Kim, H. C.; Karim, A., Dynamic Thermal Field-Induced Gradient Soft-Shear for Highly Oriented Block Copolymer Thin Films. *Acs Nano* **2012,** *6* (11), 10335-10342.
49. Majewski, P. W.; Yager, K. G., Millisecond Ordering of Block Copolymer Films via Photothermal Gradients. *Acs Nano* **2015,** *9* (4), 3896-3906.
50. Majewski, P. W.; Gopinadhan, M.; Osuji, C. O., Magnetic field alignment of block copolymers and polymer nanocomposites: Scalable microstructure control in functional soft materials. *Journal of Polymer Science Part B-Polymer Physics* **2012,** *50* (1), 2-8.
51. Qiang, Z.; Zhang, L. H.; Stein, G. E.; Cavicchi, K. A.; Vogt, B. D., Unidirectional Alignment of Block Copolymer Films Induced by Expansion of a Permeable Elastomer during Solvent Vapor Annealing. *Macromolecules* **2014,** *47* (3), 1109-1116.
52. Tang, C. B.; Wu, W.; Smilgies, D. M.; Matyjaszewski, K.; Kowalewski, T., Robust Control of Microdomain Orientation in Thin Films of Block Copolymers by Zone Casting. *Journal of the American Chemical Society* **2011,** *133* (30), 11802-11809.
53. Sinturel, C.; Vayer, M.; Morris, M.; Hillmyer, M. A., Solvent Vapor Annealing of Block Polymer Thin Films. *Macromolecules* **2013,** *46* (14), 5399-5415.
54. Li, Y.; Wang, X. C.; Sanchez, I. C.; Johnston, K. P.; Green, P. F., Ordering in asymmetric block copolymer films by a compressible fluid. *Journal of Physical Chemistry B* **2007,** *111* (1), 16-25.
55. Tillmann, S. D.; Hermida-Merino, D.; Winter, M.; Cekic-Laskovic, I.; Loos, K., Nanoporous polymer foams derived from high molecular PS-b-P4VP(PDP)(x) for template-directed synthesis approaches. *Rsc Advances* **2016,** *6* (58), 52998-53003.
56. van Zoelen, W.; Polushkin, E.; ten Brinke, G., Hierarchical Terrace Formation in PS-b-P4VP(PDP) Supramolecular Thin Films. *Macromolecules* **2008,** *41* (22), 8807-8814.
57. van Zoelen, W.; Asumaa, T.; Ruokolainen, J.; Ikkala, O.; ten Brinke, G., Phase behavior of solvent vapor annealed thin films of PS-b-P4VP(PDP) supramolecules. *Macromolecules* **2008,** *41* (9), 3199-3208.
58. Huang, W. H.; Chen, P. Y.; Tung, S. H., Effects of Annealing Solvents on the Morphology of Block Copolymer-Based Supramolecular Thin Films. *Macromolecules* **2012,** *45* (3), 1562-1569.
59. Nandan, B.; Vyas, M. K.; Bohme, M.; Stamm, M., Composition-Dependent Morphological Transitions and Pathways in Switching of Fine Structure in Thin Films of Block Copolymer Supramolecular Assemblies. *Macromolecules* **2010,** *43* (5), 2463-2473.
60. Tokarev, I.; Krenek, R.; Burkov, Y.; Schmeisser, D.; Sidorenko, A.; Minko, S.; Stamm, M., Microphase separation in thin films of poly(styrene-block-4-vinylpyridine) copolymer-2-(4 '-hydroxybenzeneazo)benzoic acid assembly. *Macromolecules* **2005,** *38* (2), 507-516.

61. Kao, J.; Thorkelsson, K.; Bai, P.; Zhang, Z.; Sun, C.; Xu, T., Rapid fabrication of hierarchically structured supramolecular nanocomposite thin films in one minute. *Nature Communications* **2014,** *5*, 8.
62. Huang, J. Y.; Xiao, Y. H.; Xu, T., Achieving 3-D Nanoparticle Assembly in Nanocomposite Thin Films via Kinetic Control. *Macromolecules* **2017,** *50* (5), 2183-2188.
63. Kim, E.; Park, S.; Han, Y. S.; Kim, T. H., Effect of solvent selectivity on supramolecular assemblies of block copolymer by solvent-vapor annealing. *Polymer* **2018,** *150*, 214-222.
64. Cheng, J. Y.; Ross, C. A.; Smith, H. I.; Thomas, E. L., Templated self-assembly of block copolymers: Top-down helps bottom-up. *Advanced Materials* **2006,** *18* (19), 2505-2521.
65. Kao, J.; Jeong, S. J.; Jiang, Z.; Lee, D. H.; Aissou, K.; Ross, C. A.; Russell, T. P.; Xu, T., Direct 3-D Nanoparticle Assemblies in Thin Films via Topographically Patterned Surfaces. *Advanced Materials* **2014,** *26* (18), 2777-2781.
66. Wu, G. P.; Liu, X. Y.; Chen, X. X.; Suh, H. S.; Li, X.; Ren, J. X.; Arges, C. G.; Li, F. X.; Jiang, Z.; Nealey, P. F., Directed Self-Assembly of Hierarchical Supramolecular Block Copolymer Thin Films on Chemical Patterns. *Advanced Materials Interfaces* **2016,** *3* (13), 6.
67. Walton, D. G.; Kellogg, G. J.; Mayes, A. M.; Lambooy, P.; Russell, T. P., A Free Energy Model for Confined Diblock Copolymers. *Macromolecules* **1994,** *27* (21), 6225-6228.
68. Turner, M. S., EQUILIBRIUM PROPERTIES OF A DIBLOCK COPOLYMER LAMELLAR PHASE CONFINED BETWEEN FLAT PLATES. *Physical Review Letters* **1992,** *69* (12), 1788-1791.
69. Lambooy, P.; Russell, T. P.; Kellogg, G. J.; Mayes, A. M.; Gallagher, P. D.; Satija, S. K., Observed Frustration in Confined Block-Copolymers. *Physical Review Letters* **1994,** *72* (18), 2899-2902.
70. Koneripalli, N.; Singh, N.; Levicky, R.; Bates, F. S.; Gallagher, P. D.; Satija, S. K., CONFINED BLOCK-COPOLYMER THIN-FILMS. *Macromolecules* **1995,** *28* (8), 2897-2904.
71. Cheng, J. Y.; Mayes, A. M.; Ross, C. A., Nanostructure engineering by templated self-assembly of block copolymers. *Nature Materials* **2004,** *3* (11), 823-828.
72. Rockford, L.; Liu, Y.; Mansky, P.; Russell, T. P.; Yoon, M.; Mochrie, S. G. J., Polymers on nanoperiodic, heterogeneous surfaces. *Physical Review Letters* **1999,** *82* (12), 2602-2605.
73. Yang, X. M.; Peters, R. D.; Nealey, P. F.; Solak, H. H.; Cerrina, F., Guided self-assembly of symmetric diblock copolymer films on chemically nanopatterned substrates. *Macromolecules* **2000,** *33* (26), 9575-9582.
74. Edwards, E. W.; Montague, M. F.; Solak, H. H.; Hawker, C. J.; Nealey, P. F., Precise control over molecular dimensions of block-copolymer domains using the interfacial energy of chemically nanopatterned substrates. *Advanced Materials* **2004,** *16* (15), 1315-+.

75. Kim, S. O.; Solak, H. H.; Stoykovich, M. P.; Ferrier, N. J.; de Pablo, J. J.; Nealey, P. F., Epitaxial self-assembly of block copolymers on lithographically defined nanopatterned substrates. *Nature* **2003,** *424* (6947), 411-414.
76. Choi, H. K.; Chang, J. B.; Hannon, A. F.; Yang, J. K. W.; Berggren, K. K.; Alexander-Katz, A.; Ross, C. A., Nanoscale spirals by directed self-assembly. *Nano Futures* **2017,** *1* (1), 9.
77. Jung, Y. S.; Jung, W.; Ross, C. A., Nanofabricated concentric ring structures by templated self-assembly of a diblock copolymer. *Nano Letters* **2008,** *8* (9), 2975-2981.
78. Stoykovich, M. P.; Muller, M.; Kim, S. O.; Solak, H. H.; Edwards, E. W.; de Pablo, J. J.; Nealey, P. F., Directed assembly of block copolymer blends into nonregular device-oriented structures. *Science* **2005,** *308* (5727), 1442-1446.
79. Huang, J. Y.; Chen, X. F.; Bai, P.; Hai, R. H.; Sun, C.; Xu, T., 45% Periodicity Reduction in Nanocomposite Thin Films via Rapid Solvent Removal. *Macromolecules* **2019,** *52* (4), 1803-1809.
80. Huang, J.; Qian, Y.; Evans, K.; Xu, T., Diffusion-Dependent Nanoparticle Assembly in Thin Films of Supramolecular Nanocomposites: Effects of Particle Size and Supramolecular Morphology. Macromolecules, 2019.
81. Helfand, E., Diffusion in Strongly Segregated Block Copolymers. *Macromolecules* **1992,** *25* (1), 492-493.
82. Barrat, J. L.; Fredrickson, G. H., Diffusion of a Symmetric Block Copolymer in a Periodic Potential. *Macromolecules* **1991,** *24* (24), 6378-6383.
83. Dalvi, M. C.; Lodge, T. P., Parallel and Perpendicular Chain Diffusion in a Lamellar Block Copolymer. *Macromolecules* **1993,** *26* (4), 859-861.
84. Hamersky, M. W.; Tirrell, M.; Lodge, T. P., Anisotropy of diffusion in a lamellar styrene-isoprene block copolymer. *Langmuir* **1998,** *14* (24), 6974-6979.
85. Rittig, F.; Fleischer, G.; Karger, J.; Papadakis, C. M.; Almdal, K.; Stepanek, P., Anisotropic self-diffusion in a hexagonally ordered asymmetric PEP-PDMS diblock copolymer studied by pulsed field gradient NMR. *Macromolecules* **1999,** *32* (18), 5872-5877.
86. Hamersky, M. W.; Hillmyer, M. A.; Tirrell, M.; Bates, F. S.; Lodge, T. P.; von Meerwall, E. D., Block copolymer self-diffusion in the gyroid and cylinder morphologies. *Macromolecules* **1998,** *31* (16), 5363-5370.
87. Cavicchi, K. A.; Lodge, T. P., Anisotropic self-diffusion in block copolymer cylinders. *Macromolecules* **2004,** *37* (16), 6004-6012.
88. Yokoyama, H.; Kramer, E. J.; Fredrickson, G. H., Simulation of diffusion of asymmetric diblock and triblock copolymers in a spherical domain structure. *Macromolecules* **2000,** *33* (6), 2249-2257.
89. Cavicchi, K. A.; Lodge, T. P., Self-diffusion and tracer diffusion in sphere-forming block copolymers. *Macromolecules* **2003,** *36* (19), 7158-7164.
90. Yokoyama, H.; Kramer, E. J., Self-diffusion of asymmetric diblock copolymers with a spherical domain structure. *Macromolecules* **1998,** *31* (22), 7871-7876.
91. Dalvi, M. C.; Eastman, C. E.; Lodge, T. P., DIFFUSION IN MICROSTRUCTURED BLOCK-COPOLYMERS - CHAIN LOCALIZATION AND ENTANGLEMENTS. *Physical Review Letters* **1993,** *71* (16), 2591-2594.

92. Lodge, T. P.; Dalvi, M. C., MECHANISMS OF CHAIN DIFFUSION IN LAMELLAR BLOCK-COPOLYMERS. *Physical Review Letters* **1995,** *75* (4), 657-660.
93. Lodge, T. P.; Hamersky, M. W.; Milhaupt, J. M.; Kannan, R. M.; Dalvi, M. C.; Eastman, C. E., Diffusion in microstructured block copolymer melts. *Macromolecular Symposia* **1997,** *121*, 219-233.
94. Koo, K.; Ahn, H.; Kim, S. W.; Ryu, D. Y.; Russell, T. P., Directed self-assembly of block copolymers in the extreme: guiding microdomains from the small to the large. *Soft Matter* **2013,** *9* (38), 9059-9071.
95. Tanaka, H.; Hasegawa, H.; Hashimoto, T., ORDERED STRUCTURE IN MIXTURES OF A BLOCK COPOLYMER AND HOMOPOLYMERS .1. SOLUBILIZATION OF LOW-MOLECULAR-WEIGHT HOMOPOLYMERS. *Macromolecules* **1991,** *24* (1), 240-251.
96. Hashimoto, T.; Tanaka, H.; Hasegawa, H., ORDERED STRUCTURE IN MIXTURES OF A BLOCK COPOLYMER AND HOMOPOLYMERS .2. EFFECTS OF MOLECULAR-WEIGHTS OF HOMOPOLYMERS. *Macromolecules* **1990,** *23* (20), 4378-4386.
97. Winey, K. I.; Thomas, E. L.; Fetters, L. J., SWELLING A LAMELLAR DIBLOCK COPOLYMER WITH HOMOPOLYMER - INFLUENCES OF HOMOPOLYMER CONCENTRATION AND MOLECULAR-WEIGHT. *Macromolecules* **1991,** *24* (23), 6182-6188.
98. Dai, K. H.; Kramer, E. J.; Shull, K. R., INTERFACIAL SEGREGATION IN 2-PHASE POLYMER BLENDS WITH DIBLOCK COPOLYMER ADDITIVES - THE EFFECT OF HOMOPOLYMER MOLECULAR-WEIGHT. *Macromolecules* **1992,** *25* (1), 220-225.
99. Urbas, A.; Sharp, R.; Fink, Y.; Thomas, E. L.; Xenidou, M.; Fetters, L. J., Tunable block copolymer/homopolymer photonic crystals. *Advanced Materials* **2000,** *12* (11), 812-814.
100. Urbas, A.; Fink, Y.; Thomas, E. L., One-dimensionally periodic dielectric reflectors from self-assembled block copolymer-homopolymer blends. *Macromolecules* **1999,** *32* (14), 4748-4750.
101. Doerk, G. S.; Yager, K. G., Rapid Ordering in "Wet Brush" Block Copolymer/Homopolymer Ternary Blends. *Acs Nano* **2017,** *11* (12), 12326-12336.
102. Yoon, J.; Lee, W.; Thomas, E. L., Highly oriented thin-film Microdomain patterns of ultrahigh molecular weight block copolymers via directional solidification of a solvent. *Advanced Materials* **2006,** *18* (20), 2691-+.
103. Park, S.; Kim, Y.; Ahn, H.; Kim, J. H.; Yoo, P. J.; Ryu, D. Y., Giant Gyroid and Templates from High-Molecular-Weight Block Copolymer Self-assembly. *Scientific Reports* **2016,** *6*, 9.
104. Kim, E.; Ahn, H.; Park, S.; Lee, H.; Lee, M.; Lee, S.; Kim, T.; Kwak, E. A.; Lee, J. H.; Lei, X.; Huh, J.; Bang, J.; Lee, B.; Ryu, D. Y., Directed Assembly of High Molecular Weight Block Copolymers: Highly Ordered Line Patterns of Perpendicularly Oriented Lamellae with Large Periods. *Acs Nano* **2013,** *7* (3), 1952-1960.
105. Gu, W. Y.; Huh, J.; Hong, S. W.; Sveinbjornsson, B. R.; Park, C.; Grubbs, R. H.; Russell, T. P., Self-Assembly of Symmetric Brush Diblock Copolymers. *Acs Nano* **2013,** *7* (3), 2551-2558.

106. Runge, M. B.; Bowden, N. B., Synthesis of high molecular weight comb block copolymers and their assembly into ordered morphologies in the solid state. *Journal of the American Chemical Society* **2007,** *129* (34), 10551-10560.
107. Bolton, J.; Bailey, T. S.; Rzayev, J., Large Pore Size Nanoporous Materials from the Self-Assembly of Asymmetric Bottlebrush Block Copolymers. *Nano Letters* **2011,** *11* (3), 998-1001.
108. Rzayev, J., Synthesis of Polystyrene-Polylactide Bottlebrush Block Copolymers and Their Melt Self-Assembly into Large Domain Nanostructures. *Macromolecules* **2009,** *42* (6), 2135-2141.
109. Aviv, Y.; Altay, E.; Fink, L.; Raviv, U.; Rzayev, J.; Shenhar, R., Quasi-Two-Dimensional Assembly of Bottlebrush Block Copolymers with Nanoparticles in Ultrathin Films: Combined Effect of Graft Asymmetry and Nanoparticle Size. *Macromolecules* **2019,** *52* (1), 196-207.
110. Fraaije, J., DYNAMIC DENSITY-FUNCTIONAL THEORY FOR MICROPHASE SEPARATION KINETICS OF BLOCK-COPOLYMER MELTS. *Journal of Chemical Physics* **1993,** *99* (11), 9202-9212.
111. Ruiz, R.; Bosworth, J. K.; Black, C. T., Effect of structural anisotropy on the coarsening kinetics of diblock copolymer striped patterns. *Physical Review B* **2008,** *77* (5), 5.
112. Dai, H. J.; Balsara, N. P.; Garetz, B. A.; Newstein, M. C., Grain growth and defect annihilation in block copolymers. *Physical Review Letters* **1996,** *77* (17), 3677-3680.
113. Hur, S. M.; Thapar, V.; Ramirez-Hernandez, A.; Nealey, P. F.; de Pablo, J. J., Defect Annihilation Pathways in Directed Assembly of Lamellar Block Copolymer Thin Films. *Acs Nano* **2018,** *12* (10), 9974-9981.
114. Hur, S. M.; Thapar, V.; Ramirez-Hernandez, A.; Khaira, G.; Segal-Peretz, T.; Rincon-Delgadillo, P. A.; Li, W. H.; Muller, M.; Nealey, P. F.; de Pablo, J. J., Molecular pathways for defect annihilation in directed self-assembly. *Proceedings of the National Academy of Sciences of the United States of America* **2015,** *112* (46), 14144-14149.
115. Tsarkova, L.; Horvat, A.; Krausch, G.; Zvelindovsky, A. V.; Sevink, G. J. A.; Magerle, R., Defect evolution in block copolymer thin films via temporal phase transitions. *Langmuir* **2006,** *22* (19), 8089-8095.
116. Tsarkova, L.; Knoll, A.; Magerle, R., Rapid transitions between defect configurations in a block copolymer melt. *Nano Letters* **2006,** *6* (7), 1574-1577.
117. Hahm, J.; Sibener, S. J., Time-resolved atomic force microscopy imaging studies of asymmetric PS-b-PMMA ultrathin films: Dislocation and disclination transformations, defect mobility, and evolution of nanoscale morphology. *Journal of Chemical Physics* **2001,** *114* (10), 4730-4740.
118. Tong, Q. Q.; Sibener, S. J., Visualization of Individual Defect Mobility and Annihilation within Cylinder-Forming Diblock Copolymer Thin Films on Nanopatterned Substrates. *Macromolecules* **2013,** *46* (21), 8538-8544.
119. Li, W. H.; Muller, M., Thermodynamics and Kinetics of Defect Motion and Annihilation in the Self-Assembly of Lamellar Diblock Copolymers. *Macromolecules* **2016,** *49* (16), 6126-6138.

120. Harrison, C.; Cheng, Z. D.; Sethuraman, S.; Huse, D. A.; Chaikin, P. M.; Vega, D. A.; Sebastian, J. M.; Register, R. A.; Adamson, D. H., Dynamics of pattern coarsening in a two-dimensional smectic system. *Physical Review E* **2002,** *66* (1).
121. Harrison, C.; Angelescu, D. E.; Trawick, M.; Cheng, Z. D.; Huse, D. A.; Chaikin, P. M.; Vega, D. A.; Sebastian, J. M.; Register, R. A.; Adamson, D. H., Pattern coarsening in a 2D hexagonal system. *Europhysics Letters* **2004,** *67* (5), 800-806.
122. Ren, Y. Z.; Muller, M., Kinetics of pattern formation in symmetric diblock copolymer melts. *Journal of Chemical Physics* **2018,** *148* (20), 16.
123. Seguini, G.; Zanenga, F.; Laus, M.; Perego, M., Ordering kinetics in two-dimensional hexagonal pattern of cylinder-forming PS-b-PMMA block copolymer thin films: Dependence on the segregation strength. *Physical Review Materials* **2018,** *2* (5), 6.
124. Vacatello, M., Monte Carlo simulations of polymer melts filled with solid nanoparticles. *Macromolecules* **2001,** *34* (6), 1946-1952.
125. Smith, G. D.; Bedrov, D.; Li, L. W.; Byutner, O., A molecular dynamics simulation study of the viscoelastic properties of polymer nanocomposites. *Journal of Chemical Physics* **2002,** *117* (20), 9478-9489.
126. Desai, T.; Keblinski, P.; Kumar, S. K., Molecular dynamics simulations of polymer transport in nanocomposites. *Journal of Chemical Physics* **2005,** *122* (13), 8.
127. Gam, S.; Meth, J. S.; Zane, S. G.; Chi, C. Z.; Wood, B. A.; Seitz, M. E.; Winey, K. I.; Clarke, N.; Composto, R. J., Macromolecular Diffusion in a Crowded Polymer Nanocomposite. *Macromolecules* **2011,** *44* (9), 3494-3501.
128. Tung, W. S.; Griffin, P. T.; Meth, J. S.; Clarke, N.; Composto, R. J.; Winey, K. I., Temperature-Dependent Suppression of Polymer Diffusion in Polymer Nanocomposites. *Acs Macro Letters* **2016,** *5* (6), 735-739.
129. Sorichetti, V.; Hugouvieux, V.; Kob, W., Structure and Dynamics of a Polymer-Nanoparticle Composite: Effect of Nanoparticle Size and Volume Fraction. *Macromolecules* **2018,** *51* (14), 5375-5391.
130. Gam, S.; Meth, J. S.; Zane, S. G.; Chi, C. Z.; Wood, B. A.; Winey, K. I.; Clarke, N.; Composto, R. J., Polymer diffusion in a polymer nanocomposite: effect of nanoparticle size and polydispersity. *Soft Matter* **2012,** *8* (24), 6512-6520.
131. Lin, C. C.; Gam, S.; Meth, J. S.; Clarke, N.; Winey, K. I.; Composto, R. J., Do Attractive Polymer-Nanoparticle Interactions Retard Polymer Diffusion in Nanocomposites? *Macromolecules* **2013,** *46* (11), 4502-4509.
132. Choi, J.; Hore, M. J. A.; Meth, J. S.; Clarke, N.; Winey, K. I.; Composto, R. J., Universal Scaling of Polymer Diffusion in Nanocomposites. *Acs Macro Letters* **2013,** *2* (6), 485-490.
133. Bailey, E. J.; Griffin, P. J.; Tyagi, M.; Winey, K. I., Segmental Diffusion in Attractive Polymer Nanocomposites: A Quasi-Elastic Neutron Scattering Study. *Macromolecules* **2019,** *52* (2), 669-678.
134. Mackay, M. E.; Dao, T. T.; Tuteja, A.; Ho, D. L.; Van Horn, B.; Kim, H. C.; Hawker, C. J., Nanoscale effects leading to non-Einstein-like decrease in viscosity. *Nature Materials* **2003,** *2* (11), 762-766.
135. Roberts, C.; Cosgrove, T.; Schmidt, R. G.; Gordon, G. V., Diffusion of poly(dimethyl siloxane) mixtures with silicate nanoparticle. *Macromolecules* **2001,** *34* (3), 538-543.

136. Tuteja, A.; Mackay, M. E.; Narayanan, S.; Asokan, S.; Wong, M. S., Breakdown of the continuum Stokes-Einstein relation for nanoparticle diffusion. *Nano Letters* **2007,** *7* (5), 1276-1281.
137. Grabowski, C. A.; Adhikary, B.; Mukhopadhyay, A., Dynamics of gold nanoparticles in a polymer melt. *Applied Physics Letters* **2009,** *94* (2), 3.
138. Grabowski, C. A.; Mukhopadhyay, A., Size Effect of Nanoparticle Diffusion in a Polymer Melt. *Macromolecules* **2014,** *47* (20), 7238-7242.
139. Di, Z. Y.; Posselt, D.; Smilgies, D. M.; Papadakis, C. M., Structural Rearrangements in a Lamellar Diblock Copolymer Thin Film during Treatment with Saturated Solvent Vapor. *Macromolecules* **2010,** *43* (1), 418-427.
140. Papadakis, C. M.; Di, Z. Y.; Posselt, D.; Smilgies, D. M., Structural Instabilities in Lamellar Diblock Copolymer Thin Films During Solvent Vapor Uptake. *Langmuir* **2008,** *24* (24), 13815-13818.
141. Gu, X. D.; Gunkel, I.; Hexemer, A.; Russell, T. P., Controlling Domain Spacing and Grain Size in Cylindrical Block Copolymer Thin Films by Means of Thermal and Solvent Vapor Annealing. *Macromolecules* **2016,** *49* (9), 3373-3381.
142. Paik, M. Y.; Bosworth, J. K.; Smilges, D. M.; Schwartz, E. L.; Andre, X.; Ober, C. K., Reversible Morphology Control in Block Copolymer Films via Solvent Vapor Processing: An in Situ GISAXS Study. *Macromolecules* **2010,** *43* (9), 4253-4260.
143. Chavis, M. A.; Smilgies, D. M.; Wiesner, U. B.; Ober, C. K., Widely Tunable Morphologies in Block Copolymer Thin Films Through Solvent Vapor Annealing Using Mixtures of Selective Solvents. *Advanced Functional Materials* **2015,** *25* (20), 3057-3065.
144. Gu, X. D.; Gunkel, I.; Hexemer, A.; Gu, W. Y.; Russell, T. P., An In Situ Grazing Incidence X-Ray Scatterings Study of Block Copolymer Thin Films During Solvent Vapor Annealing. *Advanced Materials* **2014,** *26* (2), 273-281.
145. Gunkel, I.; Gu, X.; Sun, Z.; Schaible, E.; Hexemer, A.; Russell, T. P., An In Situ GISAXS Study of Selective Solvent Vapor Annealing in Thin Block Copolymer Films: Symmetry Breaking of In-Plane Sphere Order upon Deswelling. *Journal of Polymer Science Part B-Polymer Physics* **2016,** *54* (2), 331-338.

Chapter 2: Self-Assembly of Supramolecular Thin Films: Role of Small Molecule and Solvent Vapor Annealing

1. Ruokolainen, J.; ten Brinke, G.; Ikkala, O., Supramolecular polymeric materials with hierarchical structure-within-structure morphologies. *Advanced Materials* **1999,** *11* (9), 777-780.
2. Ruokolainen, J.; Saariaho, M.; Ikkala, O.; ten Brinke, G.; Thomas, E. L.; Torkkeli, M.; Serimaa, R., Supramolecular routes to hierarchical structures: Comb-coil diblock copolymers organized with two length scales. *Macromolecules* **1999,** *32* (4), 1152-1158.
3. Ruokolainen, J.; Makinen, R.; Torkkeli, M.; Makela, T.; Serimaa, R.; ten Brinke, G.; Ikkala, O., Switching supramolecular polymeric materials with multiple length scales. *Science* **1998,** *280* (5363), 557-560.

4. van Zoelen, W.; ten Brinke, G., Thin films of complexed block copolymers. *Soft Matter* **2009,** *5* (8), 1568-1582.
5. Ikkala, O.; ten Brinke, G., Hierarchical self-assembly in polymeric complexes: Towards functional materials. *Chemical Communications* **2004,** (19), 2131-2137.
6. Tang, C. B.; Lennon, E. M.; Fredrickson, G. H.; Kramer, E. J.; Hawker, C. J., Evolution of block copolymer lithography to highly ordered square arrays. *Science* **2008,** *322* (5900), 429-432.
7. Pollino, J. M.; Weck, M., Non-covalent side-chain polymers: design principles, functionalization strategies, and perspectives. *Chemical Society Reviews* **2005,** *34* (3), 193-207.
8. ten Brinke, G.; Ruokolainen, J.; Ikkala, O., Supramolecular materials based on hydrogen-bonded polymers. In *Hydrogen Bonded Polymers*, Binder, W., Ed. Springer-Verlag Berlin: Berlin, 2007; Vol. 207, pp 113-177.
9. Kosonen, H.; Valkama, S.; Hartikainen, J.; Eerikainen, H.; Torkkeli, M.; Jokela, K.; Serimaa, R.; Sundholm, F.; ten Brinke, G.; Ikkala, O., Mesomorphic structure of poly(styrene)-block-poly(4-vinylpyridine) with oligo(ethylene oxide)sulfonic acid side chains as a model for molecularly reinforced polymer electrolyte. *Macromolecules* **2002,** *35* (27), 10149-10154.
10. van Ekenstein, G. A.; Polushkin, E.; Nijland, H.; Ikkala, O.; ten Brinke, G., Shear alignment at two length scales: Comb-shaped supramolecules self-organized as cylinders-within-lamellar hierarchy. *Macromolecules* **2003,** *36* (10), 3684-3688.
11. de Moel, K.; Maki-Ontto, R.; Stamm, M.; Ikkala, O.; ten Brinke, G., Oscillatory shear flow-induced alignment of lamellar melts of hydrogen-bonded comb copolymer supramolecules. *Macromolecules* **2001,** *34* (9), 2892-2900.
12. Korhonen, J. T.; Verho, T.; Rannou, P.; Ikkala, O., Self-Assembly and Hierarchies in Pyridine-Containing Homopolymers and Block Copolymers with Hydrogen-Bonded Cholesteric Side-Chains. *Macromolecules* **2010,** *43* (3), 1507-1514.
13. van Zoelen, W.; van Ekenstein, G. A.; Ikkala, O.; ten Brinke, G., Incorporation of PPE in lamellar self-assembled PS-b-P4VP(PDP) supramolecules and PS-b-P4VP diblock copolymers. *Macromolecules* **2006,** *39* (19), 6574-6579.
14. Valkama, S.; Ruotsalainen, T.; Nykanen, A.; Laiho, A.; Kosonen, H.; ten Brinke, G.; Ikkala, O.; Ruokolainen, J., Self-assembled structures in diblock copolymers with hydrogen-bonded amphiphilic plasticizing compounds. *Macromolecules* **2006,** *39* (26), 9327-9336.
15. Tung, S. H.; Kalarickal, N. C.; Mays, J. W.; Xu, T., Hierarchical assemblies of block-copolymer-based supramolecules in thin films. *Macromolecules* **2008,** *41* (17), 6453-6462.
16. Vukovic, I.; ten Brinke, G.; Loos, K., Hexagonally Perforated Layer Morphology in PS-b-P4VP(PDP) Supramolecules. *Macromolecules* **2012,** *45* (23), 9409-9418.
17. Tung, S. H.; Xu, T., Templated Assembly of Block Copolymer toward Nonequilibrium Nanostructures in Thin Films. *Macromolecules* **2009,** *42* (15), 5761-5765.

18. Kao, J.; Tingsanchali, J.; Xu, T., Effects of Interfacial Interactions and Film Thickness on Nonequilibrium Hierarchical Assemblies of Block Copolymer-Based Supramolecules in Thin Films. *Macromolecules* **2011,** *44* (11), 4392-4400.
19. Ikkala, O.; ten Brinke, G., Functional materials based on self-assembly of polymeric supramolecules. *Science* **2002,** *295* (5564), 2407-2409.
20. Faul, C. F. J.; Antonietti, M., Ionic self-assembly: Facile synthesis of supramolecular materials. *Advanced Materials* **2003,** *15* (9), 673-683.
21. Hammond, M. R.; Mezzenga, R., Supramolecular routes towards liquid crystalline side-chain polymers. *Soft Matter* **2008,** *4* (5), 952-961.
22. Ikkala, O.; Knaapila, M.; Ruokolainen, J.; Torkkeli, M.; Serimaa, R.; Jokela, K.; Horsburgh, L.; Monkman, A.; ten Brinke, G., Self-organized liquid phase and co-crystallization of rod-like polymers hydrogen-bonded to amphiphilic molecules. *Advanced Materials* **1999,** *11* (14), 1206-1210.
23. Osuji, C.; Chao, C. Y.; Bita, I.; Ober, C. K.; Thomas, E. L., Temperature-dependent photonic bandgap in a self-assembled hydrogen-bonded liquid-crystalline diblock copolymer. *Advanced Functional Materials* **2002,** *12* (11-12), 753-758.
24. Chao, C. Y.; Li, X. F.; Ober, C. K.; Osuji, C.; Thomas, E. L., Orientational switching of mesogens and microdomains in hydrogen-bonded side-chain liquid-crystalline block copolymers using AC electric fields. *Advanced Functional Materials* **2004,** *14* (4), 364-370.
25. Chao, C. Y.; Li, X. F.; Ober, C. K., Directing self-assembly in macromolecular systems: Hydrogen bonding in ordered polymers. *Pure and Applied Chemistry* **2004,** *76* (7-8), 1337-1343.
26. de Wit, J.; van Ekenstein, G. A.; Polushkin, E.; Kvashnina, K.; Bras, W.; Ikkala, O.; ten Brinke, G., Self-assembled poly(4-vinylpyridine) - Surfactant systems using alkyl and alkoxy phenylazophenols. *Macromolecules* **2008,** *41* (12), 4200-4204.
27. Soininen, A. J.; Tanionou, I.; ten Brummelhuis, N.; Schlaad, H.; Hadjichristidis, N.; Ikkala, O.; Raula, J.; Mezzenga, R.; Ruokolainen, J., Hierarchical Structures in Lamellar Hydrogen Bonded LC Side Chain Diblock Copolymers. *Macromolecules* **2012,** *45* (17), 7091-7097.
28. Gopinadhan, M.; Majewski, P. W.; Beach, E. S.; Osuji, C. O., Magnetic Field Alignment of a Diblock Copolymer Using a Supramolecular Route. *Acs Macro Letters* **2012,** *1* (1), 184-189.
29. Rancatore, B. J.; Mauldin, C. E.; Tung, S. H.; Wang, C.; Hexemer, A.; Strzalka, J.; Frechet, J. M. J.; Xu, T., Nanostructured Organic Semiconductors via Directed Supramolecular Assembly. *Acs Nano* **2010,** *4* (5), 2721-2729.
30. Sary, N.; Richard, F.; Brochon, C.; Leclerc, N.; Leveque, P.; Audinot, J. N.; Berson, S.; Heiser, T.; Hadziioannou, G.; Mezzenga, R., A New Supramolecular Route for Using Rod-Coil Block Copolymers in Photovoltaic Applications. *Advanced Materials* **2010,** *22* (6), 763-+.
31. Lee, K. H.; Bai, P.; Rancatore, B. J.; He, B.; Liu, Y.; Xu, T., Improved Hierarchical Ordering in Supramolecules via Symmetrically Bifunctionalized Organic Semiconductor. *Macromolecules* **2016,** *49* (7), 2639-2645.

32. Valkama, S.; Kosonen, H.; Ruokolainen, J.; Haatainen, T.; Torkkeli, M.; Serimaa, R.; Ten Brinke, G.; Ikkala, O., Self-assembled polymeric solid films with temperature-induced large and reversible photonic-bandgap switching. *Nature Materials* **2004,** *3* (12), 872-876.
33. Rancatore, B. J.; Mauldin, C. E.; Frechet, J. M. J.; Xu, T., Small Molecule-Guided Thermoresponsive Supramolecular Assemblies. *Macromolecules* **2012,** *45* (20), 8292-8299.
34. Zhao, Y.; Thorkelsson, K.; Mastroianni, A. J.; Schilling, T.; Luther, J. M.; Rancatore, B. J.; Matsunaga, K.; Jinnai, H.; Wu, Y.; Poulsen, D.; Frechet, J. M. J.; Alivisatos, A. P.; Xu, T., Small-molecule-directed nanoparticle assembly towards stimuli-responsive nanocomposites. *Nature Materials* **2009,** *8* (12), 979-985.
35. Kosonen, H.; Valkama, S.; Ruokolainen, J.; Torkkeli, M.; Serimaa, R.; ten Brinke, G.; Ikkala, O., One-dimensional optical reflectors based on self-organization of polymeric comb-shaped supramolecules. *European Physical Journal E* **2003,** *10* (1), 69-75.
36. van Zoelen, W.; Asumaa, T.; Ruokolainen, J.; Ikkala, O.; ten Brinke, G., Phase behavior of solvent vapor annealed thin films of PS-b-P4VP(PDP) supramolecules. *Macromolecules* **2008,** *41* (9), 3199-3208.
37. Nandan, B.; Vyas, M. K.; Bohme, M.; Stamm, M., Composition-Dependent Morphological Transitions and Pathways in Switching of Fine Structure in Thin Films of Block Copolymer Supramolecular Assemblies. *Macromolecules* **2010,** *43* (5), 2463-2473.
38. van Zoelen, W.; Polushkin, E.; ten Brinke, G., Hierarchical Terrace Formation in PS-b-P4VP(PDP) Supramolecular Thin Films. *Macromolecules* **2008,** *41* (22), 8807-8814.
39. Kao, J.; Jeong, S. J.; Jiang, Z.; Lee, D. H.; Aissou, K.; Ross, C. A.; Russell, T. P.; Xu, T., Direct 3-D Nanoparticle Assemblies in Thin Films via Topographically Patterned Surfaces. *Advanced Materials* **2014,** *26* (18), 2777-2781.
40. Wu, G. P.; Liu, X. Y.; Chen, X. X.; Suh, H. S.; Li, X.; Ren, J. X.; Arges, C. G.; Li, F. X.; Jiang, Z.; Nealey, P. F., Directed Self-Assembly of Hierarchical Supramolecular Block Copolymer Thin Films on Chemical Patterns. *Advanced Materials Interfaces* **2016,** *3* (13), 6.
41. Kao, J.; Thorkelsson, K.; Bai, P.; Zhang, Z.; Sun, C.; Xu, T., Rapid fabrication of hierarchically structured supramolecular nanocomposite thin films in one minute. *Nature Communications* **2014,** *5*, 8.
42. Huang, J. Y.; Xiao, Y. H.; Xu, T., Achieving 3-D Nanoparticle Assembly in Nanocomposite Thin Films via Kinetic Control. *Macromolecules* **2017,** *50* (5), 2183-2188.
43. Dalvi, M. C.; Lodge, T. P., PARALLEL AND PERPENDICULAR CHAIN DIFFUSION IN A LAMELLAR BLOCK COPOLYMER. *Macromolecules* **1993,** *26* (4), 859-861.
44. Cavicchi, K. A.; Lodge, T. P., Self-diffusion and tracer diffusion in sphere-forming block copolymers. *Macromolecules* **2003,** *36* (19), 7158-7164.
45. Helfand, E., DIFFUSION IN STRONGLY SEGREGATED BLOCK COPOLYMERS. *Macromolecules* **1992,** *25* (1), 492-493.

46. Kao, J.; Bai, P.; Chuang, V. P.; Jiang, Z.; Ercius, P.; Xu, T., Nanoparticle Assemblies in Thin Films of Supramolecular Nanocomposites. *Nano Letters* **2012,** *12* (5), 2610-2618.
47. Lambooy, P.; Russell, T. P.; Kellogg, G. J.; Mayes, A. M.; Gallagher, P. D.; Satija, S. K., OBSERVED FRUSTRATION IN CONFINED BLOCK-COPOLYMERS. *Physical Review Letters* **1994,** *72* (18), 2899-2902.
48. Walton, D. G.; Kellogg, G. J.; Mayes, A. M.; Lambooy, P.; Russell, T. P., A FREE-ENERGY MODEL FOR CONFINED DIBLOCK COPOLYMERS. *Macromolecules* **1994,** *27* (21), 6225-6228.
49. Cheng, J. Y.; Mayes, A. M.; Ross, C. A., Nanostructure engineering by templated self-assembly of block copolymers. *Nature Materials* **2004,** *3* (11), 823-828.
50. Sinturel, C.; Vayer, M.; Morris, M.; Hillmyer, M. A., Solvent Vapor Annealing of Block Polymer Thin Films. *Macromolecules* **2013,** *46* (14), 5399-5415.
51. Kim, S. H.; Misner, M. J.; Xu, T.; Kimura, M.; Russell, T. P., Highly oriented and ordered arrays from block copolymers via solvent evaporation. *Advanced Materials* **2004,** *16* (3), 226-+.
52. Rockford, L.; Mochrie, S. G. J.; Russell, T. P., Propagation of nanopatterned substrate templated ordering of block copolymers in thick films. *Macromolecules* **2001,** *34* (5), 1487-1492.
53. Bita, I.; Yang, J. K. W.; Jung, Y. S.; Ross, C. A.; Thomas, E. L.; Berggren, K. K., Graphoepitaxy of self-assembled block copolymers on two-dimensional periodic patterned templates. *Science* **2008,** *321* (5891), 939-943.
54. Shelton, C. K.; Jones, R. L.; Epps, T. H., Kinetics of Domain Alignment in Block Polymer Thin Films during Solvent Vapor Annealing with Soft Shear: An in Situ Small-Angle Neutron Scattering Investigation. *Macromolecules* **2017,** *50* (14), 5367-5376.
55. Murphy, J. N.; Harris, K. D.; Buriak, J. M., Automated Defect and Correlation Length Analysis of Block Copolymer Thin Film Nanopatterns. *Plos One* **2015,** *10* (7), 32.

Chapter 3: Directed Self-Assembly of Supramolecular Thin Films on Circular Patterned Substrates

1. Valkama, S.; Ruotsalainen, T.; Nykanen, A.; Laiho, A.; Kosonen, H.; ten Brinke, G.; Ikkala, O.; Ruokolainen, J., Self-assembled structures in diblock copolymers with hydrogen-bonded amphiphilic plasticizing compounds. *Macromolecules* **2006,** *39* (26), 9327-9336.
2. Ruokolainen, J.; Saariaho, M.; Ikkala, O.; ten Brinke, G.; Thomas, E. L.; Torkkeli, M.; Serimaa, R., Supramolecular routes to hierarchical structures: Comb-coil diblock copolymers organized with two length scales. *Macromolecules* **1999,** *32* (4), 1152-1158.
3. Ruokolainen, J.; ten Brinke, G.; Ikkala, O., Supramolecular polymeric materials with hierarchical structure-within-structure morphologies. *Advanced Materials* **1999,** *11* (9), 777-780.

4. Ruokolainen, J.; Makinen, R.; Torkkeli, M.; Makela, T.; Serimaa, R.; ten Brinke, G.; Ikkala, O., Switching supramolecular polymeric materials with multiple length scales. *Science* **1998,** *280* (5363), 557-560.
5. Nandan, B.; Vyas, M. K.; Bohme, M.; Stamm, M., Composition-Dependent Morphological Transitions and Pathways in Switching of Fine Structure in Thin Films of Block Copolymer Supramolecular Assemblies. *Macromolecules* **2010,** *43* (5), 2463-2473.
6. Tokarev, I.; Krenek, R.; Burkov, Y.; Schmeisser, D.; Sidorenko, A.; Minko, S.; Stamm, M., Microphase separation in thin films of poly(styrene-block-4-vinylpyridine) copolymer-2-(4 '-hydroxybenzeneazo)benzoic acid assembly. *Macromolecules* **2005,** *38* (2), 507-516.
7. Korhonen, J. T.; Verho, T.; Rannou, P.; Ikkala, O., Self-Assembly and Hierarchies in Pyridine-Containing Homopolymers and Block Copolymers with Hydrogen-Bonded Cholesteric Side-Chains. *Macromolecules* **2010,** *43* (3), 1507-1514.
8. ten Brinke, G.; Ruokolainen, J.; Ikkala, O., Supramolecular materials based on hydrogen-bonded polymers. In *Hydrogen Bonded Polymers*, Binder, W., Ed. Springer-Verlag Berlin: Berlin, 2007; Vol. 207, pp 113-177.
9. Huang, J. Y.; Chen, X. F.; Bai, P.; Hai, R. H.; Sun, C.; Xu, T., 45% Periodicity Reduction in Nanocomposite Thin Films via Rapid Solvent Removal. *Macromolecules* **2019,** *52* (4), 1803-1809.
10. Huang, J. Y.; Xiao, Y. H.; Xu, T., Achieving 3-D Nanoparticle Assembly in Nanocomposite Thin Films via Kinetic Control. *Macromolecules* **2017,** *50* (5), 2183-2188.
11. Kao, J.; Xu, T., Nanoparticle Assemblies in Supramolecular Nanocomposite Thin Films: Concentration Dependence. *Journal of the American Chemical Society* **2015,** *137* (19), 6356-6365.
12. Kao, J.; Bai, P.; Lucas, J. M.; Alivisatos, A. P.; Xu, T., Size-Dependent Assemblies of Nanoparticle Mixtures in Thin Films. *Journal of the American Chemical Society* **2013,** *135* (5), 1680-1683.
13. Thorkelsson, K.; Nelson, J. H.; Alivisatos, A. P.; Xu, T., End-to-End Alignment of Nanorods in Thin Films. *Nano Letters* **2013,** *13* (10), 4908-4913.
14. Kao, J.; Bai, P.; Chuang, V. P.; Jiang, Z.; Ercius, P.; Xu, T., Nanoparticle Assemblies in Thin Films of Supramolecular Nanocomposites. *Nano Letters* **2012,** *12* (5), 2610-2618.
15. Kao, J.; Tingsanchali, J.; Xu, T., Effects of Interfacial Interactions and Film Thickness on Nonequilibrium Hierarchical Assemblies of Block Copolymer-Based Supramolecules in Thin Films. *Macromolecules* **2011,** *44* (11), 4392-4400.
16. Bates, F. S.; Fredrickson, G. H., Block copolymers - Designer soft materials. *Physics Today* **1999,** *52* (2), 32-38.
17. Hawker, C. J.; Russell, T. P., Block copolymer lithography: Merging "bottom-up" with "top-down" processes. *Mrs Bulletin* **2005,** *30* (12), 952-966.
18. Rockford, L.; Liu, Y.; Mansky, P.; Russell, T. P.; Yoon, M.; Mochrie, S. G. J., Polymers on nanoperiodic, heterogeneous surfaces. *Physical Review Letters* **1999,** *82* (12), 2602-2605.

19. Kim, S. O.; Solak, H. H.; Stoykovich, M. P.; Ferrier, N. J.; de Pablo, J. J.; Nealey, P. F., Epitaxial self-assembly of block copolymers on lithographically defined nanopatterned substrates. *Nature* **2003,** *424* (6947), 411-414.
20. Fasolka, M. J.; Harris, D. J.; Mayes, A. M.; Yoon, M.; Mochrie, S. G. J., Observed substrate topography-mediated lateral patterning of diblock copolymer films. *Physical Review Letters* **1997,** *79* (16), 3018-3021.
21. Segalman, R. A.; Yokoyama, H.; Kramer, E. J., Graphoepitaxy of spherical domain block copolymer films. *Advanced Materials* **2001,** *13* (15), 1152-+.
22. Sundrani, D.; Darling, S. B.; Sibener, S. J., Guiding polymers to perfection: Macroscopic alignment of nanoscale domains. *Nano Letters* **2004,** *4* (2), 273-276.
23. Sundrani, D.; Darling, S. B.; Sibener, S. J., Hierarchical assembly and compliance of aligned nanoscale polymer cylinders in confinement. *Langmuir* **2004,** *20* (12), 5091-5099.
24. Ruiz, R.; Kang, H. M.; Detcheverry, F. A.; Dobisz, E.; Kercher, D. S.; Albrecht, T. R.; de Pablo, J. J.; Nealey, P. F., Density multiplication and improved lithography by directed block copolymer assembly. *Science* **2008,** *321* (5891), 936-939.
25. Park, S.; Lee, D. H.; Xu, J.; Kim, B.; Hong, S. W.; Jeong, U.; Xu, T.; Russell, T. P., Macroscopic 10-Terabit-per-Square- Inch Arrays from Block Copolymers with Lateral Order. *Science* **2009,** *323* (5917), 1030-1033.
26. Jung, Y. S.; Ross, C. A., Orientation-controlled self-assembled nanolithography using a polystyrene-polydimethylsiloxane block copolymer. *Nano Letters* **2007,** *7* (7), 2046-2050.
27. Hong, S. W.; Huh, J.; Gu, X. D.; Lee, D. H.; Jo, W. H.; Park, S.; Xu, T.; Russell, T. P., Unidirectionally aligned line patterns driven by entropic effects on faceted surfaces. *Proceedings of the National Academy of Sciences of the United States of America* **2012,** *109* (5), 1402-1406.
28. Cheng, J. Y.; Ross, C. A.; Smith, H. I.; Thomas, E. L., Templated self-assembly of block copolymers: Top-down helps bottom-up. *Advanced Materials* **2006,** *18* (19), 2505-2521.
29. Cheng, J. Y.; Rettner, C. T.; Sanders, D. P.; Kim, H. C.; Hinsberg, W. D., Dense self-assembly on sparse chemical patterns: Rectifying and multiplying lithographic patterns using block copolymers. *Advanced Materials* **2008,** *20* (16), 3155-3158.
30. Walton, D. G.; Kellogg, G. J.; Mayes, A. M.; Lambooy, P.; Russell, T. P., A Free Energy Model for Confined Diblock Copolymers. *Macromolecules* **1994,** *27* (21), 6225-6228.
31. Lambooy, P.; Russell, T. P.; Kellogg, G. J.; Mayes, A. M.; Gallagher, P. D.; Satija, S. K., Observed Frustration in Confined Block-Copolymers. *Physical Review Letters* **1994,** *72* (18), 2899-2902.
32. Cheng, J. Y.; Mayes, A. M.; Ross, C. A., Nanostructure engineering by templated self-assembly of block copolymers. *Nature Materials* **2004,** *3* (11), 823-828.
33. Rockford, L.; Mochrie, S. G. J.; Russell, T. P., Propagation of nanopatterned substrate templated ordering of block copolymers in thick films. *Macromolecules* **2001,** *34* (5), 1487-1492.

34. Edwards, E. W.; Stoykovich, M. P.; Solak, H. H.; Nealey, P. F., Long-range order and orientation of cylinder-forming block copolymers on chemically nanopatterned striped surfaces. *Macromolecules* **2006,** *39* (10), 3598-3607.
35. Cheng, J. Y.; Ross, C. A.; Thomas, E. L.; Smith, H. I.; Vancso, G. J., Templated self-assembly of block copolymers: Effect of substrate topography. *Advanced Materials* **2003,** *15* (19), 1599-+.
36. Edwards, E. W.; Montague, M. F.; Solak, H. H.; Hawker, C. J.; Nealey, P. F., Precise control over molecular dimensions of block-copolymer domains using the interfacial energy of chemically nanopatterned substrates. *Advanced Materials* **2004,** *16* (15), 1315-+.
37. Yang, J. K. W.; Jung, Y. S.; Chang, J. B.; Mickiewicz, R. A.; Alexander-Katz, A.; Ross, C. A.; Berggren, K. K., Complex self-assembled patterns using sparse commensurate templates with locally varying motifs. *Nature Nanotechnology* **2010,** *5* (4), 256-260.
38. Son, J. G.; Chang, J. B.; Berggren, K. K.; Ross, C. A., Assembly of Sub-10-nm Block Copolymer Patterns with Mixed Morphology and Period Using Electron Irradiation and Solvent Annealing. *Nano Letters* **2011,** *11* (11), 5079-5084.
39. Stoykovich, M. P.; Muller, M.; Kim, S. O.; Solak, H. H.; Edwards, E. W.; de Pablo, J. J.; Nealey, P. F., Directed assembly of block copolymer blends into nonregular device-oriented structures. *Science* **2005,** *308* (5727), 1442-1446.
40. Choi, H. K.; Chang, J. B.; Hannon, A. F.; Yang, J. K. W.; Berggren, K. K.; Alexander-Katz, A.; Ross, C. A., Nanoscale spirals by directed self-assembly. *Nano Futures* **2017,** *1* (1), 9.
41. Jung, Y. S.; Jung, W.; Ross, C. A., Nanofabricated concentric ring structures by templated self-assembly of a diblock copolymer. *Nano Letters* **2008,** *8* (9), 2975-2981.
42. Wilmes, G. M.; Durkee, D. A.; Balsara, N. P.; Liddle, J. A., Bending soft block copolymer nanostructures by lithographically directed assembly. *Macromolecules* **2006,** *39* (7), 2435-2437.
43. Kao, J.; Jeong, S. J.; Jiang, Z.; Lee, D. H.; Aissou, K.; Ross, C. A.; Russell, T. P.; Xu, T., Direct 3-D Nanoparticle Assemblies in Thin Films via Topographically Patterned Surfaces. *Advanced Materials* **2014,** *26* (18), 2777-2781.
44. Kao, J.; Thorkelsson, K.; Bai, P.; Zhang, Z.; Sun, C.; Xu, T., Rapid fabrication of hierarchically structured supramolecular nanocomposite thin films in one minute. *Nature Communications* **2014,** *5*, 8.
45. Evans, K.; Xu, T., Self-Assembly of Supramolecular Thin Films: Role of Small Molecule and Solvent Vapor Annealing. *Macromolecules* **2019,** *52* (2), 639-648.
46. Murphy, J. N.; Harris, K. D.; Buriak, J. M., Automated Defect and Correlation Length Analysis of Block Copolymer Thin Film Nanopatterns. *Plos One* **2015,** *10* (7), 32.

Chapter 4: High Molecular Weight-Based Polymer Nanocomposites with Feature Sizes Greater than 50 nm

1. Grzelczak, M.; Vermant, J.; Furst, E. M.; Liz-Marzan, L. M., Directed Self-Assembly of Nanoparticles. *Acs Nano* **2010,** *4* (7), 3591-3605.
2. Sarkar, B.; Alexandridis, P., Block copolymer–nanoparticle composites: Structure, functional properties, and processing. *Progress in Polymer Science* **2015,** *40*, 33-62.
3. Balazs, A. C.; Emrick, T.; Russell, T. P., Nanoparticle polymer composites: Where two small worlds meet. *Science* **2006,** *314* (5802), 1107-1110.
4. Choi, C. L.; Alivisatos, A. P., From Artificial Atoms to Nanocrystal Molecules: Preparation and Properties of More Complex Nanostructures. In *Annual Review of Physical Chemistry, Vol 61*, Leone, S. R.; Cremer, P. S.; Groves, J. T.; Johnson, M. A.; Richmond, G., Eds. Annual Reviews: Palo Alto, 2010; Vol. 61, pp 369-389.
5. Kao, J.; Thorkelsson, K.; Bai, P.; Rancatore, B. J.; Xu, T., Toward functional nanocomposites: taking the best of nanoparticles, polymers, and small molecules. *Chemical Society Reviews* **2013,** *42* (7), 2654-2678.
6. ten Brinke, G.; Ruokolainen, J.; Ikkala, O., Supramolecular materials based on hydrogen-bonded polymers. In *Hydrogen Bonded Polymers*, Binder, W., Ed. Springer-Verlag Berlin: Berlin, 2007; Vol. 207, pp 113-177.
7. Ikkala, O.; ten Brinke, G., Hierarchical self-assembly in polymeric complexes: Towards functional materials. *Chemical Communications* **2004,** (19), 2131-2137.
8. Ikkala, O.; ten Brinke, G., Functional materials based on self-assembly of polymeric supramolecules. *Science* **2002,** *295* (5564), 2407-2409.
9. Ruokolainen, J.; Saariaho, M.; Ikkala, O.; ten Brinke, G.; Thomas, E. L.; Torkkeli, M.; Serimaa, R., Supramolecular routes to hierarchical structures: Comb-coil diblock copolymers organized with two length scales. *Macromolecules* **1999,** *32* (4), 1152-1158.
10. Ruokolainen, J.; ten Brinke, G.; Ikkala, O., Supramolecular polymeric materials with hierarchical structure-within-structure morphologies. *Advanced Materials* **1999,** *11* (9), 777-780.
11. Ikkala, O.; Knaapila, M.; Ruokolainen, J.; Torkkeli, M.; Serimaa, R.; Jokela, K.; Horsburgh, L.; Monkman, A.; ten Brinke, G., Self-organized liquid phase and co-crystallization of rod-like polymers hydrogen-bonded to amphiphilic molecules. *Advanced Materials* **1999,** *11* (14), 1206-1210.
12. Ruokolainen, J.; Makinen, R.; Torkkeli, M.; Makela, T.; Serimaa, R.; ten Brinke, G.; Ikkala, O., Switching supramolecular polymeric materials with multiple length scales. *Science* **1998,** *280* (5363), 557-560.
13. Tokarev, I.; Krenek, R.; Burkov, Y.; Schmeisser, D.; Sidorenko, A.; Minko, S.; Stamm, M., Microphase separation in thin films of poly(styrene-block-4-vinylpyridine) copolymer-2-(4 '-hydroxybenzeneazo)benzoic acid assembly. *Macromolecules* **2005,** *38* (2), 507-516.
14. van Zoelen, W.; Asumaa, T.; Ruokolainen, J.; Ikkala, O.; ten Brinke, G., Phase behavior of solvent vapor annealed thin films of PS-b-P4VP(PDP) supramolecules. *Macromolecules* **2008,** *41* (9), 3199-3208.

15. Valkama, S.; Ruotsalainen, T.; Nykanen, A.; Laiho, A.; Kosonen, H.; ten Brinke, G.; Ikkala, O.; Ruokolainen, J., Self-assembled structures in diblock copolymers with hydrogen-bonded amphiphilic plasticizing compounds. *Macromolecules* **2006,** *39* (26), 9327-9336.
16. Nandan, B.; Vyas, M. K.; Bohme, M.; Stamm, M., Composition-Dependent Morphological Transitions and Pathways in Switching of Fine Structure in Thin Films of Block Copolymer Supramolecular Assemblies. *Macromolecules* **2010,** *43* (5), 2463-2473.
17. Kao, J.; Tingsanchali, J.; Xu, T., Effects of Interfacial Interactions and Film Thickness on Nonequilibrium Hierarchical Assemblies of Block Copolymer-Based Supramolecules in Thin Films. *Macromolecules* **2011,** *44* (11), 4392-4400.
18. Tung, S. H.; Xu, T., Templated Assembly of Block Copolymer toward Nonequilibrium Nanostructures in Thin Films. *Macromolecules* **2009,** *42* (15), 5761-5765.
19. Thorkelsson, K.; Bronstein, N.; Xu, T., Nanorod-Based Supramolecular Nanocomposites: Effects of Nanorod Length. *Macromolecules* **2016,** *49* (17), 6669-6677.
20. Kao, J.; Xu, T., Nanoparticle Assemblies in Supramolecular Nanocomposite Thin Films: Concentration Dependence. *Journal of the American Chemical Society* **2015,** *137* (19), 6356-6365.
21. Kao, J.; Bai, P.; Lucas, J. M.; Alivisatos, A. P.; Xu, T., Size-Dependent Assemblies of Nanoparticle Mixtures in Thin Films. *Journal of the American Chemical Society* **2013,** *135* (5), 1680-1683.
22. Thorkelsson, K.; Nelson, J. H.; Alivisatos, A. P.; Xu, T., End-to-End Alignment of Nanorods in Thin Films. *Nano Letters* **2013,** *13* (10), 4908-4913.
23. Kao, J.; Bai, P.; Chuang, V. P.; Jiang, Z.; Ercius, P.; Xu, T., Nanoparticle Assemblies in Thin Films of Supramolecular Nanocomposites. *Nano Letters* **2012,** *12* (5), 2610-2618.
24. Thorkelsson, K.; Mastroianni, A. J.; Ercius, P.; Xu, T., Direct Nanorod Assembly Using Block Copolymer-Based Supramolecules. *Nano Letters* **2012,** *12* (1), 498-504.
25. Koo, K.; Ahn, H.; Kim, S. W.; Ryu, D. Y.; Russell, T. P., Directed self-assembly of block copolymers in the extreme: guiding microdomains from the small to the large. *Soft Matter* **2013,** *9* (38), 9059-9071.
26. Bates, F. S.; Fredrickson, G. H., BLOCK COPOLYMER THERMODYNAMICS - THEORY AND EXPERIMENT. *Annual Review of Physical Chemistry* **1990,** *41*, 525-557.
27. Colby, R. H.; Fetters, L. J.; Graessley, W. W., The melt viscosity-molecular weight relationship for linear polymers. *Macromolecules* **1987,** *20* (9), 2226-2237.
28. Urbas, A.; Sharp, R.; Fink, Y.; Thomas, E. L.; Xenidou, M.; Fetters, L. J., Tunable block copolymer/homopolymer photonic crystals. *Advanced Materials* **2000,** *12* (11), 812-814.
29. Urbas, A.; Fink, Y.; Thomas, E. L., One-dimensionally periodic dielectric reflectors from self-assembled block copolymer-homopolymer blends. *Macromolecules* **1999,** *32* (14), 4748-4750.

30. Doerk, G. S.; Yager, K. G., Rapid Ordering in "Wet Brush" Block Copolymer/Homopolymer Ternary Blends. *Acs Nano* **2017,** *11* (12), 12326-12336.
31. Winey, K. I.; Thomas, E. L.; Fetters, L. J., SWELLING A LAMELLAR DIBLOCK COPOLYMER WITH HOMOPOLYMER - INFLUENCES OF HOMOPOLYMER CONCENTRATION AND MOLECULAR-WEIGHT. *Macromolecules* **1991,** *24* (23), 6182-6188.
32. Tanaka, H.; Hasegawa, H.; Hashimoto, T., ORDERED STRUCTURE IN MIXTURES OF A BLOCK COPOLYMER AND HOMOPOLYMERS .1. SOLUBILIZATION OF LOW-MOLECULAR-WEIGHT HOMOPOLYMERS. *Macromolecules* **1991,** *24* (1), 240-251.
33. Hashimoto, T.; Tanaka, H.; Hasegawa, H., ORDERED STRUCTURE IN MIXTURES OF A BLOCK COPOLYMER AND HOMOPOLYMERS .2. EFFECTS OF MOLECULAR-WEIGHTS OF HOMOPOLYMERS. *Macromolecules* **1990,** *23* (20), 4378-4386.
34. Kim, E.; Ahn, H.; Park, S.; Lee, H.; Lee, M.; Lee, S.; Kim, T.; Kwak, E. A.; Lee, J. H.; Lei, X.; Huh, J.; Bang, J.; Lee, B.; Ryu, D. Y., Directed Assembly of High Molecular Weight Block Copolymers: Highly Ordered Line Patterns of Perpendicularly Oriented Lamellae with Large Periods. *Acs Nano* **2013,** *7* (3), 1952-1960.
35. Gu, W. Y.; Huh, J.; Hong, S. W.; Sveinbjornsson, B. R.; Park, C.; Grubbs, R. H.; Russell, T. P., Self-Assembly of Symmetric Brush Diblock Copolymers. *Acs Nano* **2013,** *7* (3), 2551-2558.
36. Choi, J.; Hore, M. J. A.; Meth, J. S.; Clarke, N.; Winey, K. I.; Composto, R. J., Universal Scaling of Polymer Diffusion in Nanocomposites. *Acs Macro Letters* **2013,** *2* (6), 485-490.
37. Valkama, S.; Kosonen, H.; Ruokolainen, J.; Haatainen, T.; Torkkeli, M.; Serimaa, R.; Ten Brinke, G.; Ikkala, O., Self-assembled polymeric solid films with temperature-induced large and reversible photonic-bandgap switching. *Nature Materials* **2004,** *3* (12), 872-876.
38. Bockstaller, M. R.; Mickiewicz, R. A.; Thomas, E. L., Block copolymer nanocomposites: Perspectives for tailored functional materials. *Advanced Materials* **2005,** *17* (11), 1331-1349.
39. Bockstaller, M. R.; Lapetnikov, Y.; Margel, S.; Thomas, E. L., Size-selective organization of enthalpic compatibilized nanocrystals in ternary block copolymer/particle mixtures. *Journal of the American Chemical Society* **2003,** *125* (18), 5276-5277.
40. Huang, J. Y.; Xiao, Y. H.; Xu, T., Achieving 3-D Nanoparticle Assembly in Nanocomposite Thin Films via Kinetic Control. *Macromolecules* **2017,** *50* (5), 2183-2188.
41. Huang, J. Y.; Chen, X. F.; Bai, P.; Hai, R. H.; Sun, C.; Xu, T., 45% Periodicity Reduction in Nanocomposite Thin Films via Rapid Solvent Removal. *Macromolecules* **2019,** *52* (4), 1803-1809.
42. Huang, J.; Qian, Y.; Evans, K.; Xu, T., Diffusion-Dependent Nanoparticle Assembly in Thin Films of Supramolecular Nanocomposites: Effects of Particle Size and Supramolecular Morphology. Macromolecules, 2019.

43. Kao, J.; Thorkelsson, K.; Bai, P.; Zhang, Z.; Sun, C.; Xu, T., Rapid fabrication of hierarchically structured supramolecular nanocomposite thin films in one minute. *Nature Communications* **2014,** *5*, 8.
44. Evans, K.; Xu, T., Self-Assembly of Supramolecular Thin Films: Role of Small Molecule and Solvent Vapor Annealing. *Macromolecules* **2019,** *52* (2), 639-648.
45. Tuteja, A.; Mackay, M. E.; Narayanan, S.; Asokan, S.; Wong, M. S., Breakdown of the continuum Stokes-Einstein relation for nanoparticle diffusion. *Nano Letters* **2007,** *7* (5), 1276-1281.
46. Ganesan, V.; Pryamitsyn, V.; Surve, M.; Narayanan, B., Noncontinuum effects in nanoparticle dynamics in polymers. *Journal of Chemical Physics* **2006,** *124* (22).
47. Murphy, J. N.; Harris, K. D.; Buriak, J. M., Automated Defect and Correlation Length Analysis of Block Copolymer Thin Film Nanopatterns. *Plos One* **2015,** *10* (7), 32.

Chapter 5: Probing the Self-Assembly Process of a Supramolecular Nanocomposite Thin Film Using *In Situ* Grazing-Incidence Transmission Small Angle X-Ray Scattering

1. Yang, H. T.; Jiang, P., Large-Scale Colloidal Self-Assembly by Doctor Blade Coating. *Langmuir* **2010,** *26* (16), 13173-13182.
2. Diao, Y.; Zhou, Y.; Kurosawa, T.; Shaw, L.; Wang, C.; Park, S.; Guo, Y. K.; Reinspach, J. A.; Gu, K.; Gu, X. D.; Tee, B. C. K.; Pang, C. H.; Yan, H. P.; Zhao, D. H.; Toney, M. F.; Mannsfeld, S. C. B.; Bao, Z. A., Flow-enhanced solution printing of all-polymer solar cells. *Nature Communications* **2015,** *6*, 10.
3. Barrows, A. T.; Pearson, A. J.; Kwak, C. K.; Dunbar, A. D. F.; Buckley, A. R.; Lidzey, D. G., Efficient planar heterojunction mixed-halide perovskite solar cells deposited via spray-deposition. *Energy & Environmental Science* **2014,** *7* (9), 2944-2950.
4. Baeg, K. J.; Jung, S. W.; Khim, D.; Kim, J.; Kim, D. Y.; Koo, J. B.; Quinn, J. R.; Facchetti, A.; You, I. K.; Noh, Y. Y., Low-voltage, high speed inkjet-printed flexible complementary polymer electronic circuits. *Organic Electronics* **2013,** *14* (5), 1407-1418.
5. Park, M.; Im, J.; Shin, M.; Min, Y.; Park, J.; Cho, H.; Park, S.; Shim, M. B.; Jeon, S.; Chung, D. Y.; Bae, J.; Jeong, U.; Kim, K., Highly stretchable electric circuits from a composite material of silver nanoparticles and elastomeric fibres. *Nature Nanotechnology* **2012,** *7* (12), 803-809.
6. Krebs, F. C., Fabrication and processing of polymer solar cells: A review of printing and coating techniques. *Solar Energy Materials and Solar Cells* **2009,** *93* (4), 394-412.
7. Steele, A.; Bayer, I.; Loth, E., Inherently Superoleophobic Nanocomposite Coatings by Spray Atomization. *Nano Letters* **2009,** *9* (1), 501-505.
8. Pierre, A.; Sadeghi, M.; Payne, M. M.; Facchetti, A.; Anthony, J. E.; Arias, A. C., All-Printed Flexible Organic Transistors Enabled by Surface Tension-Guided Blade Coating. *Advanced Materials* **2014,** *26* (32), 5722-+.

9. Farahani, R. D.; Dube, M.; Therriault, D., Three-Dimensional Printing of Multifunctional Nanocomposites: Manufacturing Techniques and Applications. *Advanced Materials* **2016,** *28* (28), 5794-5821.
10. Zhang, P.; Santoro, G.; Yu, S.; Vayalil, S. K.; Bommel, S.; Roth, S. V., Manipulating the Assembly of Spray-Deposited Nanocolloids: In Situ Study and Monolayer Film Preparation. *Langmuir* **2016,** *32* (17), 4251-4258.
11. Huang, J. Y.; Chen, X. F.; Bai, P.; Hai, R. H.; Sun, C.; Xu, T., 45% Periodicity Reduction in Nanocomposite Thin Films via Rapid Solvent Removal. *Macromolecules* **2019,** *52* (4), 1803-1809.
12. Huang, J. Y.; Xiao, Y. H.; Xu, T., Achieving 3-D Nanoparticle Assembly in Nanocomposite Thin Films via Kinetic Control. *Macromolecules* **2017,** *50* (5), 2183-2188.
13. Thorkelsson, K.; Bronstein, N.; Xu, T., Nanorod-Based Supramolecular Nanocomposites: Effects of Nanorod Length. *Macromolecules* **2016,** *49* (17), 6669-6677.
14. Zhao, Y.; Thorkelsson, K.; Mastroianni, A. J.; Schilling, T.; Luther, J. M.; Rancatore, B. J.; Matsunaga, K.; Jinnai, H.; Wu, Y.; Poulsen, D.; Frechet, J. M. J.; Alivisatos, A. P.; Xu, T., Small-molecule-directed nanoparticle assembly towards stimuli-responsive nanocomposites. *Nature Materials* **2009,** *8* (12), 979-985.
15. Gu, X. D.; Gunkel, I.; Hexemer, A.; Russell, T. P., Controlling Domain Spacing and Grain Size in Cylindrical Block Copolymer Thin Films by Means of Thermal and Solvent Vapor Annealing. *Macromolecules* **2016,** *49* (9), 3373-3381.
16. Gunkel, I.; Gu, X.; Sun, Z.; Schaible, E.; Hexemer, A.; Russell, T. P., An In Situ GISAXS Study of Selective Solvent Vapor Annealing in Thin Block Copolymer Films: Symmetry Breaking of In-Plane Sphere Order upon Deswelling. *Journal of Polymer Science Part B-Polymer Physics* **2016,** *54* (2), 331-338.
17. Gu, X. D.; Gunkel, I.; Hexemer, A.; Gu, W. Y.; Russell, T. P., An In Situ Grazing Incidence X-Ray Scatterings Study of Block Copolymer Thin Films During Solvent Vapor Annealing. *Advanced Materials* **2014,** *26* (2), 273-281.
18. Paik, M. Y.; Bosworth, J. K.; Smilges, D. M.; Schwartz, E. L.; Andre, X.; Ober, C. K., Reversible Morphology Control in Block Copolymer Films via Solvent Vapor Processing: An in Situ GISAXS Study. *Macromolecules* **2010,** *43* (9), 4253-4260.
19. Chavis, M. A.; Smilgies, D. M.; Wiesner, U. B.; Ober, C. K., Widely Tunable Morphologies in Block Copolymer Thin Films Through Solvent Vapor Annealing Using Mixtures of Selective Solvents. *Advanced Functional Materials* **2015,** *25* (20), 3057-3065.
20. Shelton, C. K.; Epps, T. H., Block copolymer thin films: Characterizing nanostructure evolution with in situ X-ray and neutron scattering. *Polymer* **2016,** *105*, 545-561.
21. Albalak, R. J.; Capel, M. S.; Thomas, E. L., Solvent swelling of roll-cast triblock copolymer films. *Polymer* **1998,** *39* (8-9), 1647-1656.
22. Stegelmeier, C.; Exner, A.; Hauschild, S.; Filiz, V.; Perlich, J.; Roth, S. V.; Abetz, V.; Forster, S., Evaporation-Induced Block Copolymer Self-Assembly into Membranes Studied by in Situ Synchrotron SAXS. *Macromolecules* **2015,** *48* (5), 1524-1530.

23. Lu, X. H.; Yager, K. G.; Johnston, D.; Black, C. T.; Ocko, B. M., Grazing-incidence transmission X-ray scattering: surface scattering in the Born approximation. *Journal of Applied Crystallography* **2013,** *46*, 165-172.
24. Mahadevapuram, N.; Strzalka, J.; Stein, G. E., Grazing-Incidence Transmission Small Angle X-Ray Scattering from Thin Films of Block Copolymers. *Journal of Polymer Science Part B-Polymer Physics* **2013,** *51* (7), 602-610.
25. Tung, S. H.; Xu, T., Templated Assembly of Block Copolymer toward Nonequilibrium Nanostructures in Thin Films. *Macromolecules* **2009,** *42* (15), 5761-5765.
26. Thorkelsson, K.; Mastroianni, A. J.; Ercius, P.; Xu, T., Direct Nanorod Assembly Using Block Copolymer-Based Supramolecules. *Nano Letters* **2012,** *12* (1), 498-504.
27. Ruokolainen, J.; Saariaho, M.; Ikkala, O.; ten Brinke, G.; Thomas, E. L.; Torkkeli, M.; Serimaa, R., Supramolecular routes to hierarchical structures: Comb-coil diblock copolymers organized with two length scales. *Macromolecules* **1999,** *32* (4), 1152-1158.
28. Thorkelsson, K.; Nelson, J. H.; Alivisatos, A. P.; Xu, T., End-to-End Alignrnent of Nanorods in Thin Films. *Nano Letters* **2013,** *13* (10), 4908-4913.
29. Kao, J.; Xu, T., Nanoparticle Assemblies in Supramolecular Nanocomposite Thin Films: Concentration Dependence. *Journal of the American Chemical Society* **2015,** *137* (19), 6356-6365.
30. Kao, J.; Bai, P.; Chuang, V. P.; Jiang, Z.; Ercius, P.; Xu, T., Nanoparticle Assemblies in Thin Films of Supramolecular Nanocomposites. *Nano Letters* **2012,** *12* (5), 2610-2618.
31. Kao, J.; Bai, P.; Lucas, J. M.; Alivisatos, A. P.; Xu, T., Size-Dependent Assemblies of Nanoparticle Mixtures in Thin Films. *Journal of the American Chemical Society* **2013,** *135* (5), 1680-1683.
32. Kao, J.; Thorkelsson, K.; Bai, P.; Zhang, Z.; Sun, C.; Xu, T., Rapid fabrication of hierarchically structured supramolecular nanocomposite thin films in one minute. *Nature Communications* **2014,** *5*, 8.
33. Filmetrics, Taking the Mystery Out of Thin-Film Measurements. Filmetrics, Ed. San Diego, 2018.
34. Li, Y.; Wang, X. C.; Sanchez, I. C.; Johnston, K. P.; Green, P. F., Ordering in asymmetric block copolymer films by a compressible fluid. *Journal of Physical Chemistry B* **2007,** *111* (1), 16-25.
35. Cavicchi, K. A.; Lodge, T. P., Self-diffusion and tracer diffusion in sphere-forming block copolymers. *Macromolecules* **2003,** *36* (19), 7158-7164.
36. Dalvi, M. C.; Lodge, T. P., PARALLEL AND PERPENDICULAR CHAIN DIFFUSION IN A LAMELLAR BLOCK COPOLYMER. *Macromolecules* **1993,** *26* (4), 859-861.
37. NIST Neutron activation and scattering calculator. (accessed May 10 2019).
38. Hubbell, J. H. a. S. S. M., Tables of x-ray mass attenuation coefficients and mass energy-absorption coefficients 1 keV to 20 meV for elements z = 1 to 92 and 48 additional substances of dosimetric interest. **1995**.